

AD-A045 220

EFFECTS TECHNOLOGY INC SANTA BARBARA CALIF
IMPACT DAMAGE IN SINGLE CRYSTALS.(U)

F/G 20/2

JUL 77 W F ADLER, S V HOOKER

N00014-76-C-0744

UNCLASSIFIED

ETI-TR77-49

NL

1 OF 2
ADA
045220



AD A 045 220

12

J

TR77-49

IMPACT DAMAGE IN SINGLE CRYSTALS

Technical Report

July 1977

Submitted to the

Office of Naval Research
800 N. Quincy Street
Arlington, VA 22217



by

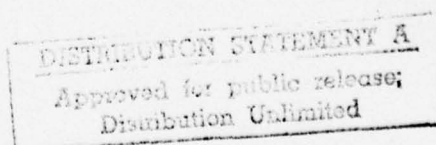
William F. Adler
Stephen V. Hooker

Reproduction in whole or in part is permitted for
any purpose of the United States Government

This research was sponsored by the Office of Naval Research
under Contract No. N00014-76-C-0744, NR 032-565.

EFFECTS TECHNOLOGY, INC.
5383 HOLLISTER AVENUE
SANTA BARBARA, CALIFORNIA 93111

AD No. _____
DDC FILE COPY



Unclassified

SECURITY CLASSIFICATION OF THIS PAGE (When Data Entered)

REPORT DOCUMENTATION PAGE		READ INSTRUCTIONS BEFORE COMPLETING FORM
1. REPORT NUMBER	2. GOVT ACCESSION NO.	3. RECIPIENT'S CATALOG NUMBER
4. TITLE (and Subtitle)		5. TYPE OF REPORT & PERIOD COVERED
(6) IMPACT DAMAGE IN SINGLE CRYSTALS.		Technical rept. 24 Mar 1976 - 31 July 1977
7. AUTHOR(s)		6. PERFORMING ORG. REPORT NUMBER
(10) William F. Adler and Stephen V. Hooker		(14) ETI-TR77-49
9. PERFORMING ORGANIZATION NAME AND ADDRESS		8. CONTRACT OR GRANT NUMBER(s)
Effects Technology, Inc. 5383 Hollister Avenue Santa Barbara, California 93111		(15) N00014-76-C-0744
11. CONTROLLING OFFICE NAME AND ADDRESS		10. PROGRAM ELEMENT, PROJECT, TASK AREA & WORK UNIT NUMBERS
Office of Naval Research		Project No. 471 (NR032-565)
14. MONITORING AGENCY NAME & ADDRESS (if different from Controlling Office)		12. REPORT DATE
(12) 119p		31 July 1977
		13. NUMBER OF PAGES
		116
		15. SECURITY CLASS. (of this report)
		Unclassified
		15a. DECLASSIFICATION DOWNGRADING SCHEDULE
16. DISTRIBUTION STATEMENT (of this Report)		
Approved for public release; distribution unlimited.		
17. DISTRIBUTION STATEMENT (of the abstract entered in Block 20, if different from Report)		
18. SUPPLEMENTARY NOTES		
19. KEY WORDS (Continue on reverse side if necessary and identify by block number)		
Impact	Calcium Fluoride	Hertzian Theory
Fracture	Silicon	Hugoniot Relations
Water Drop Impact	Germanium	Impact Damage Modes
Solid Particle Impact	Magnesium Oxide	
Erosion	Sapphire	
20. ABSTRACT (Continue on reverse side if necessary and identify by block number)		
<p>Single crystals of calcium fluoride, silicon, and magnesium oxide were subjected to quasistatic bead indentations from very low to moderately high load levels as reference for the dynamic loading conditions. 1 mm diameter beads were used in all of the tests reported here. Sapphire beads were propelled at velocities up to 100 ms^{-1} using a modified air gun arrangement which allows accurate placement of the particle on the surface, measurement of the impact velocity, and eliminates any rotational motions which would normally be imparted to the</p>		

DD FORM 1 JAN 73 1473

EDITION OF 1 NOV 55 IS OBSOLETE

Unclassified

SECURITY CLASSIFICATION OF THIS PAGE (When Data Entered)

100 m/s

405 842

1B

Unclassified

SECURITY CLASSIFICATION OF THIS PAGE(When Data Entered)

particle. Nylon beads were propelled at velocities up to 1000 ms^{-1} using an exploding wire impact facility. Single water drop impacts can now be obtained on these crystals at velocities up to 500 ms^{-1} , and multiple water drop experiments are carried out in a rotating arm erosion facility at velocities up to 260 ms^{-1} . 260 m/s 500 m/s

The general features of water drop and solid particle impacts are described in terms of relatively simple analytical models. These computations provide perspective on the approximate intensity of each test condition in relation to the nature of the observed failure modes. The least restrictive but still meaningful equivalence criteria are established for the two loading conditions. Impact conditions representative of the experimental investigations of particle collisions are used as specific examples: the particles are glass, sapphire and nylon beads and 1.8 and 2.0 mm water drops. In general it is found that it is not possible to satisfy all of the necessary equivalence criteria.

Preliminary observations of the damage produced by water drop impacts on CaF_2 , Si, and MgO are described for impact velocities below the coherent fracture threshold, but the effects of solid particle collisions on these crystals are considered in greater depth. Significantly different damage modes and sequences are observed for CaF_2 and MgO subjected to quasistatic sapphire bead indentations, sapphire bead impacts, and nylon bead impacts. The nature of the response to each of these loading conditions also differed between the two materials. Crystallographic fracture initiation was common to all of the particle loading conditions for Si. Some preliminary results on solid particle impacts on sapphire are also reported.

ACCESS	FOR
NTIS	<input type="checkbox"/>
DDC	<input type="checkbox"/>
UNANIM	
JUS I	
BY	DISTRICT/ANY
DI	COPIES
	CIAL
A	

Unclassified

SECURITY CLASSIFICATION OF THIS PAGE(When Data Entered)

TR77-49

IMPACT DAMAGE IN SINGLE CRYSTALS

Technical Report

for the period from 24 March 1976 through 31 July 1977

Contract No. N00014-76-C-0744

Project No. 471 (NR 032-565)

Prepared for the

Office of Naval Research
800 N. Quincy Street
Arlington, VA 22217

by

William F. Adler
Stephen V. Hooker

EFFECTS TECHNOLOGY, INC.
5383 HOLLISTER AVENUE
SANTA BARBARA, CALIFORNIA 93111
PHONE (805) 964-9831

THIS PAGE INTENTIONALLY BLANK

Abstract

Single crystals of calcium fluoride, silicon, and magnesium oxide were subjected to quasistatic bead indentations from very low to moderately high load levels as reference for the dynamic loading conditions. 1 mm diameter beads were used in all of the tests reported here. Sapphire beads were propelled at velocities up to 100 ms^{-1} using a modified air gun arrangement which allows accurate placement of the particle on the surface, measurement of the impact velocity, and eliminates any rotational motions which would normally be imparted to the particle. Nylon beads were propelled at velocities up to 1000 ms^{-1} using an exploding wire impact facility. Single water drop impacts can now be obtained on these crystals at velocities up to 500 ms^{-1} , and multiple water drop experiments are carried out in a rotating arm erosion facility at velocities up to 260 ms^{-1} .

The general features of water drop and solid particle impacts are described in terms of relatively simple analytical models. These computations provide perspective on the approximate intensity of each test condition in relation to the nature of the observed failure modes. The least restrictive but still meaningful equivalence criteria are established for the two loading conditions. Impact conditions representative of the experimental investigations of particle collisions are used as specific examples: the particles are glass, sapphire and nylon beads and 1.8 and 2.0 mm water drops. In general it is found that it is not possible to satisfy all of the necessary equivalence criteria.

Preliminary observations of the damage produced by water drop impacts on CaF_2 , Si, and MgO are described for impact velocities below the coherent fracture threshold, but the effects of solid particle collisions on these crystals are considered in greater depth. Significantly different damage modes and sequences are observed for CaF_2 .

and MgO subjected to quasistatic sapphire bead indentations, sapphire bead impacts, and nylon bead impacts. The nature of the response to each of these loading conditions also differed between the two materials. Crystallographic fracture initiation was common to all of the particle loading conditions for Si. Some preliminary results on solid particle impacts on sapphire are also reported.

TABLE OF CONTENTS

<u>SECTION</u>		<u>PAGE</u>
1.0	INTRODUCTION -----	1
2.0	EXPERIMENTAL PROCEDURE -----	5
2.1	LIQUID DROP IMPACT FACILITY -----	7
2.2	ANALYSIS OF PARTICLE IMPACT CONDITIONS -----	13
	2.2.1 Contact Area Between Impacting Bodies -----	14
	2.2.2 Magnitude and Form of the Inter- facial Pressure -----	19
	2.2.3 Stresses in a Half-Space Due to Particle Impacts -----	23
	2.2.4 Comparison of Solid Bead and Water Drop Impact Loading Conditions -----	44
3.0	EXPERIMENTAL RESULTS AND DISCUSSION -----	51
3.1	CALCIUM FLUORIDE -----	52
	3.1.1 Multiple Water Drop Impacts -----	52
	3.1.2 Nylon Bead Impacts -----	56
	3.1.3 Sapphire Bead Impacts -----	65
	3.1.4 Quasistatic Bead Indentations -----	69
3.2	SILICON -----	70
	3.2.1 Multiple Water Drop Impacts -----	72
	3.2.2 Nylon Bead Impacts -----	77
	3.2.3 Sapphire Bead Impacts -----	79
3.3	MAGNESIUM OXIDE -----	81
	3.3.1 Multiple Water Drop Impacts -----	81
	3.3.2 Nylon Bead Impacts -----	90
	3.3.3 Sapphire Bead Impacts -----	93
	3.3.4 Quasistatic Indentations -----	99
3.4	SAPPHIRE -----	104
4.0	SUMMARY -- -----	107
	ACKNOWLEDGEMENTS -----	111
	REFERENCES -----	113

THIS PAGE INTENTIONALLY BLANK

1.0 INTRODUCTION

The objectives of this program are to generate data which define the rain erosion behavior of selected infrared window materials and establish phenomenological and experimental analyses which describe the mechanisms and modes of degradation of material properties. The information obtained will be used to identify suitable hardening techniques for future window requirements.

The evolution of the rain erosion process from the initial impact up through the nucleation of erosion pits is the major concern of this investigation. Beyond this stage, the incubation period, the erosion process can be described in terms of the nucleation and growth of erosion pits. This is a general material removal process for water drops on the order of 1 mm in diameter impacting at subsonic to low supersonic velocities which has been described previously.⁽¹⁾ The sequence of events which takes place when a single spherical liquid drop strikes a plane surface has also been reviewed.⁽²⁾

The effects of the water drop collisions are quite localized on the specimen's surface. Although the intensity at subsonic and supersonic impact velocities is frequently insufficient to produce a definable pattern of damage, water drop impacts exploit weaknesses in the surface to produce an often irregular and ill-defined level of damage for a single impact. The most damaging condition is the propagation of cracks over macroscopic distances. Crack nucleation may result directly from a single or several water drop collisions onto sites of surface flaws. Alternatively, foreign particulate matter or minute second phases which are less erosion resistant than the bulk specimen material may be damaged and ejected by water drop impacts.

Once a crack is nucleated by liquid drop impingement it can be propagated during subsequent loading cycles. Continued crack growth depends upon both the location of subsequent drop collisions and the crack opening geometry. Three primary mechanisms can be enumerated which contribute to crack propagation. If the crack lies within the contact area of an impacting drop, the crack can be extended by the direct imposition of pressure with accompanying penetration of the liquid into the crack (hydraulic penetration mechanism). This is the most general means for crack extension which is effective in extending submicron size flaws up through cracks with lateral dimensions on the order of a millimeter or more. When cracks are formed, the edges of the crack are often displaced at the surface of the specimen. Typically, one edge of the crack is elevated several thousand angstroms above the surface of the specimen.⁽³⁾ This is a characteristic of the intermediate size cracks formed in most brittle and semi-brittle materials by liquid drop impacts. The second mechanism for crack growth occurs when a drop impacts the specimen's surface at a location where the lateral outflow jet (formed as the drop collapses onto the surface) impacts against the elevated edge of the crack thereby separating the two faces of the crack. The third mechanism for crack propagation is the interaction of stress waves propagating away from the impact site with pre-existing flaws and cracks. Stress wave propagation contributes to the nucleation of cracks from such defects and other sources of stress concentration as well as contributing to crack extension. The role of stress wave propagation is quite important in the earliest stages of the erosion process. However, its significance decreases rapidly as extensive crack networks or erosion pits develop when other mechanisms dominate the surface degradation process.

The phenomena associated with water drop collisions on crystalline materials are being investigated on a microscopic level to determine the controlling material properties. Consideration of the mechanics of liquid drop collisions has led to an investigation of solid particle

impacts. Impact conditions associated with solid particle impacts and their relation to water drop impacts have been investigated in conjunction with the failure modes observed for solid bead impacts on crystalline materials. This report is devoted primarily to a description of these failure modes for subsequent comparison with water drop impact damage and simple computations which define potential bases for comparison between the two forms of loading conditions.

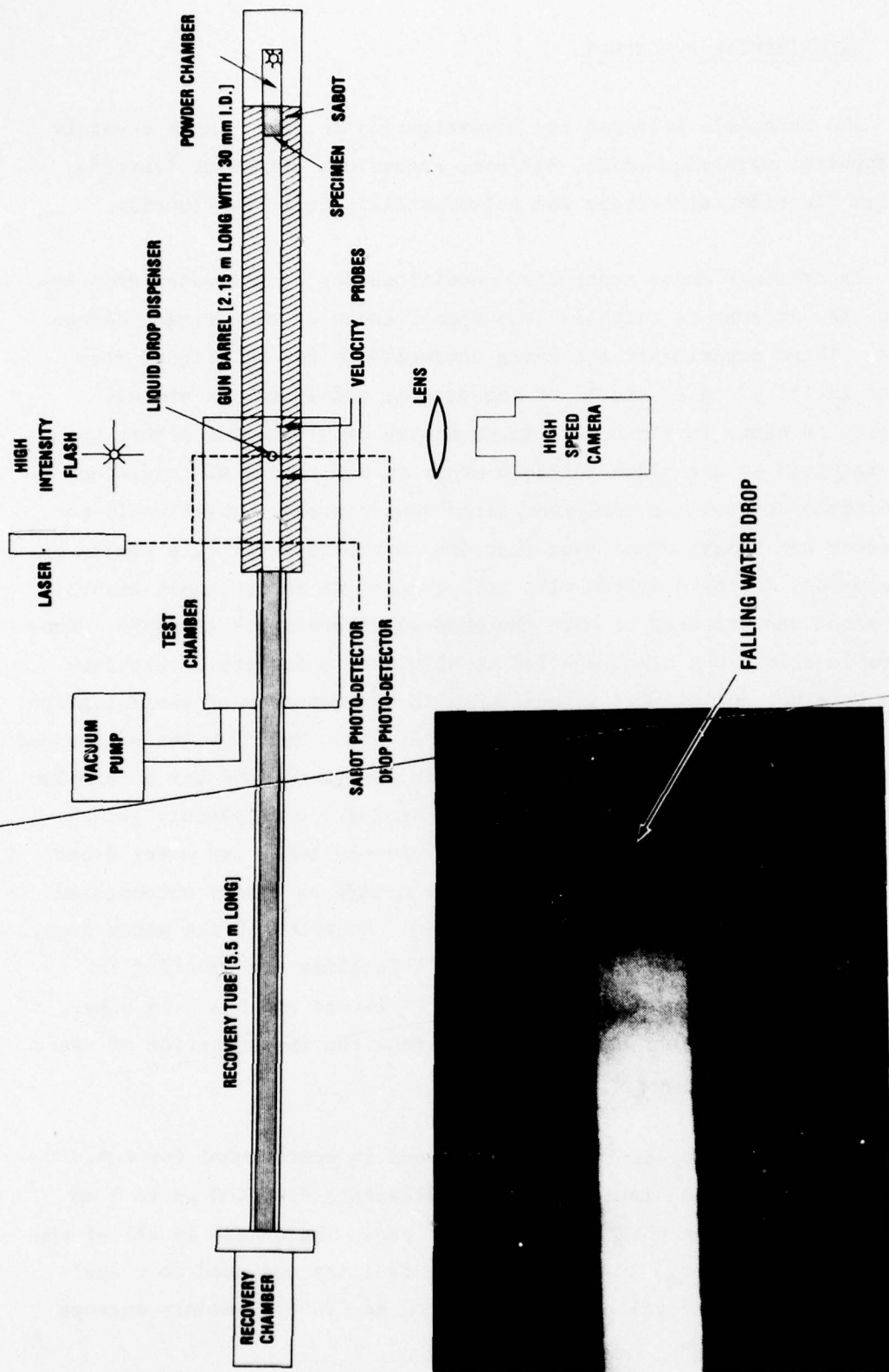
THIS PAGE INTENTIONALLY BLANK

2.0 EXPERIMENTAL PROCEDURE

The materials selected for investigation include single crystals of sapphire, magnesium oxide, silicon, germanium, strontium fluoride, lithium fluoride, and single and polycrystalline calcium fluoride.

Experiments under controlled conditions for single water drop impacts are underway to establish the significance of the primary damage modes. These experiments are being conducted in the ETI liquid drop impact facility. A schematic of the general configuration of this facility is shown in Figure 1. An extensive developmental effort has been required to establish suitable stopping and retrieval conditions for brittle crystalline specimens fired down the range which would not introduce any damage other than that due to the impact with a single water drop. A closed system with rail guides for the specimen mounted on a sabot was selected to meet the imposed recovery requirements. Considerable effort was also required to eliminate a variety of problems which were not anticipated associated with maintenance of the integrity of the water drop before impacting the specimen. The experience acquired in other ballistic range facilities was investigated, however no similar experimental arrangement was found which employed a completely guided sabot configuration, a relatively short recovery tube, and water drops in a closed system. In view of the above delays have been encountered in gathering data on water drop collisions. Examples of the water drop impacts obtained in the liquid drop impact facility are provided in Section 2.1. The results presented in this report are based on other forms of particle impact damage which augment the investigation of water drop impacts.

An air gun arrangement was designed and is operational for conducting dynamic solid bead impacts for bead diameters from 400 μm to 2 mm over a velocity range which is capable of producing damage in all of the materials of interest. An exploding wire facility was used to propel nylon beads at impact velocities up to 1000 ms^{-1} . Preliminary surveys



DETAIL OF FALLING DROP IN RAIL SYSTEM PRIOR TO IMPACT

Figure 1. Liquid Drop Impact Facility.

of the damage produced in the materials of interest when exposed to these various test conditions are described in Section 3. Section 2.2 is devoted to an analysis of the particle impact conditions relevant to this study and comparisons are made with the conditions representative of water drop impacts.

2.1 LIQUID DROP IMPACT FACILITY

A schematic of the ETI liquid drop impact facility is shown in Figure 1. The specimen is mounted at the front of a sabot which is propelled down the range by a small charge of gunpowder. Water drops are formed at the tip of a syringe mounted above the test section and fall in the path of the sabot which is completely confined along its trajectory. A slotted rail system is used to guide the specimen through the test section and into the recovery tube. As a single drop falls from the tip of the syringe it interrupts a laser beam focused onto a photo detector. This action initiates the firing sequence. The system is calibrated so the sabot reaches the drop when it has fallen to a point within the limits of the exposed surface of the specimen. After impacting the water drop the sabot and specimen pass through a second laser beam: one of three methods for obtaining velocity measurements. The impact velocity is also measured by means of velocity pins inserted in the path of the sabot a known distance apart and by measurements taken from the high-speed photographic record for the specimen impacting the water drop. The sabot then enters the recovery tube. A graded distribution of material in the recovery tube controls the deceleration of the sabot and protects the face of the specimen from extraneous damage.

The typical specimen is a disc: 22 mm in diameter and 6 mm thick. These dimensions are generally adequate to avoid edge effects, however non-circular specimens with lateral dimensions less than 22 mm and a wide range of thicknesses can be accommodated. The tests are conducted

in a vacuum of less than 1 mm of Hg to avoid distortions of the drop prior to impact. Currently the drop is a composition of 80% distilled water and 20% ethylene glycol. The water drop dimensions can be controlled to some extent by the size of the syringe over a range of 1.5 to 2.5 mm. The drop is photographed prior to impact so the diameter of the drop for a particular test is known. A photograph of the drop falling through the rail system in the test chamber is shown in the insert in Figure 1. High-speed photographs can be taken of the impact event in the same way. A Beckman and Whitley framing camera capable of recording at a maximum rate of four million frames per second is used for this purpose.

The gun is capable of accelerating the sabot to a maximum speed of 1800 ms^{-1} . At the present time the recovery system is designed to decelerate single crystals of germanium, silicon, calcium fluoride, and magnesium oxide at impact velocities up to 500 ms^{-1} without cracking the specimens or producing additional damage which obscures that due to the drop impact. This velocity range is sufficient to damage the materials of interest to a level in excess of that required in our investigations of water drop impacts on crystalline solids.

The nature of the water drop impact damage on polymethylmethacrylate (PMMA) and soda lime glass specimens is shown in Figures 2 to 5. Uniform drop diameters are obtained when the conditions in the water drop impact facility are held constant. The damage due to a 2 mm water drop is currently being investigated. For the velocity range required in the experimental program, 300 to 500 ms^{-1} , PMMA provides an excellent imprint of the water drop impact in order to check the symmetry of the drop collision and to check the uniformity of the damage over the impact site. Profilometer traces of the impressions on PMMA specimens, for example as shown in Figure 2, are comparable to those reported by Fyall.⁽⁴⁾ The PMMA specimens are also used to determine the extent of



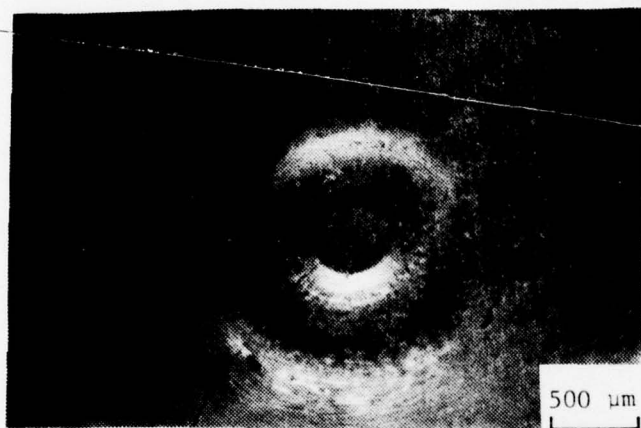
1 μm
100 μm

PROFILOMETER TRACE

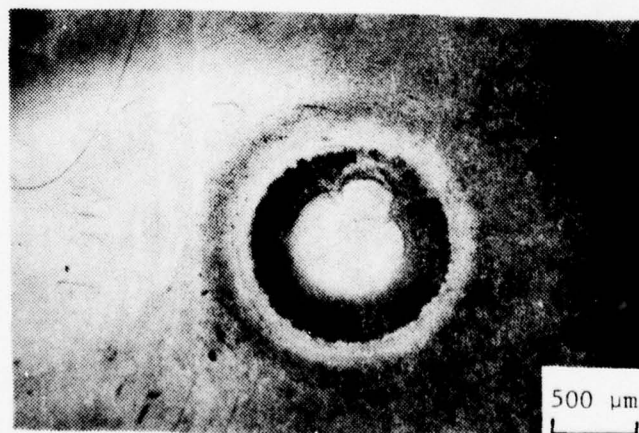
Figure 2. 2 mm Water Drop Impacting PMMA at 260 ms^{-1} .



a. 274 ms^{-1}

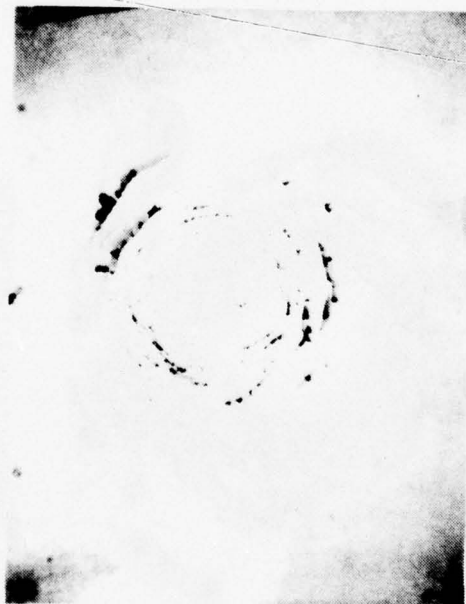


b. 310 ms^{-1}



c. 450 ms^{-1}

Figure 3. General Character of 1.8 mm Water Drop Impacts on Polymethylmethacrylate Over the Velocity Range to be Used in the Experiments on Single Crystals.

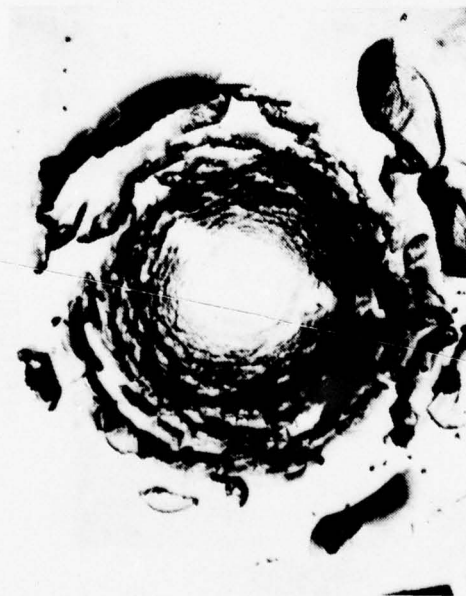


REFLECTED ILLUMINATION



TRANSMITTED ILLUMINATION

Figure 4. 2 mm Water Drop Impact on Soda Lime Glass at 300 ms^{-1} .



TRANSMITTED ILLUMINATION



REFLECTED ILLUMINATION

Figure 5. 2 mm Water Drop Impact on Soda Lime Glass at 450 ms^{-1} .

the damage, if any, which may be imparted to the specimen's surface during recovery. This characterization procedure is essential, since the symmetry and quality of the water drop collision is not at all evident on single crystals for impact velocities below and at the fracture threshold.

Soda lime glass was used in the developmental stages of the liquid drop impact facility to establish the appropriate recovery conditions for the brittle ceramic specimens to be used in the experimental program, although several of the crystalline materials were more susceptible to damage than soda lime glass. The mechanics of the recovery process have now been developed to the point that soda lime glass specimens can be fired down the range, impacted by a water drop, and recovered without extraneous damage at velocities in excess of 500 ms^{-1} . Typical water drop impacts are shown in Figures 4 and 5 for an impact velocity near the fracture threshold and for a higher velocity impact with extensive damage to the specimen. The upper limit for the impact velocity for the weaker crystals, such as germanium, is governed by the extent of the damage produced by the water drop impact and its interaction with the decelerating forces which can produce large cracks in the specimen. The stronger crystals do not present this problem until the extent of the damage is well beyond that which is of interest in the current program.

Water drop impacts on a number of crystalline specimens have now been obtained and are being analyzed. The analysis of the damage modes will be described in a future report.

2.2 ANALYSIS OF PARTICLE IMPACT CONDITIONS

Spherical water drop impacts under controlled conditions are generally quite difficult to obtain in the laboratory. As a consequence there is incentive to devise alternative means to simulate the general

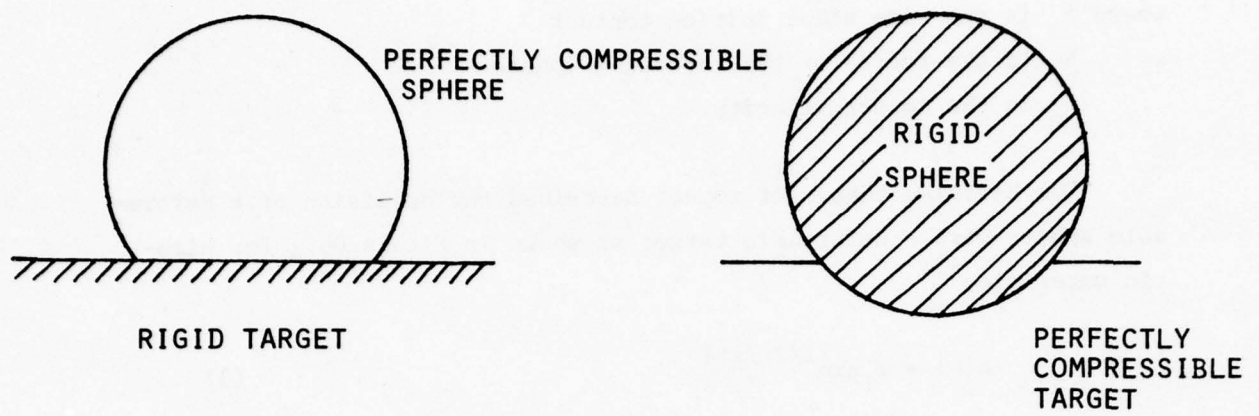
features of a water drop impact. It is an interesting and challenging undertaking to try to establish meaningful correlations between a water drop impact and other forms of localized loadings on a deformable plane surface. However in exploring these possibilities it cannot be over-emphasized that the approach followed in this work is that controlled experiments with liquid drops and microscopic examination of the resulting failure modes are the only accurate assessment of rain erosion damage; it is to this reference data that the results from alternative tests environments must be compared. Idealized analyses for the range of test conditions used in this work will be employed to gain some perspective on the relative intensity of the various test conditions. This information is useful in comparing the failure modes described in Section 3.

In considering particle impacts ranging from water drops to sapphire beads, a comparison of the loading conditions depends on three factors: the temporal development of the contact zone between the particle and the target's surface, the magnitude of the pressure which develops at the contact interface, and the spatial and temporal development of the pressure distribution.

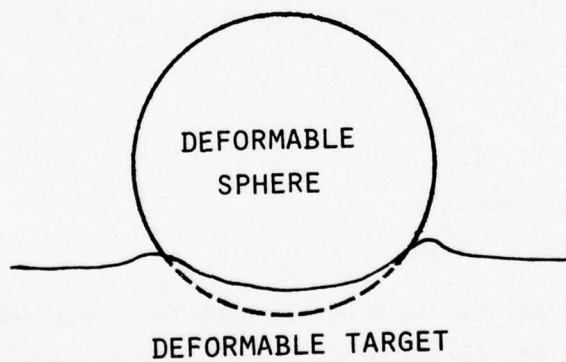
2.2.1 Contact Area Between Impacting Bodies

Particle/target interactions can be considered from several points of view. For example, the extremes of material response can be considered as shown in Figure 6a. For the idealized conditions shown the expansion of the circular contact zone (denoted by the radius a) can be described by the relation.

$$a(t) = \left[2RV_0 t - (V_0 t)^2 \right]^{1/2} \quad (1)$$



(a) Idealized Limiting Conditions



(b) General Form of Interfacial Deformations

Figure 6. Impact of a Sphere on a Half-Space.

where t is the time after initial contact

R is the radius of the impacting sphere

V_o is the impact velocity.

The Hertzian theory of impact describes the collision of a deformable sphere with a deformable target as shown in Figure 6b. For elastic materials, ⁽⁵⁾

$$a(t) = a_1 \sin^{1/2} \left(\frac{\pi t}{T} \right) \quad (2)$$

where $a_1 = K^{1/2} R V_o^{2/5}$ is the maximum contact radius

$T = 2.943 K^{2/5} R V_o^{-1/5}$ is the duration the bodies are in contact

$K = 1.25 \pi \rho_1 \left(\frac{1}{\rho_1 C_1^2} + \frac{1}{\rho_2 C_2^2} \right)$ represents the elastic properties of the impacting bodies.

ρ_1, ρ_2 are the densities of the sphere and the target, respectively,

C_1, C_2 are the elastic wave velocities for the sphere and the target, respectively,

$$C^2 = \frac{1}{\rho} \left(\frac{E}{1 - \nu^2} \right) \quad (3)$$

where E is Young's modulus

ν is Poisson's ratio.

The expression in Eq. (1) is a purely geometric relationship, while the expression in Eq. (2) involves the elastic properties of the impacting bodies.

Eq. (1) has been used to characterize liquid drop impacts when it is approximated by ^(2,6)

$$a(t) = \left(2 R V_o t \right)^{1/2} \quad (4)$$

The difference between Eq. (1) and (4) is only significant when $(a/R) > 0.5$.⁽²⁾ For a water drop impact the pressure loading phase prior to lateral outflow is generally completed before the contact radius reaches $0.5R$, so the approximation in Eq. (4) is quite acceptable. The expression in Eq. (4) has also been shown to be representative of the time-dependence of the contact zone based on comparisons with more accurate material response models.⁽²⁾

The corresponding condition to that represented by Eq. (1) and (4) for the Hertzian impact would be a deformable elastic sphere impacting a rigid half-space. For this impact condition

$$a(t) = \left(\frac{5}{4}\pi\right)^{1/5} R \left(\frac{V_0}{C_1}\right)^{2/5} \sin^{1/2} \left[\frac{\pi}{5.1} \left(\frac{C_1}{V_1}\right)^{4/5} \left(\frac{V_0 t}{R}\right) \right] \quad (5)$$

The relative velocity between the two colliding bodies is zero when

$$a(t) = a_1 = \left(\frac{5}{4}\pi\right)^{1/5} R \left(\frac{V_0}{C_1}\right)^{2/5} \quad (6)$$

at time $t = T/2$. Then the sphere rebounds from the surface after another time increment equal to $T/2$. The elastic properties and density of the material are represented in C_1 according to Eq. (3). It is seen that the maximum contact radius is determined by the magnitude of C_1 . For a rigid sphere $C_1 \rightarrow \infty$ and $a_1 \rightarrow 0$.

It is easy to show that according to Eq. (4) and (5) the times required for the elastic sphere to reach a contact radius a_1 will always be 5.1 times that required for the idealized model in Figure 6a to achieve the same contact radius. Representative values of the maximum contact radii, a_1 , and contact times, T , are listed in Table 1 for the materials used in the solid particle impact experiments. If the target material is deformable, a_1 and T are always larger than the values in Table 1.

Table 1. 1 mm Diameter Beads Impacting a Rigid Half-Space

BEAD MATERIAL	WAVE VELOCITY C_1 (mm/ μ s)	IMPACT VELOCITY V_o (mm/ μ s)	MAXIMUM CONTACT RADIUS a_1 (mm)	CONTACT TIME T (μ s)
NYLON	1.8	0.222	0.284	2.16
	1.8	0.342	0.338	1.98
	1.8	1.000	0.520*	1.59
SODA LIME GLASS	5.40	0.222	0.184	0.900
	5.40	0.342	0.218	0.821
	5.40	1.000	0.335	0.660
SAPPHIRE	10.0	0.222	0.143	0.548
	10.0	0.342	0.167	0.515
	10.0	1.000	0.262	0.405

* Computed contact diameter exceeds the diameter of the sphere.

2.2.2 Magnitude and Form of the Interfacial Pressure

The form of the pressure distribution associated with a solid bead impact can be taken to be the Hertzian paraboloidal pressure distribution, however the exact form of the spatial and temporal pressure distribution at the interface between an impacting drop and the target is still not known with any degree of exactness. The following discussion summarizes briefly some of the recent results on this topic. Figure 7 illustrates both computational and experimental evaluations of the interfacial pressure. The pressure, p , is normalized with respect to the water hammer pressure: $p_w = \rho C V_0$ where C is the compressional wave speed of water. It should be noted that the experimental results were based on either disc-shaped drops^(7,8) or a water jet⁽⁹⁾, so there are no direct measurements currently available for a spherical water drop impact. The two computer solutions employed different computational schemes.⁽¹⁰⁻¹²⁾

On the other hand, Kinslow⁽¹³⁾ finds that the maximum interfacial pressures generated using water jets have a maximum value along the axis of symmetry of the impact in accordance with Huang's computations.⁽¹⁰⁾ The early experimental results of Rochester and Brunton⁽⁷⁾ also conformed to Huang's results which were subsequently revised by Hwang as shown in Figure 7. Peterson⁽¹⁴⁾ used the general form of the temporal development of Huang's pressure distribution to analyze water drop impacts in terms of a static Hertzian pressure distribution which corresponds to a spherical indenter impressing an elastic half-space. An interfacial pressure distribution with a maximum at the periphery of the contact zone was originally advanced by Heymann^(15,16).

The maximum pressures at the interface between the two impacting bodies can be calculated from a modified form of the water hammer equation for a deformable target material,

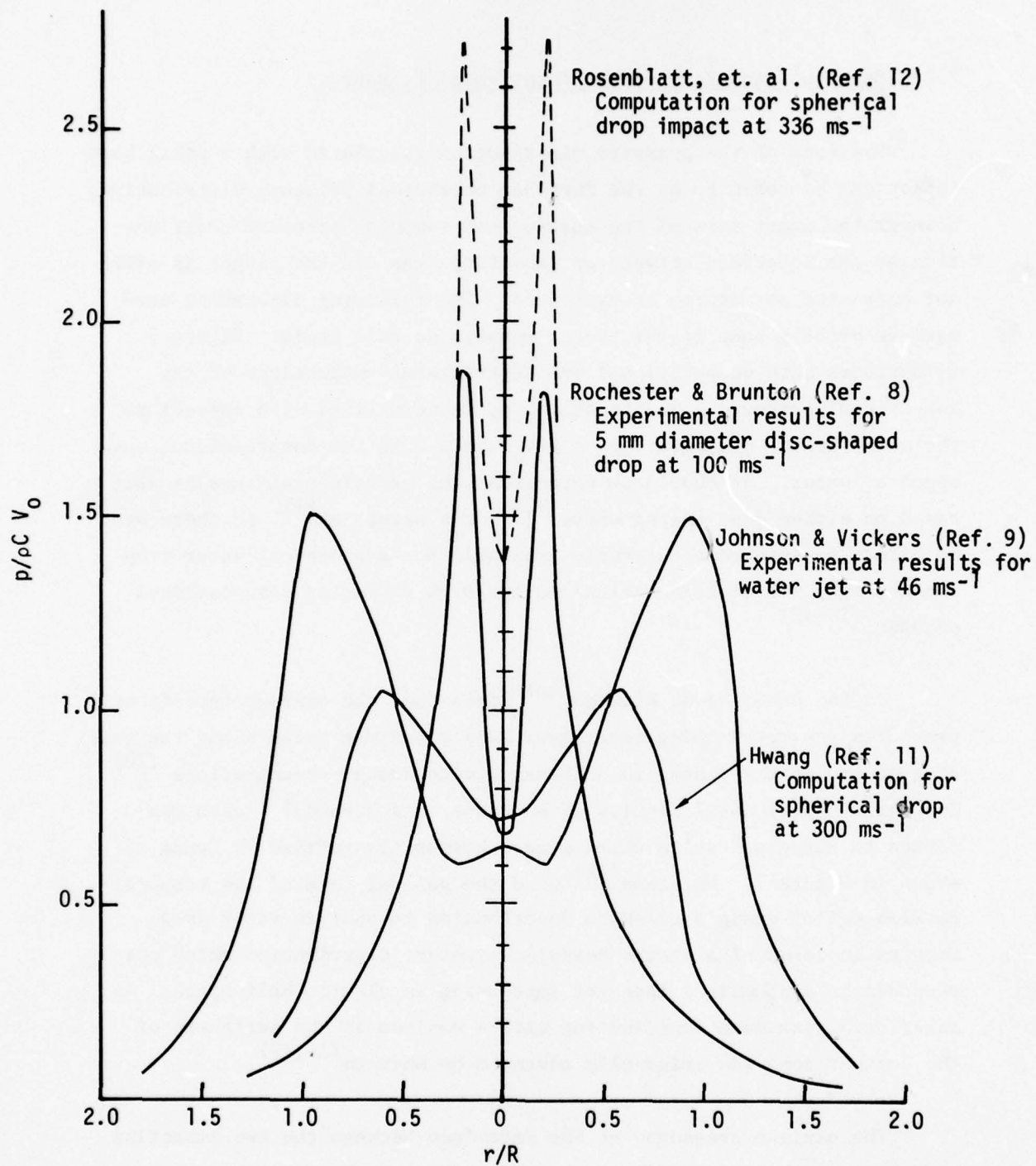


Figure 7. Maximum Interfacial Pressure Distributions
Based on Available Data.

$$P_w = \frac{\rho_1 C_1 V_o}{1 + \frac{\rho_1 C_1}{\rho_2 C_2}} \quad (7)$$

or from the Hertzian theory of impact,

$$P_h = \frac{5}{3 \left(\frac{5}{4} \pi \right)^{4/5}} \cdot \frac{\rho_1 C_1^{8/5} V_o^{2/5}}{\left(1 + \frac{\rho_1 C_1^2}{\rho_2 C_2^2} \right)^{4/5}} \quad (8)$$

When $C_2 \rightarrow \infty$, the impact represents a rigid target; Eq. (7) reduces to the usual form of the water hammer equation.

Eq. (7) is a limiting case of the one-dimensional Hugoniot relations which are based on the application of a uniform pressure distribution to the target. The interfacial pressure is calculated as a function of the impact velocity according to the one-dimensional Hugoniot relations and according to the Hertzian theory of impact for a fused silica target material as summarized in Figure 8. Significant differences are seen in the magnitude of the impact pressures for the two conditions. This fact is not always recognized. For low velocity impacts the Hertzian pressure should provide reasonable results for sapphire, tungsten carbide, and glass beads. The one-dimensional shock wave analysis would only be expected to be applicable at extremely high impact velocities. The Hugoniot for water and nylon are seen to be similar and on the basis of this comparison nylon beads are sometimes used to simulate water drop impacts at moderate to high impact velocities. This simulation deserves further investigation with a careful assessment of several additional factors related to the mechanics of soft particle impacts. The comparisons in Figure 8 demonstrate that the intensity of a solid particle impact is considerably greater at low velocities than for a water drop collision.

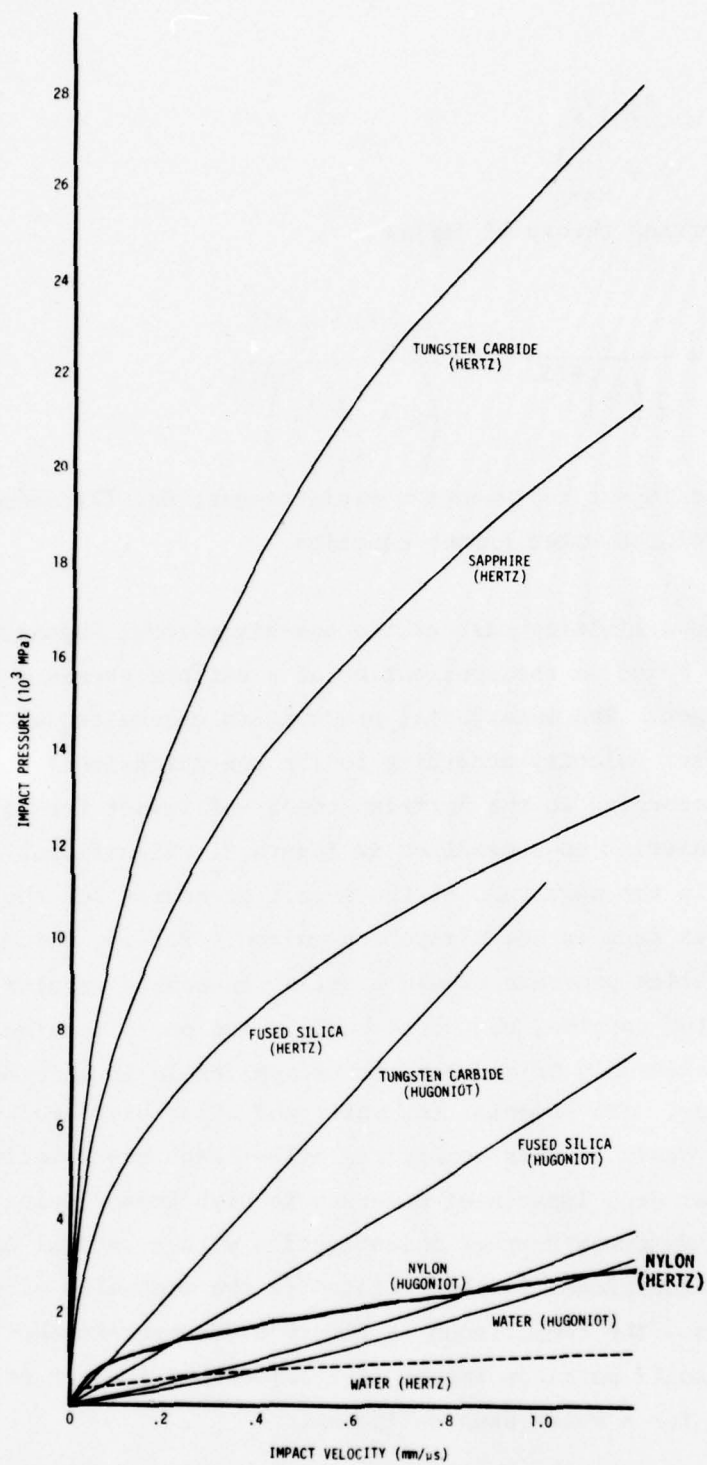


Figure 8. Comparison of Computed Interfacial Pressure Generated by Particle Impacts on Fused Silica.

2.2.3 Stresses in a Half-Space Due to Particle Impacts

The next consideration is the way in which a material body responds to the applied loading. The transient stress states produced in homogeneous, isotropic, elastic materials when impacted by a water drop can be estimated on the basis of the idealized model of the impact event shown in Figure 6a and described by Eq. (4). The pressure is taken to be uniform over the expanding contact zone. The general character and magnitude of the stresses generated for polymethylmethacrylate, soda lime glass, and zinc selenide have been described.⁽²⁾ The temporal development of the radial stress component for soda lime glass is shown in Figure 9. The duration and magnitude of the tensile stresses at and in the vicinity of the surface contribute to the propagation of cracks. An explicit representation for these stresses as a function of time and the spatial coordinates coupled with the critical stress intensity factor and surface flaw distribution for the material can provide information on its susceptibility to initial damage. The stress computations also provide some insights into the local stress states which may interact with the material's microstructure to initiate damage.

As already suggested solid spherical bead impacts can be analyzed on the basis of the Hertzian theory of impact. The form of the Hertzian pressure distribution for two values of the contact zone radius, a , is shown in Figure 10. The total load is taken to be equal to unity. The corresponding uniform pressure distribution is also shown in Figure 10.

The radial stress distributions associated with the surface pressures shown in Figure 10 are given for selected values of the contact zone radius and depth into a soda lime glass specimen in Figures 11 to 14. The stresses in an elastic half-space for the Hertzian and uniform pressure distributions are obtained from Love's solution to these problems.⁽¹⁷⁾ These solutions have been programmed for digital computer

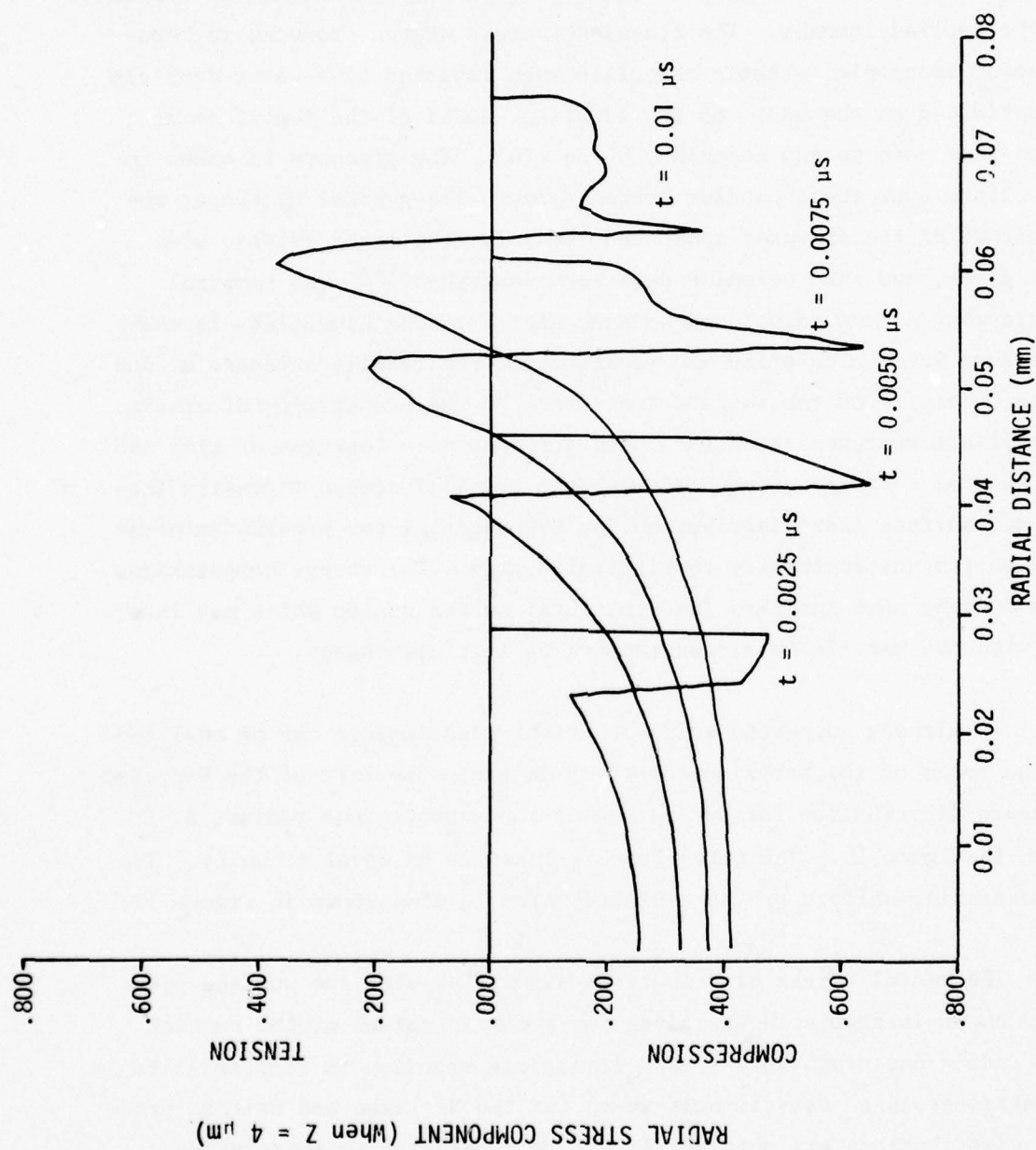


Figure 9. Variation of Radial Stress Component with Time for a 1.8 mm Diameter Water Drop Impacting Soda Lime Glass at 222 ms^{-1}

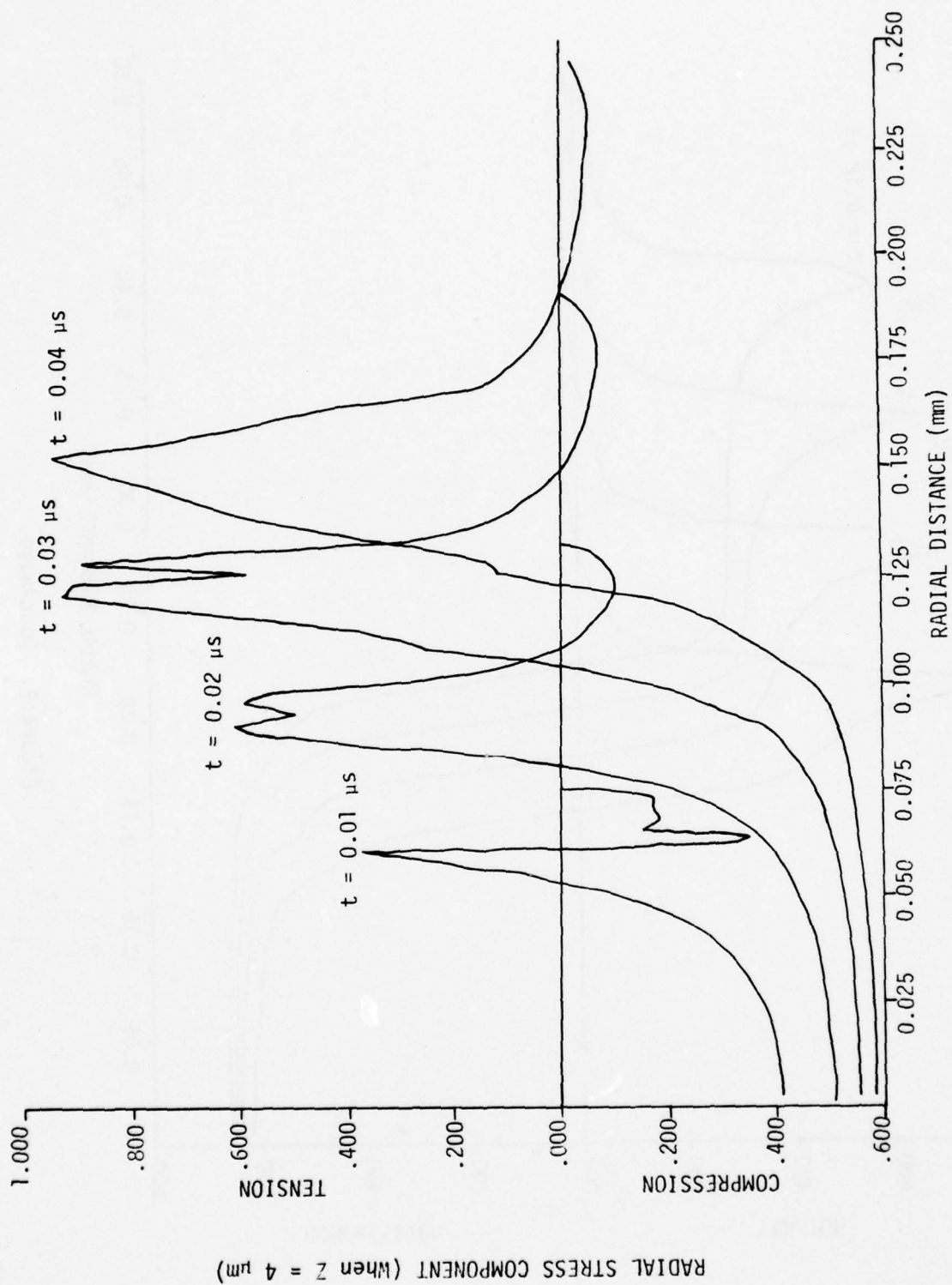


Figure 9. Continued

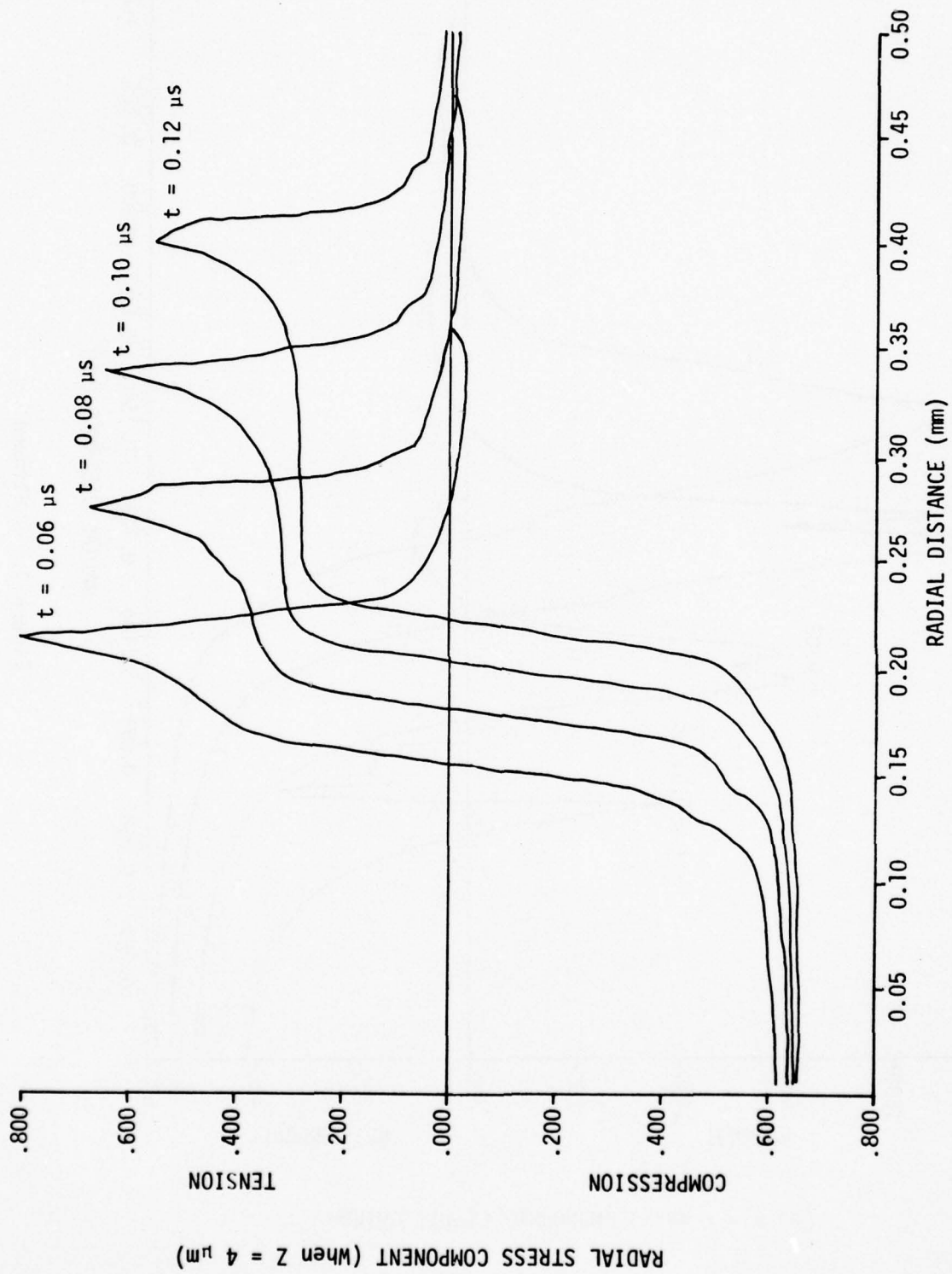


Figure 9. Continued

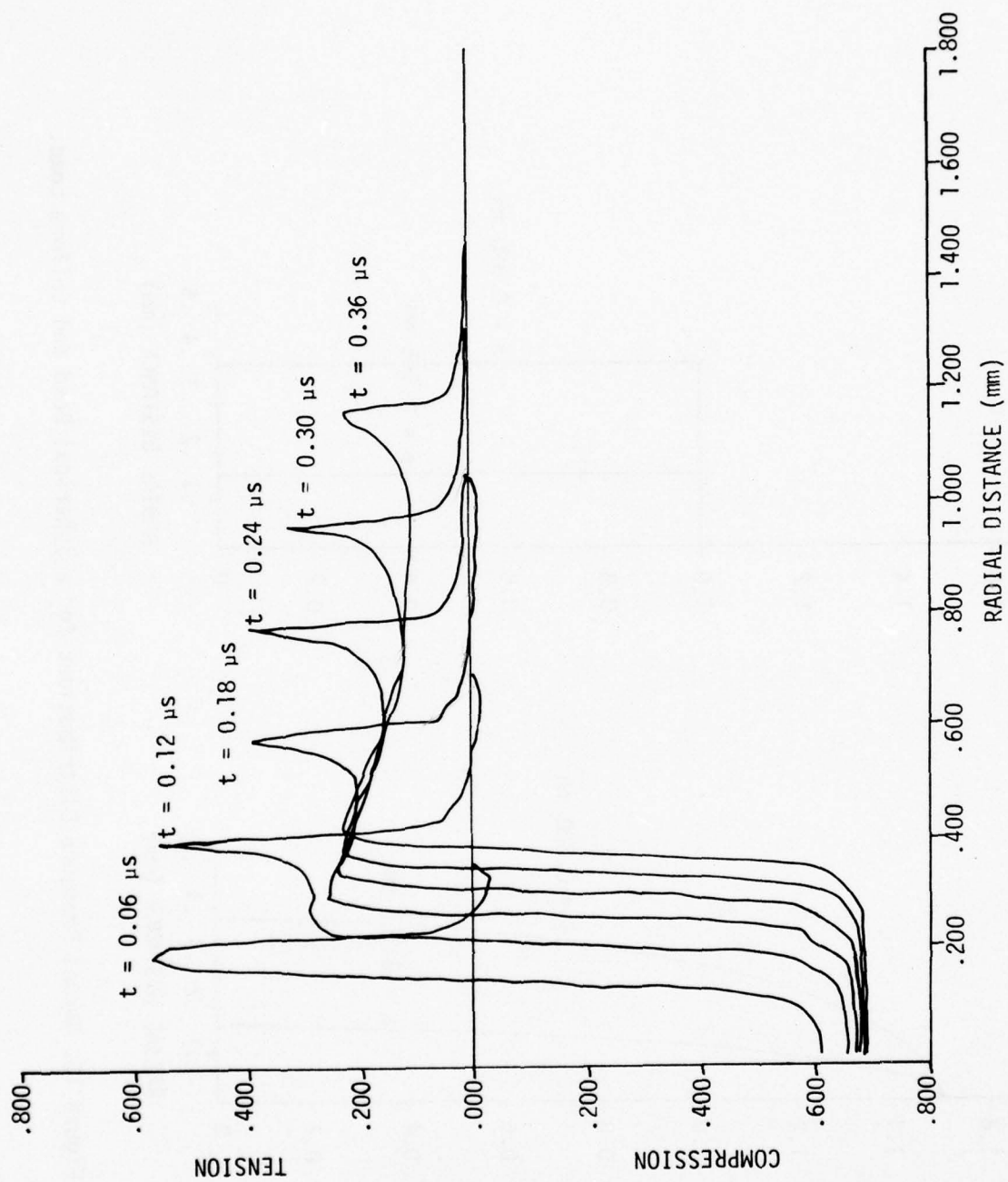


Figure 9. Concluded

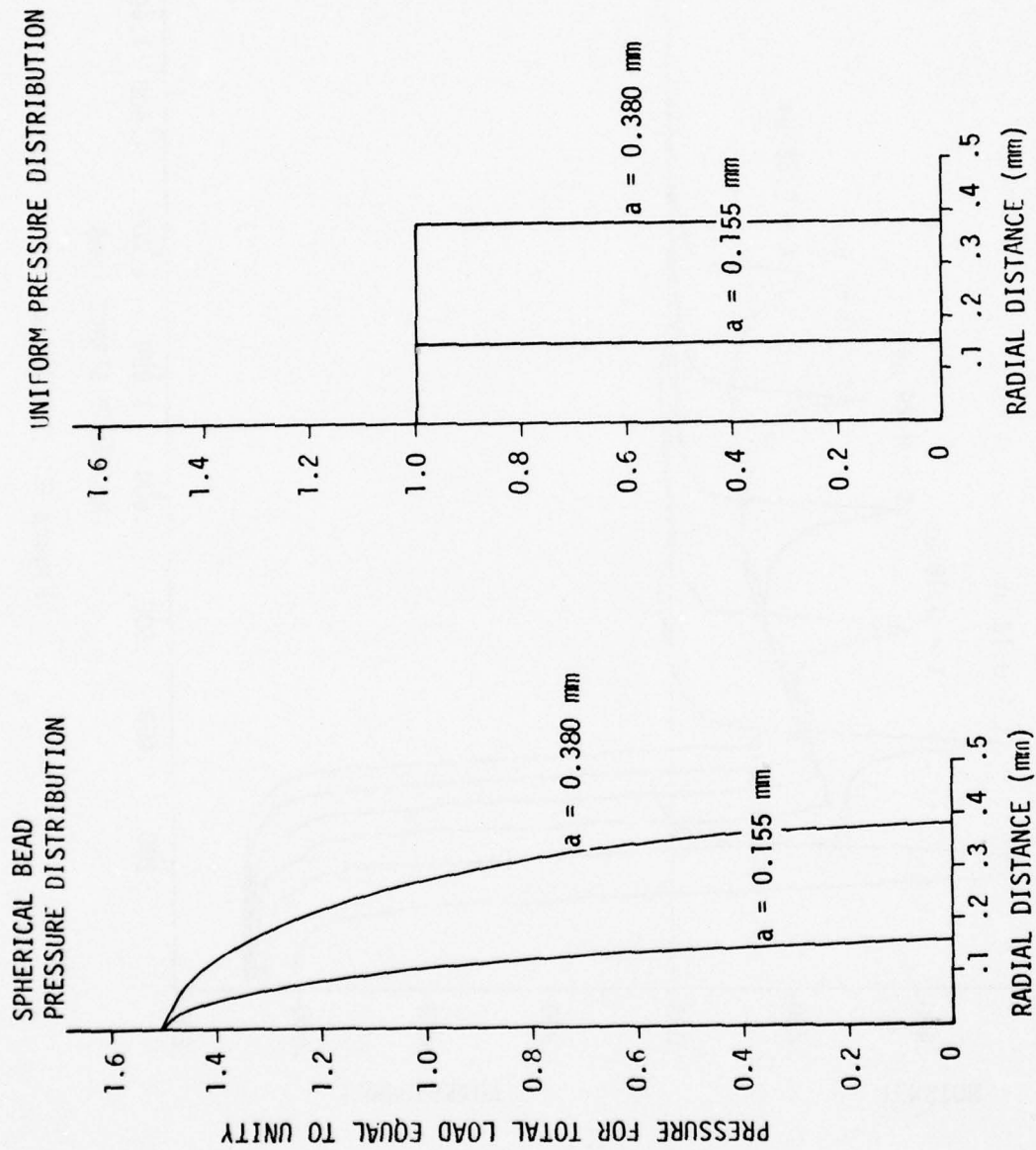


Figure 10. Normal Pressure Distributions for a Spherical Bead and Uniform Load.

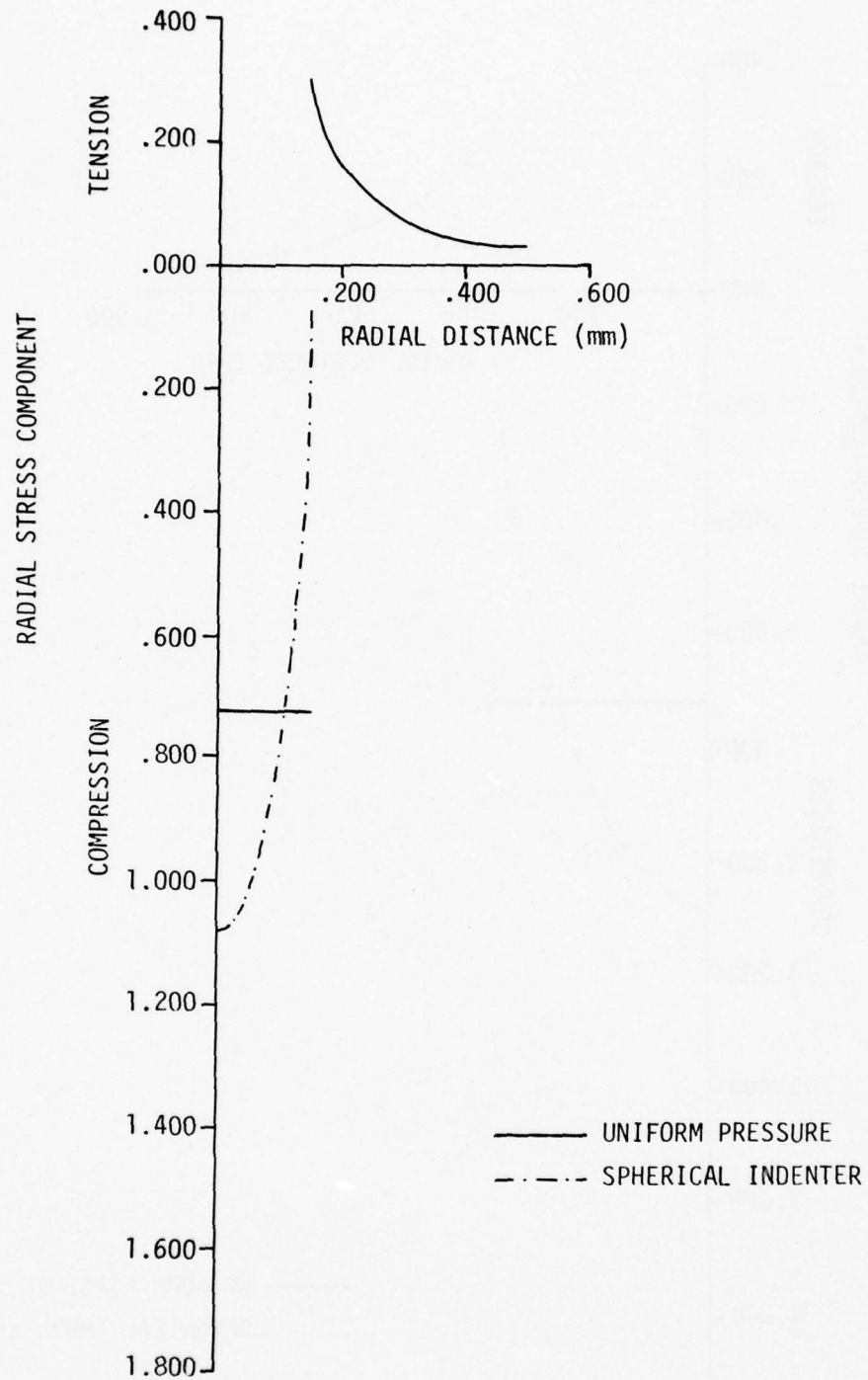


Figure 11. Static Radial Stress Distribution for a Soda Lime Glass Target at the Surface ($Z=0$) When the Contact Zone Radius is 0.155 mm.

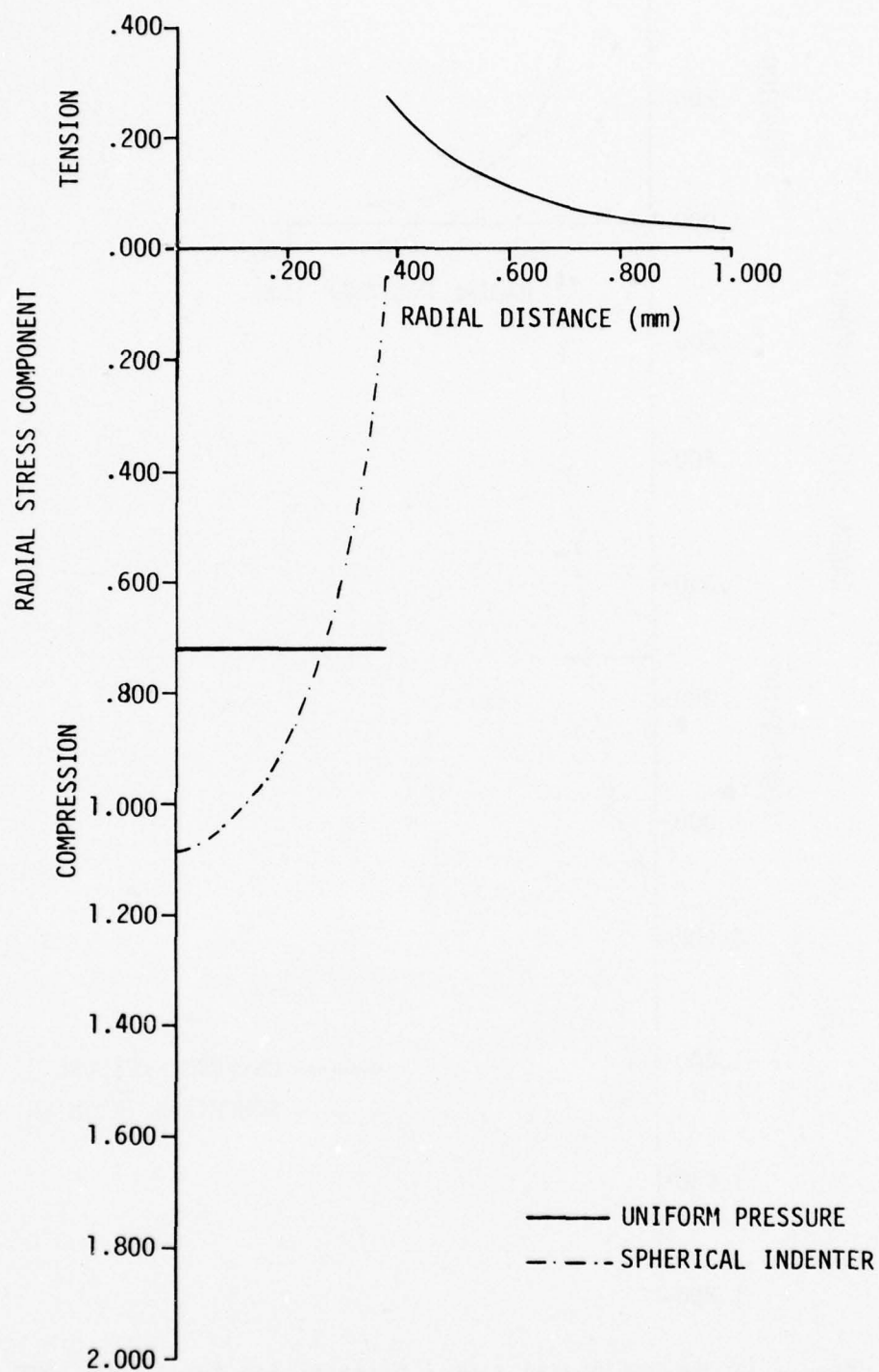


Figure 12. Static Radial Stress Distribution for a Soda Lime Glass Target at the Surface ($Z=0$) When the Contact Zone Radius is 0.380 mm.

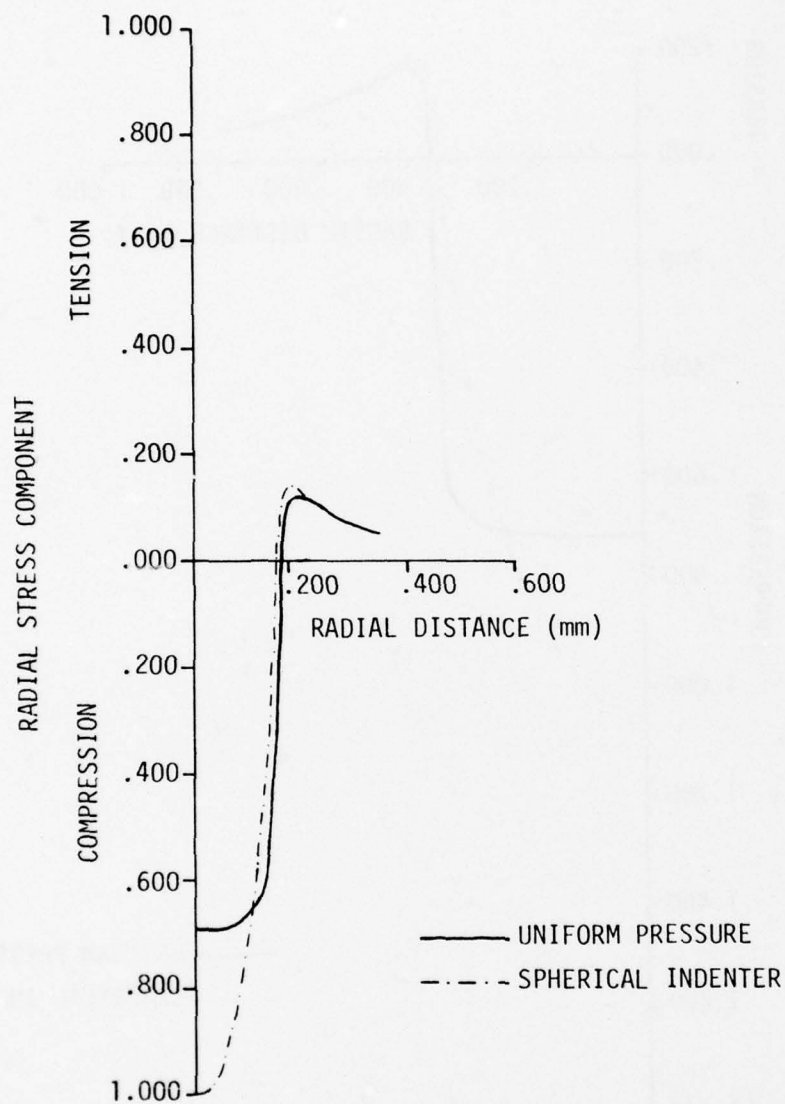


Figure 13. Static Radial Stress Distribution for a Soda Lime Glass Target at $Z = 4 \mu\text{m}$ When the Contact Radius is 0.155 mm.

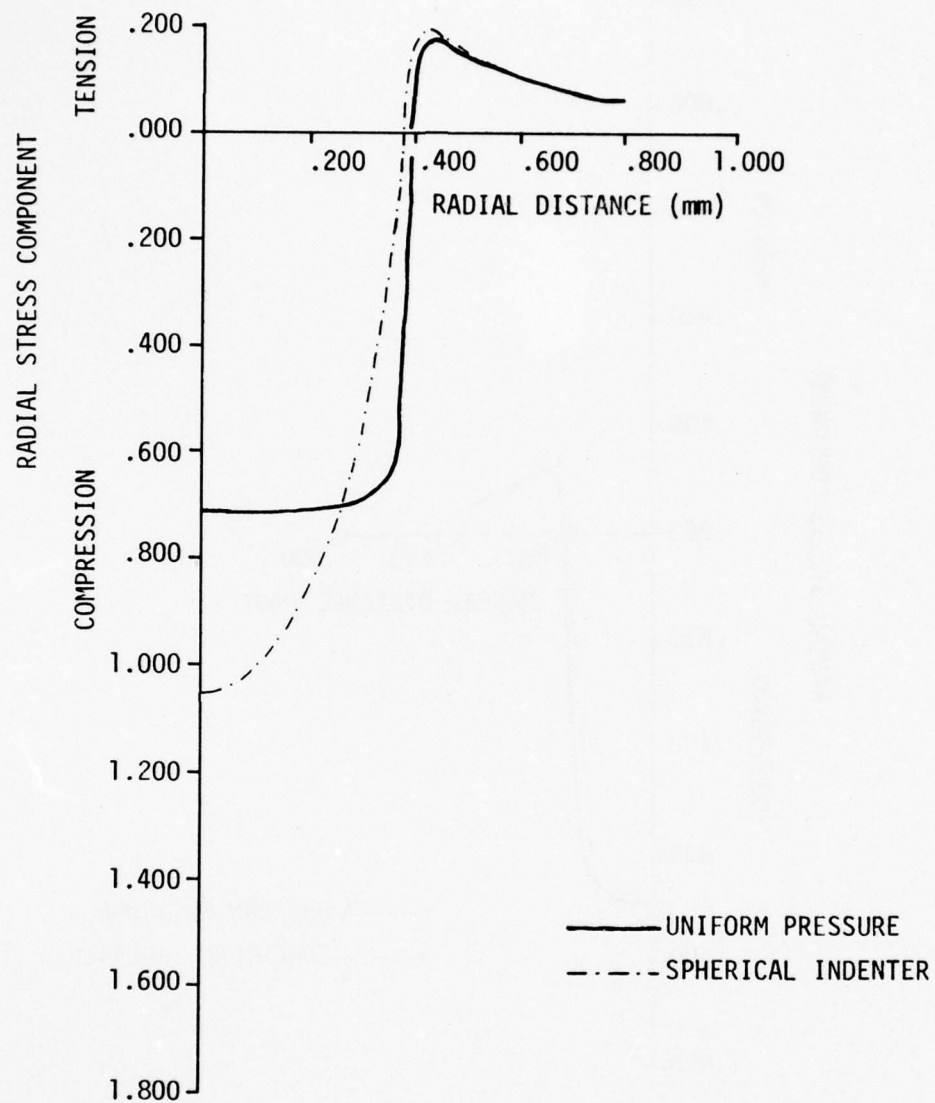


Figure 14. Static Radial Stress Distribution for a Soda Lime Glass Target at $Z = 4 \mu\text{m}$ When the Contact Radius is 0.155 mm.

calculation of the four non-vanishing stress components throughout the half-space. The principal normal and shear stresses can be computed along with the principal stress trajectories. These stress fields and the corresponding results for the water drop impacts will be used to assist in establishing a basis for comparison between water drop and rounded solid particle impacts.

It is immediately observed from Figures 11 to 14 that at the surface ($Z = 0$) the radial stresses are essentially identical outside the contact zone. It is on this basis that the calculation using the dynamic uniform pressure distribution provides useful information on the tensile stresses outside the contact zone for bead impacts. Variations develop in the stress distributions with increasing depth in the vicinity of the boundary of the contact zone, but the two static stress distributions tend to converge with increasing radial distance in accordance with Boussineq's Principle from the theory of elasticity. The radial stresses at a depth of $4 \mu\text{m}$ in Figures 13 and 14 can be compared with those given in Figure 9 for the dynamic case. A direct comparison can be made for a uniform load. When $a = 0.155 \text{ mm}$ in Figure 13 ($t = 0.06 \mu\text{s}$ in Figure 9), the static radial stress distribution shows minimal resemblance to the dynamic values for equal contact radii. It is seen that the dynamic compressive stresses in the vicinity of the impact site are tending toward the static values. After the shear wave has propagated a distance three times the contact radius when $a = 0.380 \text{ mm}$ ($t = 0.36 \mu\text{s}$ in Figure 9) the static and dynamic stress states have converged to a near superposition at radial distances slightly beyond the contact periphery. At larger radial distances the dynamic stresses are still a factor of two greater than the static values. Based on the results from the static and dynamic analysis of a uniform pressure distribution, it is seen that the near-surface radial stress distributions only converge for relatively long dynamic loading durations. If a transient stress analysis was available for the Hertzian pressure distribution, similar observations could be made with regard to the stress distributions for this loading condition.

Calculations of transient stresses due to a liquid drop impact analogous to those described for soda lime glass were undertaken for the (001) orientation of the single crystals listed in Table 2. The application of the idealized solution based on the assumption of an isotropic medium is certainly questionable. While the computations cannot completely accommodate the anisotropic properties of the crystals, they should provide at least reasonable approximations to the stress states prevailing along the $\langle 100 \rangle$ directions. The temporal development of the radial stress component 10 μm below the surface of the crystal-line targets for a 1.8 mm water drop impacting at 342 ms^{-1} (Mach 1) is shown in Figures 15 to 18. The effect of the variation in the wave velocities and elastic properties of the crystals is clearly evident in the extent and form of the stresses generated. The computations are based on a uniform pressure distribution of unit magnitude. The lower wave speed for Ge is seen to produce a higher relative amplitude radial tensile stress acting over a much shorter radial distance than in the case of Si.

The effect of reasonable water drop impact velocities for a single moderately large value of the contact radius is shown in Figures 19 to 22. As the impact velocity increases the contact time prior to lateral outflow is decreased, so the stresses cannot propagate as far from the impact site for equal values of the contact radius. The general form of the normalized curves for Si and MgO at 222 and 342 ms^{-1} are nearly identical so only one of these curves is plotted in Figures 21 and 22. The wave velocities are comparable for these two crystals and being high the near-field effects are not that significant for the two values of the velocities selected when $a = 0.380 \text{ mm}$: a relatively large value. The equivalent static stress distribution is also plotted in Figures 19 to 22 for comparison. Only Poisson's ratio, ν , is required in the static computation (for a uniform pressure of unit magnitude distribu-

Table 2. Elastic Properties of Crystals

	DENSITY (g/cc)	ELASTIC CONSTANTS ($\times 10^5$ MPa)			WAVE VELOCITIES IN $\langle 100 \rangle$ DIRECTION (mm/ μ s)	
		C_{11}	C_{12}	C_{44}	C_ℓ	C_s
CaF ₂	3.18	1.66	0.49	0.36	7.22	3.36
Ge	5.32	1.29	0.48	0.67	4.92	3.55
Si	2.33	1.68	0.65	0.80	8.50	5.86
MgO	3.58	2.87	0.88	1.54	8.96	6.56

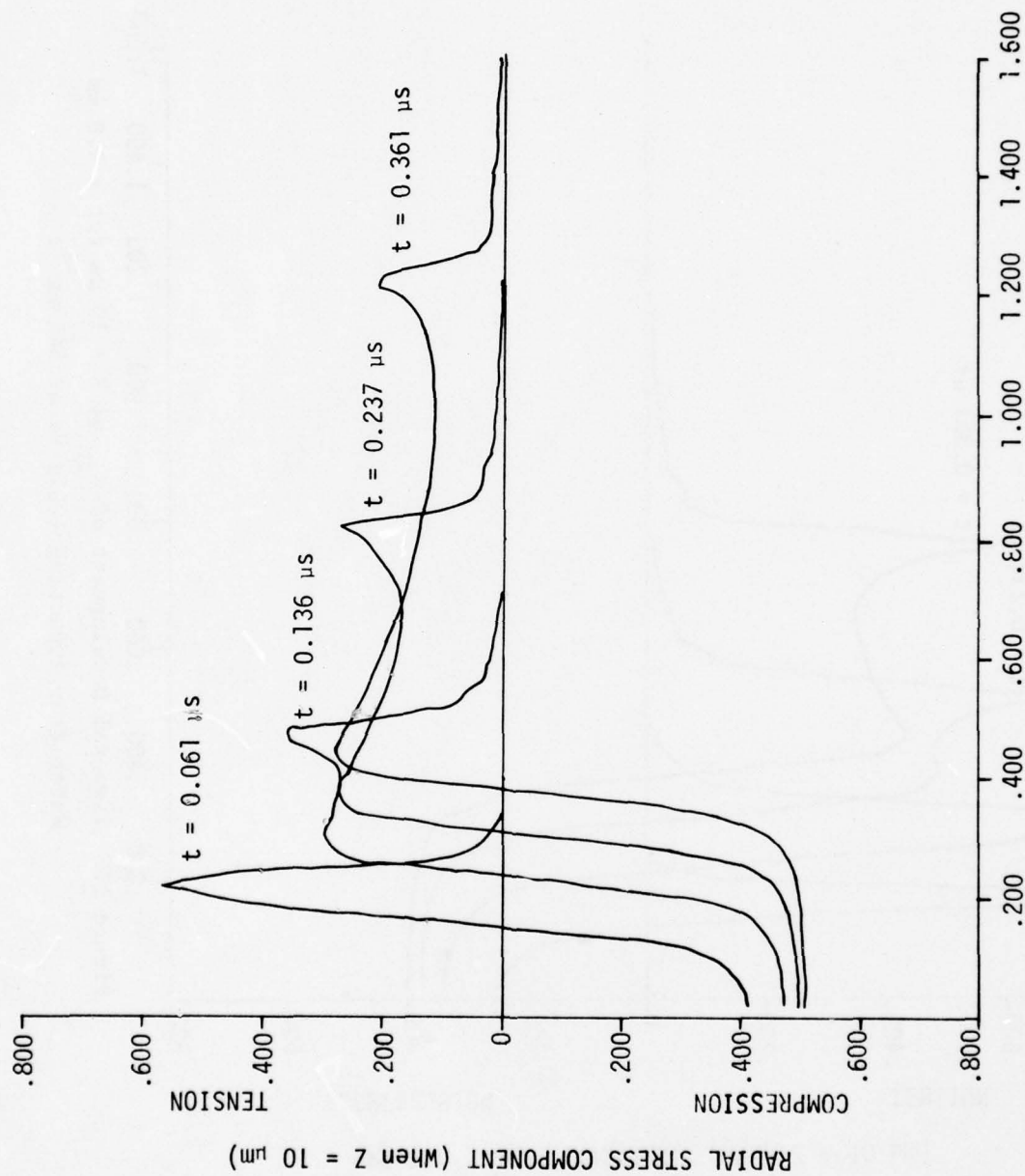


Figure 16. Temporal Development of σ_{rr} at $Z = 10 \mu\text{m}$ for a 1.8 mm Water Drop Impacting (001) Si at 342 ms^{-1} .

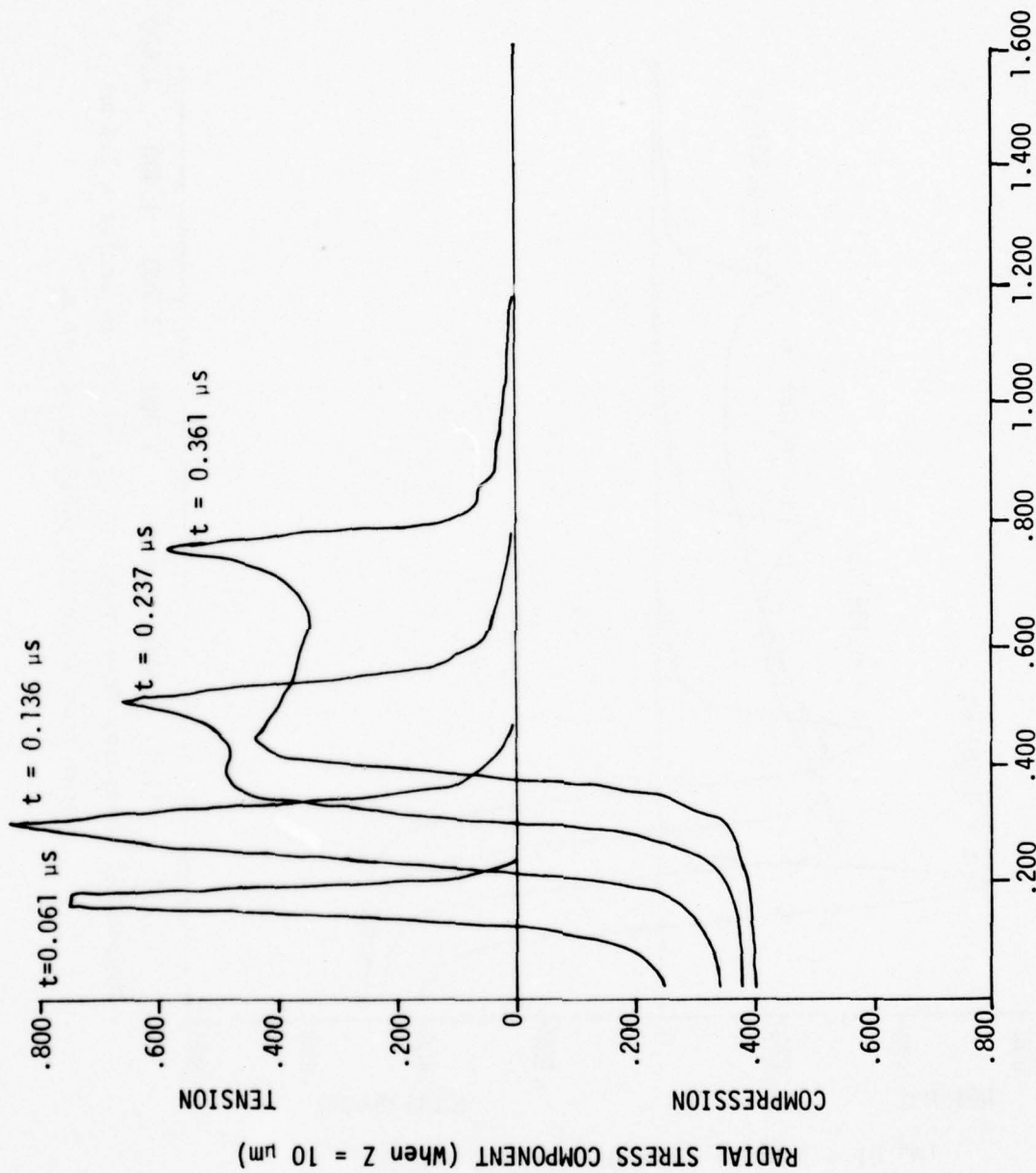


Figure 17. Temporal Development of σ_{rr} at $Z = 10 \mu m$ for a 1.8 mm Water Drop Impacting (001) Ge at $342 ms^{-1}$.

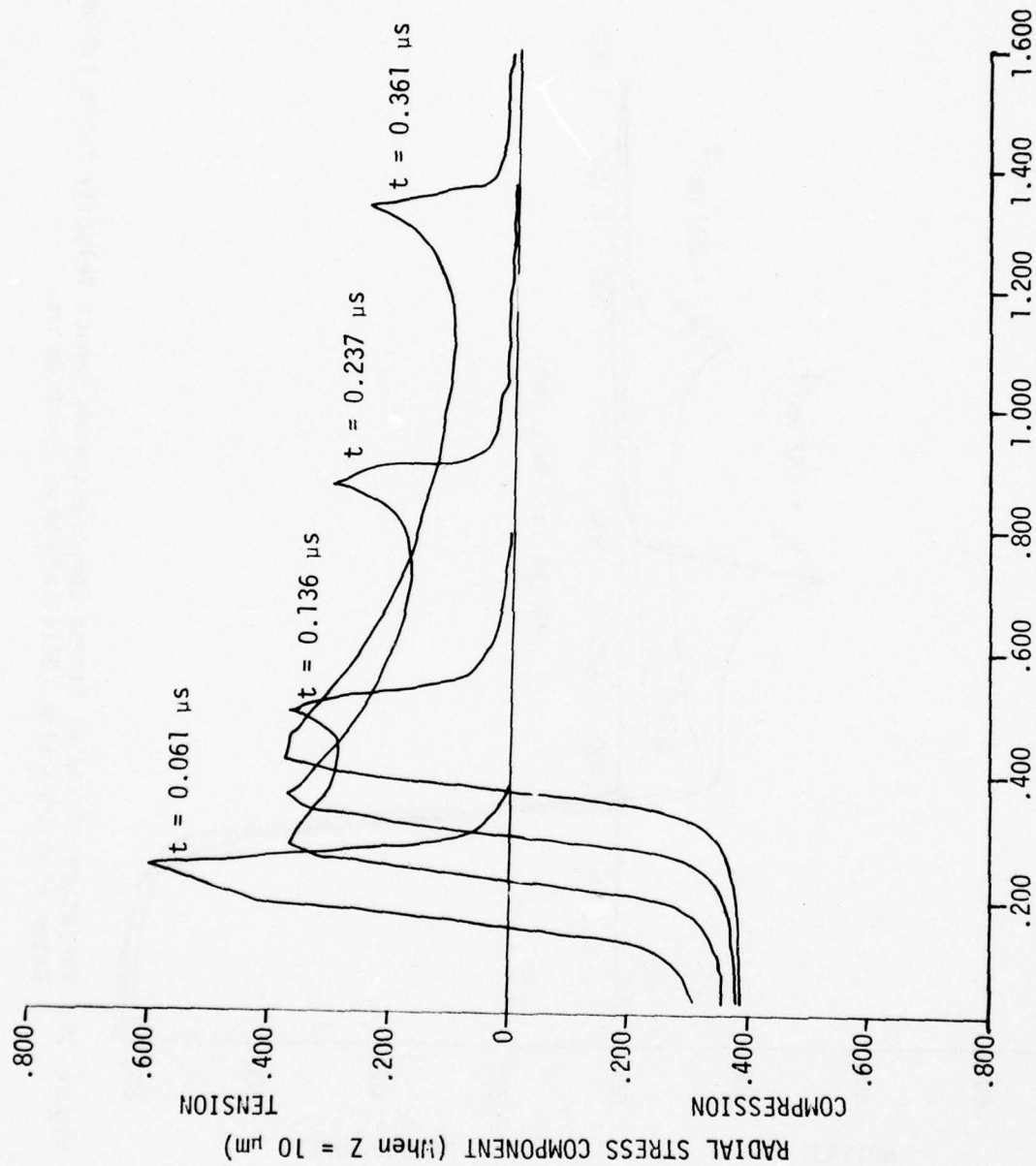


Figure 18. Temporal Development of σ_{rr} at $Z = 10 \mu\text{m}$ for a 1.8 mm Water Drop Impacting (001) MgO at 342 ms^{-1} .

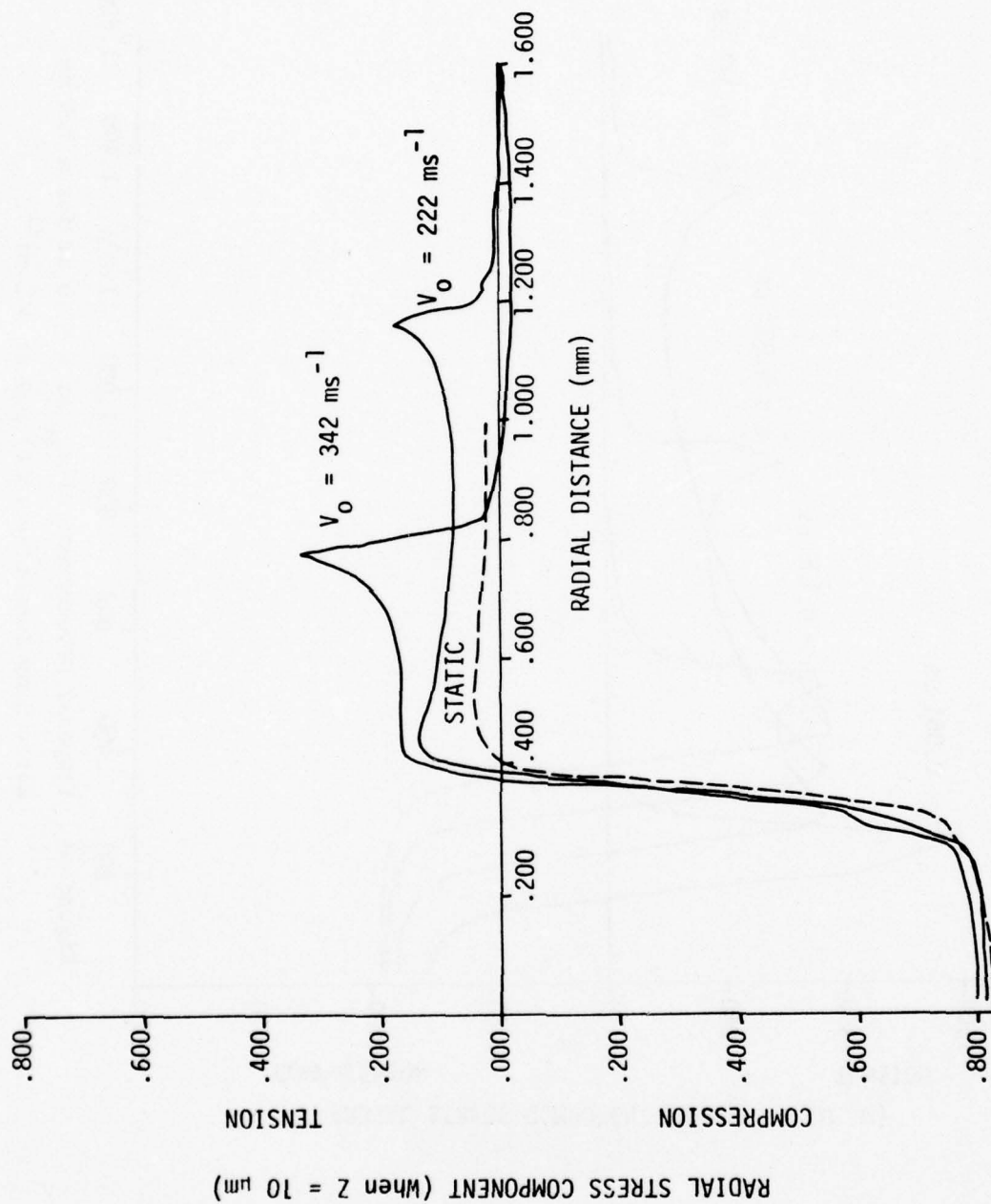


Figure 19. Variation of Radial Stress Component with Impact Velocity for a 1.8 mm Water Drop Impacting (001) CaF_2 When $a \approx 0.38 \text{ mm}$.

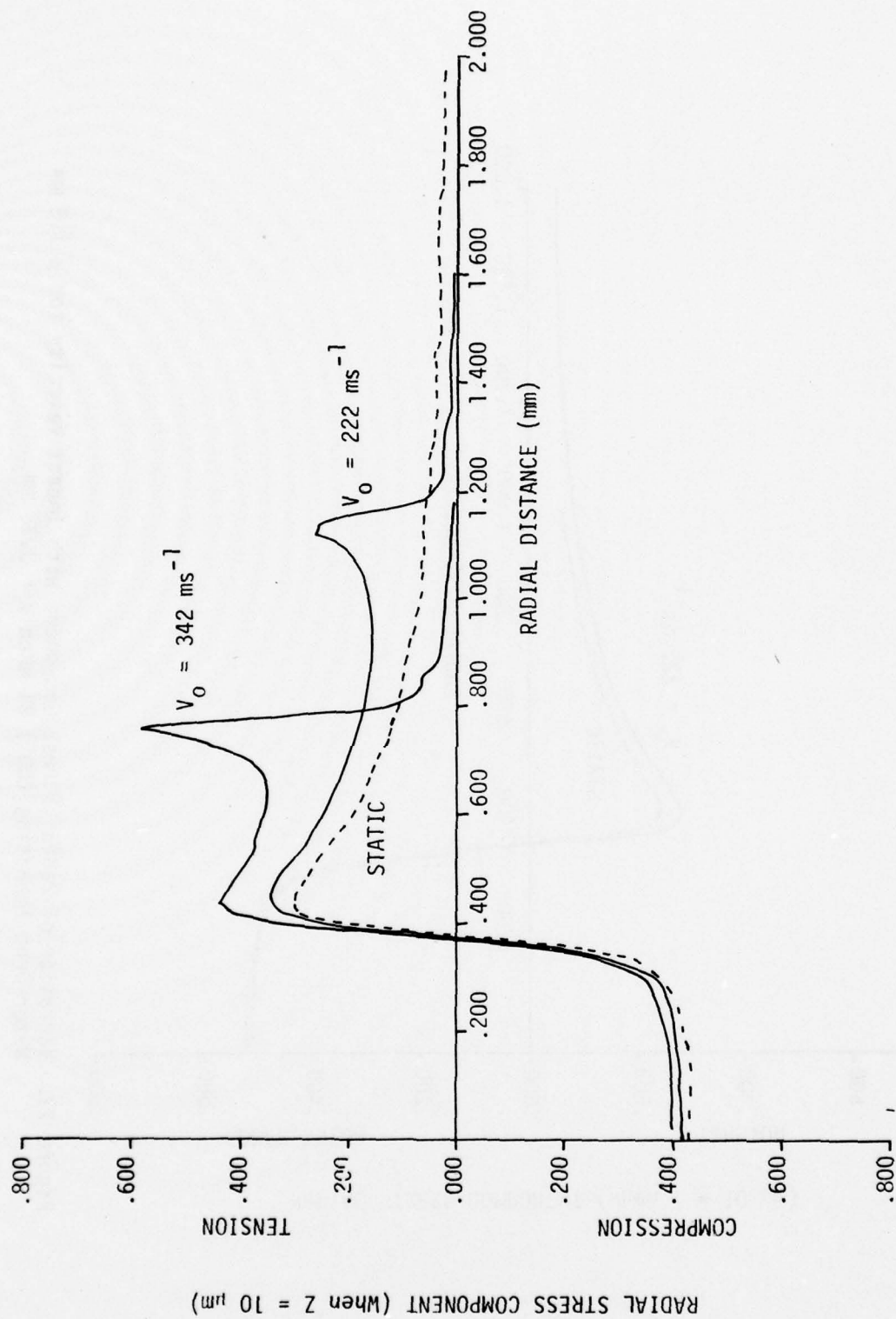


Figure 20. Variation of Radial Stress Component with Impact Velocity for a 1.8 mm Water Drop Impacting (001) Ge when $a = 0.38$ mm.

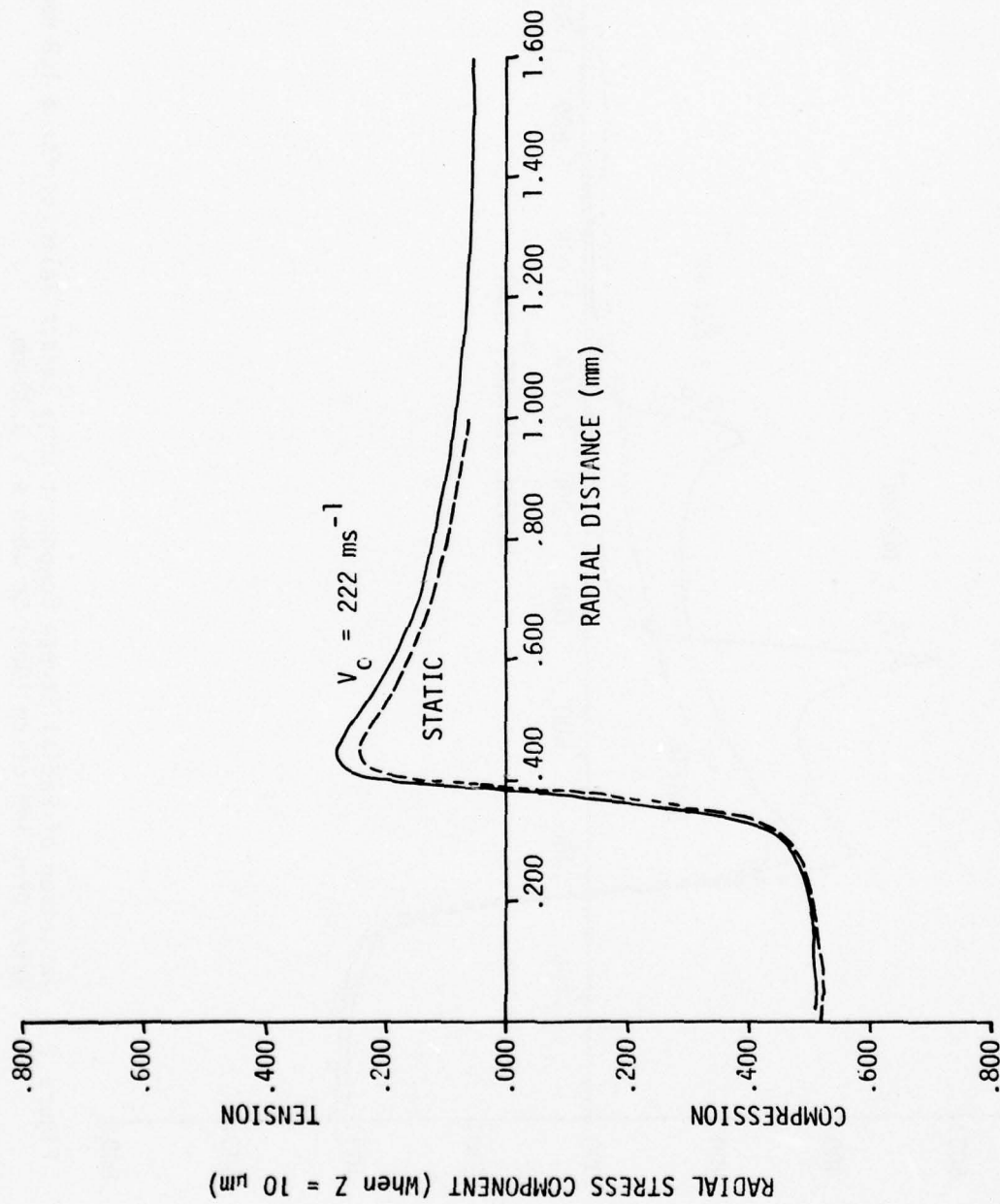


Figure 21. Variation of Radial Stress Component with Impact Velocity for a 1.8 mm Water Drop Impacting (001) Si when $a = 0.38 \text{ mm}$.

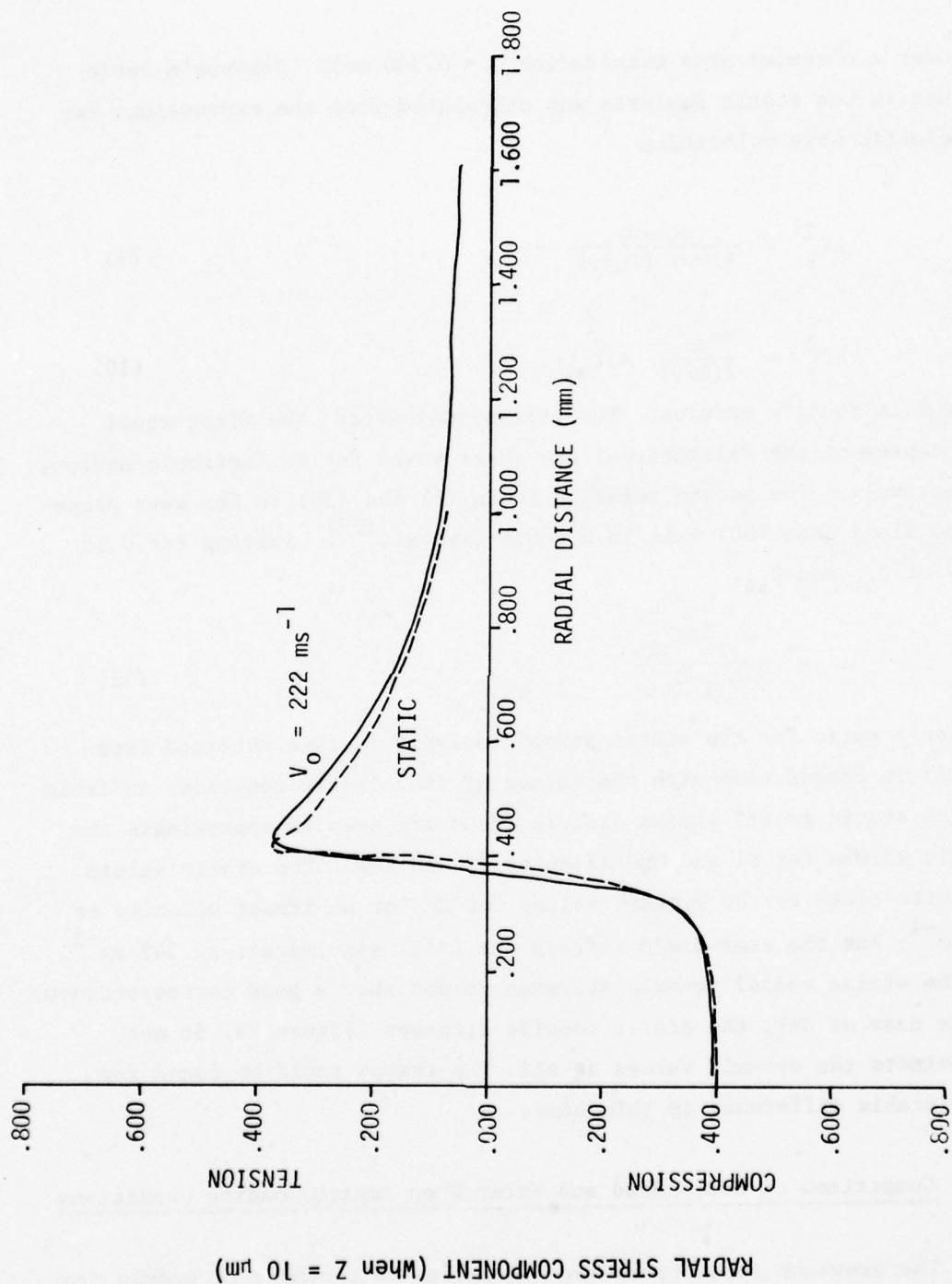


Figure 22. Variation of Radial Stress Component with Impact Velocity for a 1.8 mm Water Drop Impacting (001) MgO when $a = 0.38 \text{ mm}$.

ted over a circular area with radius $a = 0.380$ mm). Poisson's ratio for use in the static analysis was calculated from the expressions for the elastic wave velocities

$$\rho C_l^2 = \frac{E(1-\nu)}{(1+\nu)(1-2\nu)} = C_{11} \quad (9)$$

$$\rho C_s^2 = \frac{E}{2(1+\nu)} = C_{44} \quad (10)$$

where E is Young's modulus. The expressions after the first equal sign represent the dilatational and shear waves for an isotropic medium, respectively. The second relation in Eq.(9) and (10) is for wave propagation along the $\langle 100 \rangle$ axis in a cubic crystal.⁽¹⁸⁾ Solving for ν in terms of C_{11} and C_{44} ,

$$\nu = \frac{C_{11} - 2C_{44}}{2(C_{11} - C_{44})} \quad (11)$$

Poisson's ratio for the static stress analysis is then obtained from Eq.(11) in conjunction with the values of the elastic constants in Table 2. The static radial stress distributions are seen to approximate the dynamic values for Si and MgO (Figures 21 and 22). The static values are quite close to the dynamic values for Ge for an impact velocity of 222 ms^{-1} ; but the near-field effects are still significant at 342 ms^{-1} , and the static radial tensile stresses do not show a good correspondence. In the case of CaF_2 the static tensile stresses (Figure 19) do not approximate the dynamic values at all. No reason could be found for the sizeable difference in this case.

2.2.4 Comparison of Solid Bead and Water Drop Impact Loading Conditions

The previous subsections have investigated a number of models describing various aspects of the mechanics of particle impacts. Obviously, there are other approaches which could be used, however the main fea-

tures of the collision appear to be represented by the comparatively simple analyses presented. In general, the comparison of the results from the idealizations of the collision process with more sophisticated computer models has been most favorable. Many of the computations presented have been used, possibly in a more restricted form, in the literature on particulate impacts and erosion.

The results in the previous subsections are provided to indicate the nature of the impact regimes for water drops, nylon beads, and sapphire beads which are used in the experiments described in Section 3.0. The analytical approximations for water drops and sapphire beads are reasonably representative of the impact event. The material response of nylon is not adequately described by an elastic sphere or a perfectly compressible body, so nylon bead impacts cannot be completely characterized by the models introduced here. According to the Hertzian calculation of the contact area in Table 1, the diameter of the contact zone exceeds the diameter of the nylon sphere when the impact velocity is somewhat less than 1000 ms^{-1} . Actually the analysis is invalid at much lower velocities according to the basic geometric approximations made in the derivation of the Hertzian equations. The computed values in Table 1 for soda lime glass and sapphire appear reasonable, although the soda lime glass beads would fragment and possibly be pulverized at velocities less than 1000 ms^{-1} . These restrictions in the physical as opposed to the idealized impact process should be realized in order to avoid drawing incorrect conclusions from the straightforward application of the computations which can now be carried out.

Rudimentary equivalence criteria can be established between water drop and solid particle collisions based on the analytical expressions described in terms of the applied loading function. The problem is posed as follows. A solid particle collision with a plane surface will be considered equivalent to a water drop impact if the mean pressures

developed over the contact zone and the maximum contact radii are equal. For the moment the form of the pressure distribution and the time required to reach the maximum contact radius in each case are ignored. Using Eq.(7) and (8),

$$P_w = P_H$$

$$\frac{\rho_w C_w V_w}{1 + \frac{\rho_w C_w}{P_t C_t}} = 0.556 \frac{\rho_p C_p^{8/5} V_p^{2/5}}{\left(1 + \frac{\rho_p C_p^2}{\rho_p C_t^2}\right)^{4/5}} \quad (12)$$

where the subscripts w, p, and t refer to the water drop, solid particle, and target respectively. Eq.(12) is solved for V_p , the velocity of the solid particle. The left-hand-side of Eq.(12) should actually be the Hugoniot for water, since C_w is not constant but is a nonlinear function of the particle velocity. The Hugoniot relation for obtaining P_w was used in the computations carried out here. This is an important factor for water drop impacts at velocities above 200 m/s.

The second equivalence condition is stated explicitly by equating the contact radius for the water drop prior to lateral outflow to the Hertzian expression in Eq.(2) for the maximum contact radius for solid particle impacts,

$$a_w = 1.315 \left(\frac{1}{C_p^2} + \frac{\rho_p}{\rho_t} \frac{1}{C_t^2} \right)^{1/5} V_p^{2/5} R_p \quad (13)$$

Since a_w is specified, R_p , the radius of the equivalent solid particle, is determined from Eq.(13). The contact radius a_w is related to the water drop diameter, but the drop diameter does not have to be prescribed until specific test conditions are examined.

The stated equivalence criteria then provide the size of the solid sphere and its impact velocity. Values of R_p and V_p are computed from the general format outlined in Eq.(12) and (13) and are summarized in Table 3 for the range of particle impact conditions relevant to the experimental results presented in Section 3.0. The general form of the data in Table 3 can be anticipated from the curves in Figure 8. It is immediately evident that the equivalent glass and sapphire bead impacts occur at very low impact velocities. Based on this analysis the intensities of the glass and sapphire bead impacts at 25 ms^{-1} are much greater than that of a water drop impact at velocities up to 1000 ms^{-1} . Nylon impact velocities are more in accord with the velocity range for water, however as already stated the applicability of the Hertzian and the Hugoniot relations is questionable. Illustrative examples based on Table 3 will be given in order to obtain some idea of how well the imposition of these relatively general conditions can be satisfied.

Let a water drop with diameter $2R_w = 1.8 \text{ mm}$ impact a glass target over the velocity range listed in Table 3, then a_w probably lies within the limits of 0.155 to 0.380 mm used in Section 2.2.3. When $a_w = 0.155 \text{ mm}$, a 9 mm diameter sapphire bead would have to be used for $V_w = 222 \text{ ms}^{-1}$ and a 1.33 mm sapphire bead for $V_w = 1000 \text{ ms}^{-1}$. When $a_w = 0.380 \text{ mm}$, the solid bead diameters are increased in direct proportion to the radius of the contact zone. Other impact conditions are summarized in Table 4.

Now that the equivalent conditions for the contact radius and the impact velocities have been evaluated, the time required for a water drop and a solid sphere to reach the same value of the contact radius can be evaluated from Eq.(4) and (2) respectively. The computed values for the contact times listed in Table 4 for a water drop impact and an equivalent solid bead impact indicate differences of more than an order of magnitude: generally closer to two orders of magnitude. The contact zone for a water drop is seen to expand much more rapidly than for the solid particle. This is a significant difference between the two modes of loading.

Table 3. Equivalent Conditions Between Water Drop
and Solid Particle Impacts on a Glass Plate

WATER DROP IMPACT VELOCITY (m/s)	PRESSURE P_w (MPa)	PARTICLE MATERIAL	V_p (m/s)	R_p/a_w
222	360	Nylon	160. (Hugoniot)	7.96
			26.2 (Hertz)	16.4
		Glass	0.15	18.0
		Sapphire	.046	29.0
342	620	Nylon	265. (Hugoniot)	6.51
			103. (Hertz)	9.47
		Glass	0.59	10.38
		Sapphire	.18	16.75
1000	2430	Nylon	855. (Hugoniot)	4.06
			3090. (Hertz)	2.43
		Glass	17.7	2.66
		Sapphire	5.4	4.29

Table 4. Solid Particle Impact Conditions Equivalent to a
1.8 mm Water Drop Impacting a Glass Plate

WATER			GLASS			SAPPHIRE		
V_w (m/s)	a_w (mm)	t (μ s)	V_p (m/s)	R_p (mm)	$T/2$ (μ s)	V_p (m/s)	R_p (mm)	$T/2$ (μ s)
222	0.155	0.060	0.15	2.79	14.1	0.046	4.50	23.4
222	.380	.361	0.15	6.85	34.6	.046	11.03	57.4
1000	0.155	0.013	17.7	0.412	0.805	5.4	0.665	1.335
1000	0.380	0.080	17.7	1.01	1.97	5.4	1.63	3.22

THIS PAGE INTENTIONALLY BLANK

3.0 EXPERIMENTAL RESULTS AND DISCUSSION

The general rain erosion behavior of (001) CaF_2 , (001) Si, and (001) MgO has been studied for short exposures to multiple 1.8 mm water drop impacts at 222 and 260 ms^{-1} . Most of the specimens used in this investigation are polished to acceptable optical tolerances, however residual grinding flaws are of major importance for damage initiation in a rain environment in the stated velocity range. At subsonic impact velocities these sites influence the erosion process in the crystals examined which have a higher tolerance for crystallographic fractures.

The microstructural failure modes and fractures in a rain environment are being investigated and compared to the damage produced by impressing a Vickers hardness indenter, a 1 mm spherical indenter, and impact by 1 mm nylon and sapphire beads near the fracture threshold velocities. In previous work the spherical indenter proved very effective in ranking the erosion resistance of a series of oxide-based glasses whereas other fracture data and material parameters showed little correspondence.⁽¹⁹⁾ The relevance of the quasistatic indentation evaluations and associated failure mechanisms have therefore been explored for the crystalline materials in this program. The nylon bead impacts are included since deformable solid particle impacts have been used as a simulation technique for water drop impacts at higher impact velocities.⁽²⁰⁾ The merit of this approach is being investigated for relevant impact conditions. The analyses in Section 2.2.4 indicate some of the criteria which must be satisfied if a correspondence is to be established between liquid drop and solid bead impacts. The impact conditions used in the experimental program were based in part on the available facilities and do not represent an approximation to the level of correspondence which may be possible.

The results presented are of an exploratory nature. Future work in this area will focus on the critical issues uncovered during this

initial survey of the failure modes in the crystals of interest.

3.1 CALCIUM FLUORIDE

Specimens of single crystal calcium fluoride have been subjected to multiple water drop impacts, nylon and sapphire bead impacts and quasistatic indentation. Calcium fluoride displayed markedly different response under all test conditions behaving in a ductile manner for quasistatic bead indentations and dynamic sapphire bead impacts but brittle fracture and surface flaws are responsible for damage initiation in a rain environment.

3.1.1 Multiple Water Drop Impacts

A specimen of (001) oriented CaF_2 was exposed to the multiple water drop environment in the AFML rain erosion facility at 222 ms^{-1} . Although relatively poor resistance was anticipated in view of the low micro-hardness values, exposures to water drop impacts of $15/\text{cm}^2$ and $1000/\text{cm}^2$ produced little degradation. Optical microscopy of the briefly exposed surface before and after etching did not reveal any damage which could be attributed to the rainfield. Slight degradation could be identified for the longer exposure before etching. The most readily observed feature was a granular deposit. This could be physically removed by exerting a large shear force during wiping but resisted dissolution by soaking in pure solvents or soap solutions (testing for residual cellulose acetate tape or mineral deposits). It could be readily dissolved in acid without influencing the underlying substrate and is believed to be an oxide or carbonate deposit formed during exposure.

Three forms of damage were observed sparsely distributed over the exposed surface: small cavities associated with lateral spall, small lateral fracture systems before dislodgement of material, and small crack arrays. These forms of damage are similar to those previously observed

on germanium exposed to greater than 70 impacts/cm² except that the crack array dimensions are much larger on germanium.⁽²¹⁾ All erosion damage was confined to microscopic dimensions and far more impacts would be required to develop significant damage networks. Two views of the eroded surface are shown in Figures 23 and 24.

Application of a dislocation etchant to the eroded surface revealed most of it contained too low a dislocation density to produce etch pits. ~~Although not all~~ reported dislocation etchants produce etch pits on polished (100) surfaces, the procedures used here produce well-defined rosettes of etch pits about microhardness indentations for this crystal orientation. A low density of pits was found to be associated with the arrays of surface cracks as shown in Figure 25. Since clusters of these pits were found only adjacent to the surface fractures, it is assumed they arose from slip associated with fracture. In view of the large number of impacts the specimen received, 1.8 mm water collisions at 222 ms⁻¹ do not appear to generate a sufficiently large stress intensity-duration profile for slip in undeformed CaF₂. The effectiveness of the water drop impacts in propagating slip bands could not be ascertained from this test series. However slip has been observed at fracture sites in quasistatic flexure tests.⁽²²⁾

Compact fracture arrays of similar shape have been observed also on eroded surfaces of a variety of brittle materials including a variety of glasses⁽¹⁹⁾, germanium⁽²¹⁾, and silicon (as reported in Section 3.2). Since these arrays do not relate in an obvious way to the impact geometry, it is assumed that the arrays result instead from the gradual enlargement of residual grinding damage introduced during surface preparation. Optical surfaces impose rigorous flatness requirements which limit the final polishing steps and this limitation together with economic considerations suggest small fissures (probably covered over with polishing debris) exist in the as-polished surfaces. Such damage is well-documented for silicon and implicitly assumed in a number of discussions of glass surfaces. Such fissures could undergo subcritical growth during repeated drop

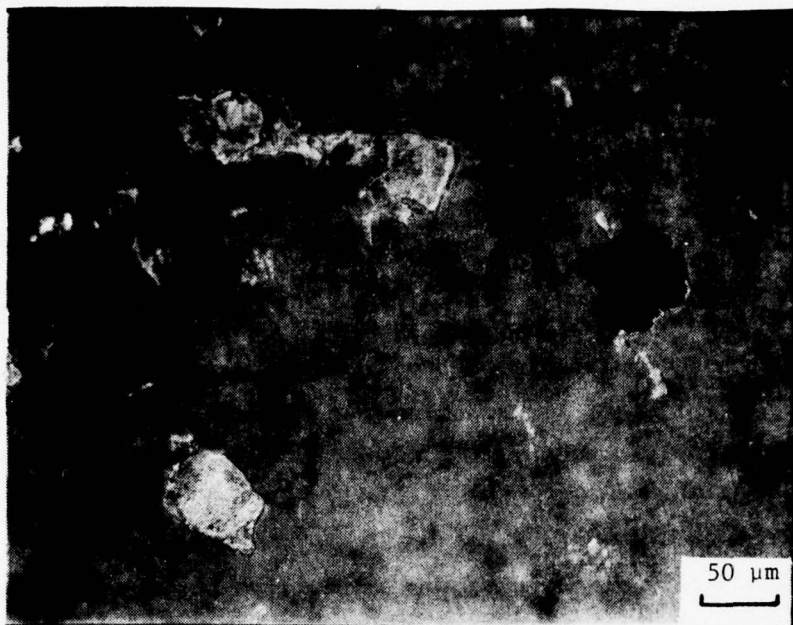


Figure 23. (001) CaF_2 after exposure to a rainfield of 1.8 mm water drops for 1000 impacts/cm² at 222 m/s



Figure 24. Scanning electron micrograph of (001) CaF_2 showing erosive attack at site of grinding damage after dislocation etching.

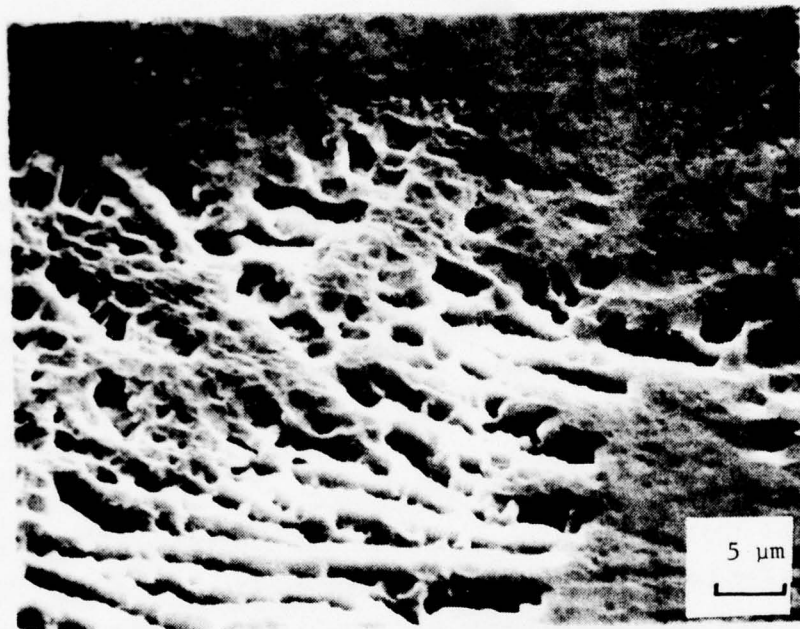


Figure 25. Scanning electron micrograph of (001) CaF_2 showing etch pit detail at site in Figure 24.

impact well below the conditions required for fracture during a single impact.

Examination of cross-sectioned specimens indicated that penetration of erosion damage into the specimen interior could not be detected consistent with the low level of surface damage. Vickers microhardness measurements using a 200g load indicated a microhardness of 177 ± 3 kg/mm which is sufficiently similar to the as-polished microhardness of 171 ± 3 kg/mm to further suggest that the specimen's surface did not undergo degradation (beyond sparse formation of fissures). Although some fissures occurred along scratches and crystallographic orientations, the majority were randomly oriented. Water drop impact conditions above the subthreshold level for damage described here will be investigated.

3.1.2 Nylon Bead Impacts

Several (001) oriented specimens of calcium fluoride were impacted with 1 mm nylon beads in the velocity range of 675 to 885 ms⁻¹. Under these conditions the impacts produced square fracture patterns analogous to Hertzian ring fractures for glass with the fractures aligned along the traces of the {111} cleavage planes. These fractures tended to be short and discontinuous, frequently lying along tangentially aligned scratches. The interior of the region bounded by these square fractures appeared to be undamaged. The fractures beyond the square fracture arrays nearest the impact site were larger, were more closely aligned along the {111} orientations, and penetrated deeper. A large crystallographic truncated pyramid formed beneath the impact site which penetrated into the interior in a manner similar to the Hertzian fracture cones in glass. These characteristics are illustrated for typical impacts in Figures 26 to 30.

The interior dimensions of the square fracture patterns generally ranged from .125 to .30 mm and the outer limit of the ring diameter from 1 to 2 mm. Examination of the rings under polarized light revealed a

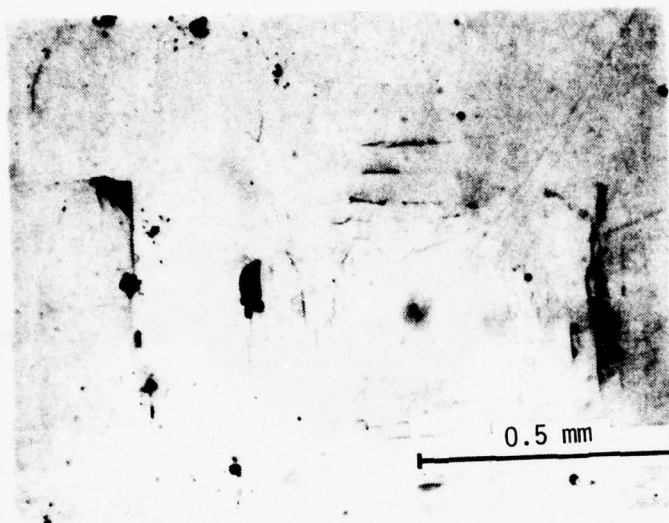


Figure 26. 1 mm nylon bead impact on (001) CaF_2 at 675 m/s

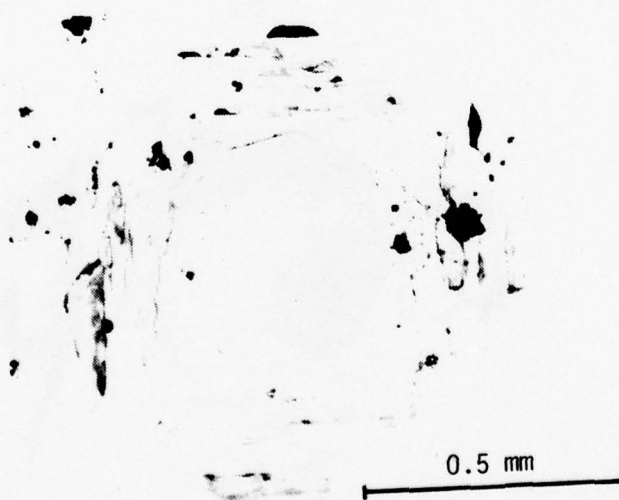


Figure 27. 1 mm nylon bead impact on (001) CaF_2 at 760 m/s

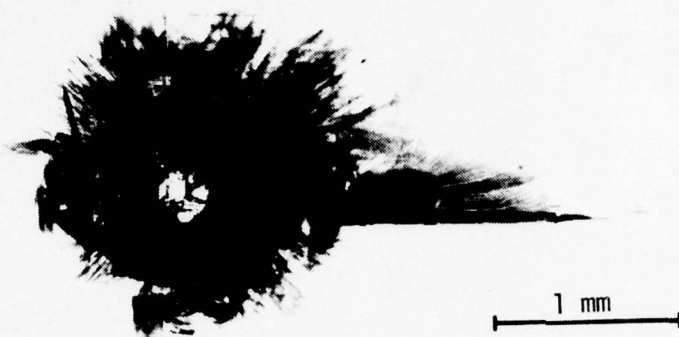


Figure 28. 1 mm nylon bead impact on (001) CaF_2 at 885 m/s.



Figure 29. Detail of (001) CaF_2 impacted with a 1 mm nylon bead at 835 m/s.

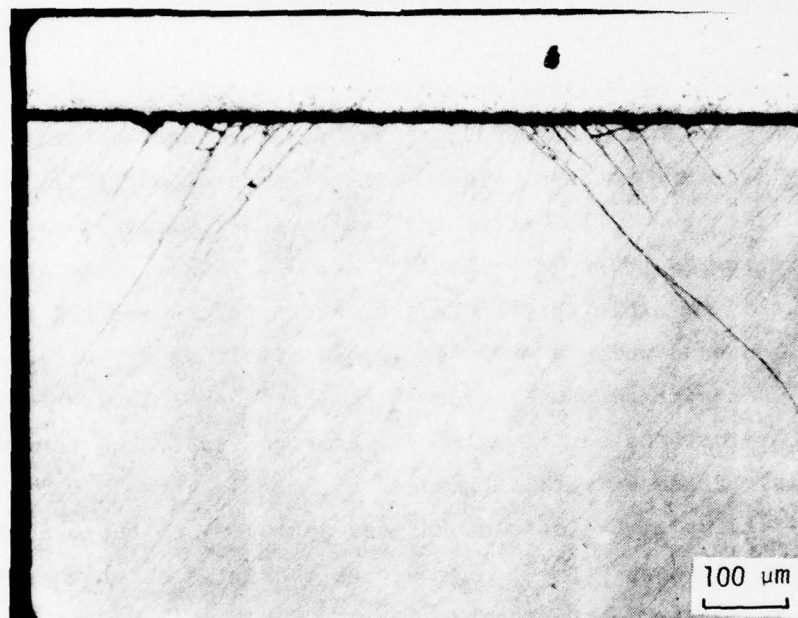


Figure 30. Lightly etched cross section of (001) CaF_2 impacted with a 1mm nylon bead at 760 m/s.

diffuse strain field surrounding the interior fracture pyramid with the greatest intensity along the $\langle 100 \rangle$ axes. The birefringent illumination was less intense than that associated with the more localized Vickers microhardness and 1 mm sapphire bead indentations (Section 3.1.4). The interior appeared to be free of birefringent effects.

Application of a light etchant sensitive only to sealed fracture paths revealed a more dense and circular fracture pattern existed within the square fracture pattern. These fractures were particularly evident along the $\langle 100 \rangle$ axes. The etchant revealed small microcleavages on the central surface as shown in Figures 31 and 32. Since these form an annulus, it is possible they arose from shear forces exerted by the deforming nylon bead which are of negligible magnitude for water drop impacts.⁽⁸⁾ Application of a hydrochloric acid procedure which heavily over-etched fractures but revealed dislocations indicated the circumferential fractures were surrounded by a dense array of pits. These pits appear to originate at dislocations analogous to those observed on rain erosion surfaces. These pits probably originated at emerging dislocations associated with fracture formation although a contribution from a frictional shearing action can't be ruled out.

The fracture pyramid is best illuminated by its own strain field as shown in Figure 33 for a partially crossed polarizer setting. Examination of the lightly etched specimen with a condensor stage at magnifications up to 300X and various working distances revealed the pyramid originated near the innermost limit of the fracture rings. However, both the fractographic river markings and the absence of etched surface fractures at the projected point of intersection suggest many of these fractures originated 5 to 15 μm below the surface.

Under lower magnifications, the ring appeared to be a coherent structure which could be traced continuously in any direction. The internal pyramidal surface was very rough in comparison with that produced

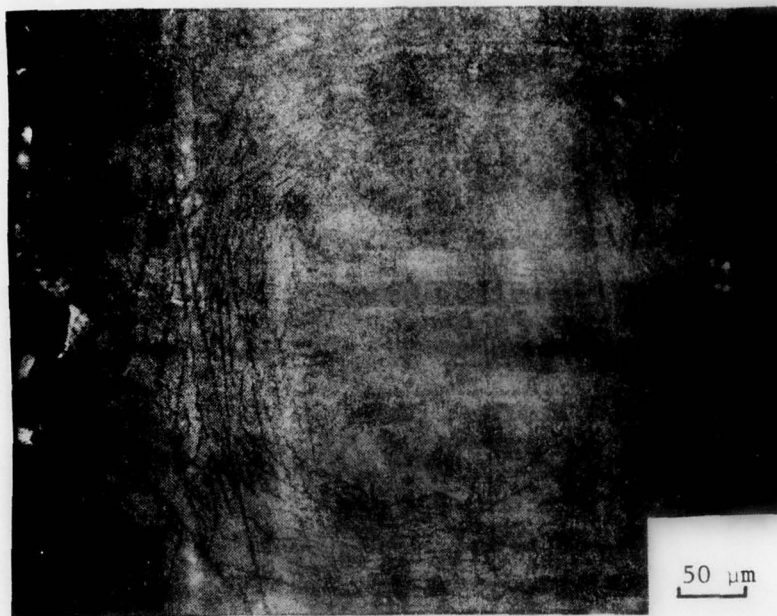


Figure 31. Lightly etched surface of (001) CaF_2 impacted with a 1mm nylon bead at 760 m/s.

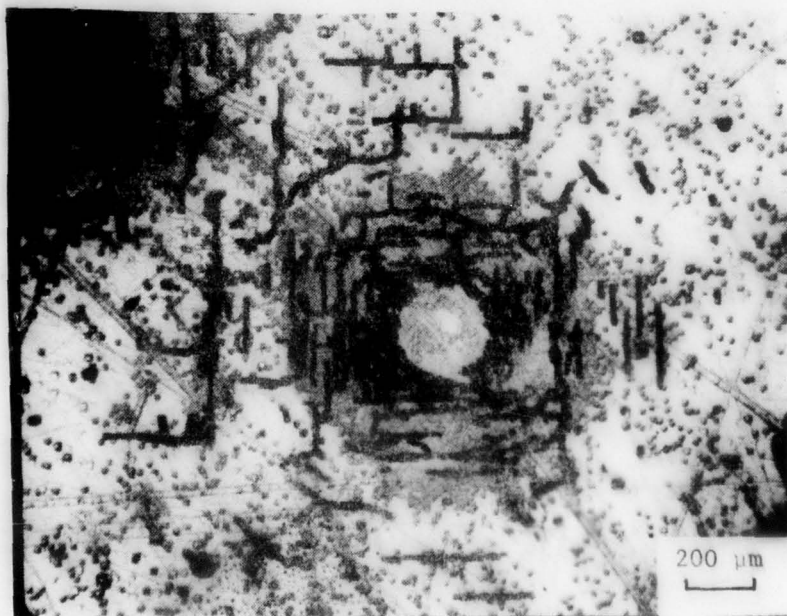


Figure 32. Surface of (001) CaF_2 impacted with a 1mm nylon bead at 675 m/s after dislocation etching.



Figure 33. Fracture pyramid in (001) CaF₂ due to impact with a 1mm nylon bead at 760 m/s shown in birefringent illumination.

by glass indentation with sapphire beads and also the fracture of calcium fluoride under flexural loadings.⁽²²⁾ The large and abrupt misorientations of the fracture facets allow the {100} and {111} cleavage surfaces to accommodate the deviations from the {111} orientations: possibly due in part to the nature of the stress waves generated during pyramid formation. Along the $\langle 110 \rangle$ axes the structure was composed of a system of overlapping fan-like {111} cleavage facets, whereas along the $\langle 100 \rangle$ axes the structure was modified to include (001) cleavage facets to accommodate the corners. This central cone penetrated more deeply than the satellite cleavage fractures.

To investigate the depth profile of the impact damage, cross-sections were prepared by grinding and polishing into several impacts. Although the cross-sectioning was generally successful, two problems could not be resolved. First, there is a possibility that the stresses associated with embedding and also the fine grinding and rough polishing steps could cause near surface fractures to break through to the surface. Second, neither of the reported room temperature dislocation etch procedures nor several compositions explored in this work could form etch pit rosettes about Vickers microhardness indents on as-polished (001) CaF_2 . Consequently, it was necessary to etch with nearly boiling solutions of hydrochloric acid. Although the specimens were slowly cooled, an unknown stress cycle is thereby imposed on the fractured specimens. Measurements of the fracture lengths on both free and embedded specimens indicated fracture length growth generally ranged from unchanged to 10 percent. This is within experimental error and some extension due to dissolution would be anticipated.

The surface of the central regions of the etched and lightly etched sections appeared to be undamaged. The central fracture pyramid penetrated more deeply than the adjacent cleavage fractures. In Figure 30 the pyramid depth is 350 μm whereas the deepest adjacent fracture is

180 μm . The crystallographic angle between the (100) and (111) surfaces is 55° and the following experimental angles can be measured from Figure 30: right- 51° (pyramid boundary), 48° , 58° , 61° , and 60° and left- 44° (pyramid boundary), 41° (split in boundary), 51° , 49° and 57° . The smaller angles are due to a split in the boundary of the cross-sectioned pyramid wall on the left hand side (as seen in Figure 30), however such deviations are not representative of the cone fracture surface. It is difficult to assess the magnitude of the crystallographic influence since similar angles have been recorded for nylon bead impacts on fine grained zinc sulfide.⁽²³⁾ Consequently, the crystallographic cleavage requirements determine the projected geometry of the fracture pyramid but the penetration angle is also sensitive to the transient stress profile. The very limited slip (to depths less than 2 to 3 μm) and the presence of the fracture pyramid would support the application of a Hertzian model as a first approximation to the impact damage for water drops at sufficiently high impact velocities. The significant differences noted in Section 2.2 between the transient and static stress distributions for CaF_2 hinder the suggested approach from being a direct application of the Hertzian analysis suitably modified for anisotropic materials.⁽²⁴⁾

The average cone depths for four impacts were measured with an uncertainty of ± 0.1 mm. A plot of the cone depths as a function of impact velocity provided a straight-line extrapolation which indicated that the threshold velocity for cone formation was approximately 660 ms^{-1} . This extrapolation is consistent with highly asymmetric cone structure at the lowest velocity, 675 ms^{-1} , in which only one side of the pyramid was well-developed and the opposing side was barely visible. At 885 ms^{-1} a radial fracture was produced extending several millimeters into the adjacent material (Figure 28). The velocity range over which pyramidal fracture surfaces occur has a lower bound of 660 ms^{-1} and an upper bound in the vicinity of 885 ms^{-1} .

3.1.3 Sapphire Bead Impacts

Both (001) and (111) surfaces of calcium fluoride have been impacted with 1 mm sapphire beads^{*}. At the lower velocities the impact events produced a ring fracture surrounding the impact, shallow crushing beneath the impact site, and short radial fractures whose traces corresponded to the (111) direction. The ring fractures for the (111) impacts agreed more closely with the anticipated crystallographic geometry of a hexagon than the impacts on (100) calcium fluoride and on (111) silicon (Section 3.2.3) as shown in Figure 34. The central crushing appears to be a general characteristic of the sapphire bead impacts for the materials examined to date; although less crystallographic in nature it is believed similar to that observed for the cross-sectioned magnesium oxide (Section 3.3.3).

At the low impact velocities, the impact produced only a slight concavity within the ring in contrast to the deep impressions under quasistatic conditions. Etching techniques reveal that the lower velocity impacts for both orientations are surrounded by a field of dislocations. These dislocations conform to the anticipated geometry as shown in Figure 34. Comparison of the birefringent patterns for the impact and indentation geometries show the impact pattern is less intense and less closely aligned to the crystallographic axes; slip bands could not be discerned by this technique in the vicinity of the impact site. This indicates a more diffuse but less coherent plastic deformation surrounds the impact sites in comparison with the indentation sites. Plastic deformation is not confined to the immediate vicinity of fractures as in the case of nylon bead impacts and the preliminary observations of water drop impacts. Slip bands could be readily dis-

^{*}The initial pressure-velocity calibration for the air gun was found to be in error after completion of most of the sapphire bead impact studies, so precise velocities can not be stated for the damage modes described in this report. Although the experimental arrangement is quite satisfactory, the impact velocities were found to be inherently random; so only rough estimates of the impact velocities can be made at this time.

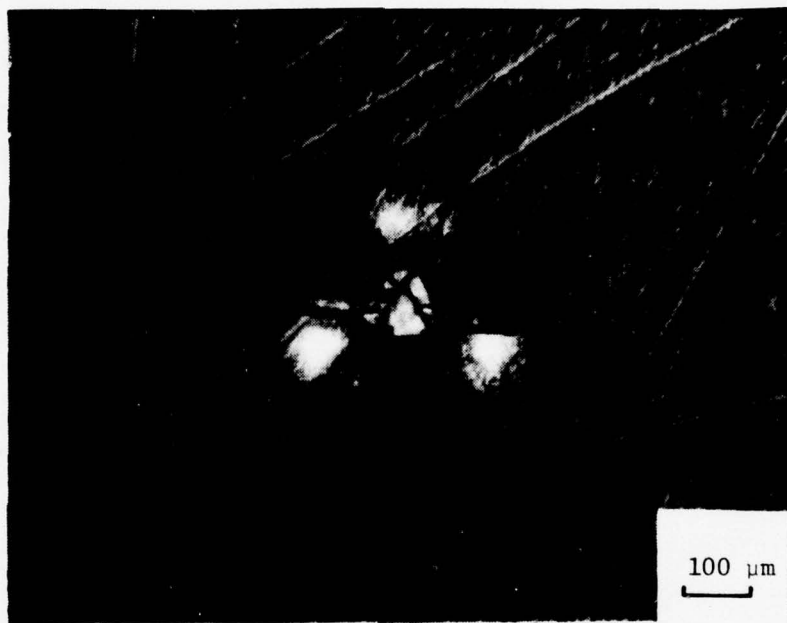


Figure 34. 1 mm sapphire bead impact on (111) CaF₂ after dislocation etching.

tinguished in the micrographs of the bead impacts on the (111) orientation but not for the bead impacts on the (001) orientation.

Further increases in the impact velocity produced fractures and cavity patterns similar to those observed for rigid bead impacts on the other materials investigated here. Initially radial fracture extension occurred along the traces of the {111} cleavage planes. Tsai and Kolsky⁽²⁵⁾ had previously noted for ball bearings impacting glass surfaces that the radial fractures were highly symmetric with fractures forming at 180° apart when two radial fractures are formed and 120° apart when three radial fractures appear. A similar observation was noted for the (111) oriented CaF_2 ; three wavy fractures radiated 120° apart on the surface of the specimen in directions rotated 30° from the crystallographic axes. All fracture patterns showed a striking symmetry in fracture length. The extent to which radial fracture extension in this material can be related to the impact parameters is currently under investigation.

Increases in impact velocity produced crater formation as described by Evans for fine-grained polycrystalline materials⁽²³⁾. The intermediate stage is shown in Figure 35 in which one lateral segment has been ejected and crushed material beneath the impact axis is revealed at the edge of the crater. The lateral fracture markings suggest the fractures originated beneath the crushed zone and were bounded by previously formed radial fracture. This is clearly a relief phase phenomena. Further increases in velocity would produce craters as described in Section 3.2.3. Fractures within the impact rings of the (111) CaF_2 were more obviously crystallographic. Under transmission illumination, equilateral triangles and hexagonal figures were seen at various depths. The intersection points of these internal fractures appeared to initiate the longer radial fractures. Only at the higher



Figure 35. 1 mm sapphire bead impact on (001) CaF_2 showing first stage of material removal.

velocities could fractures displaying the median vent structure be distinguished. These penny-shaped fractures passed beneath the indentation site and extended to form long radial fractures along the {111} cleavage planes. As the impact velocity was increased further these propagated through the central contact zone just below the surface crushing zone. Further increases in velocity produce crater structures and lateral cavities determined by these radial fractures.

3.1.4 Quasistatic Bead Indentations

A specimen of (001) oriented CaF_2 was indented with 1 mm sapphire and tungsten carbide beads. The indentations generally produced shallow hemispherical cavities with lateral dimensions ranging from .12 to .25 μm , the smaller dimension characterized indents at the fracture threshold of 3.6 kg and the larger dimension characterized the transition to macroscopic fracture propagation. At the larger loadings the circular symmetry was transformed to yield a rounded square aligned along the $\langle 110 \rangle$ axes consistent with the {100} $\langle 110 \rangle$ slip system active in the fluorspar structure.^(26,27) Octagonal shapes were also observed at higher pressures.

Initial fracture formation consisted of a radial fracture of nearly vertical, half-penny geometry which appeared to originate from the cavity wall beneath the surface. This radial fracture propagation was confined to the $\langle 100 \rangle$ and $\langle 110 \rangle$ axes, although it was surprising that the $\langle 110 \rangle$ fractures did not form smaller angles with respect to the surface since the {111} - {100} intersection angle is 55° . The zone of plastic deformation for all indents extended well beyond the fracture perimeter as determined by transmission microscopy under polarized illumination. Unfortunately, the specimens were embedded for cross-sectioning before suitable etching techniques to reveal etch pits were established for the (001) orientation. The birefringence formed intense bands closely aligned to the $\langle 100 \rangle$ axes and well-defined {100} slip bands

could be distinguished in the original photographs at least 30 μm from the actual impression. Analogous birefringence effects were observed about the Vickers microhardness indentations. Applications of the fracture etchant to the indented surface also suggests these vertical fractures generally originated below the surface and propagated outward and upward. The second fractures to form were penny-shaped, internal satellites which originated from both the impression wall and the vertical fracture. Careful examination revealed no evidence of median vent formation but such fractures could have formed and essentially resealed during the indentation cycle.

Application of greater pressure to the indenter produced larger and more complex fractures as shown in Figure 36. Although no sign of crushing occurred, a complex pattern of radial and internal penny-shaped fractures formed (Figure 37). Gradually, the $\langle 110 \rangle$ fracture orientation predominated over the $\langle 100 \rangle$ fracture orientation (the $\{100\}$ plane are secondary cleavage orientations in the fluorspar system). For the largest indents, one or two very large half-penny shaped cracks would form along the $\langle 110 \rangle$ axes suggesting that a median vent had extended radially from beneath the indenter to form a radial fracture during unloading. Although the CaF_2 was transparent, the complexity of the fracture structure frequently obscured the fractographic details. However, the median vents were observed to form predominantly along the $\langle 110 \rangle$ direction. These fractures tended to be inclined to the surface suggesting a compromise between the $\{111\}$ orientation and the radial stress and plasticity effects. The largest applied loads produced macroscopic radial fractures which dominated the fracture system.

3.2 SILICON

Specimens of (001) oriented Si have been subjected to multiple water drop impacts and higher velocity nylon bead impacts. Lower velocity sapphire bead impacts were examined on (111) oriented Si. Crystallo-



Figure 36. 1 mm sapphire bead indentations on CaF_2 .



Figure 37. 1 mm sapphire bead indentation on CaF_2 showing penny-shaped fracture propagation on $\{111\}$ plane.

graphic fracture initiation is common to all test conditions, however additional damage modes are found in the rain eroded specimens.

3.2.1 Multiple Water Drop Impacts

The impact conditions employed in the multiple water drop field were well below the threshold for single drop fracture. The exposed specimen surface was chemically polished. Exposure of the silicon specimens resulted in the gradual development of minute pits and hair-line fractures together with a few large cavities. The individual erosion structures resembled those observed previously on germanium and oxide-based glasses at the same and lower velocities.^(19,21)

Exposure of a silicon specimen to a density of 15 water drop impacts/cm² at 257 ms⁻¹ did not produce discernable damage, comparison of the eroded surface with a replica of the as-received surface revealed a few isolated polishing digs; these were not enlarged during the brief exposure. Neither transmission electron microscopy of replicas nor Nomarski interference contrast provided evidence for small cleavage fractures. Continued exposure of this surface to a water drop density of 1000 impacts/cm² gradually introduced an isolated array of incipient damage. This damage resembled some of the structures on Ge after exposure to low impact densities at 222 ms⁻¹⁽²¹⁾. Fractures in Si generally were propagated over much shorter distances, the damage dimensions were less uniformly distributed, and the damage density was much lower. This increased resistance of Si is attributed to its greater fracture strength and higher quasi-longitudinal wave speed which reduces the duration the tensile stresses are at their maximum values than for Ge (compare Figures 16 and 17, 20 and 21). The increased dispersion in damage dimension is attributed to the decreased ratio of impact stress to fracture strength which confined erosion to the largest surface flaws and the large flaw dispersions associated with well-polished surface. An analogous trend toward more uniform damage has been observed for a series

of borosilicate glass specimens subjected to high impact densities as the impact velocity varied from 132 to 222 ms⁻¹(19)

Water drop induced fractures propagated in (001) Si via cleavage along {111} planes and along conchoidal paths with no evidence of secondary cleavage orientations. This fracture response is consistent with water drop impacts on Ge and existing indentation and particulate impact fractures reported on both Ge and Si. Cleavage fractures on the eroded silicon surface were initiated both in the absence and in association with small pits and cavities. At this stage for incipient damage, the mechanistic sequence by which the small pits were formed was not evident.

The fine cleavage fractures did appear to be preferentially nucleated from the larger incipient cavity structures as shown in Figure 38. This figure also reveals several isolated fractures, although these may not be as readily observed on copies of the original micrograph. In several instances, the hairline fractures extended up to 1 mm in length with forks and associated cavities similar to the fracture structures observed on the rain erosion of soda lime glass.⁽¹⁹⁾ These cleavage fractures weakened the surface by introducing large flaws with sharp tips and provided preferential paths for cavity extension. Examination of the as-polished surface (including etching) provided no evidence that significant sized cleavage fractures existed before etching. Cleavage fractures also formed as compact fracture arrays suggesting the onset of crushing within the material below the surface. Insufficient erosion damage had taken place to evaluate whether such sites could nucleate erosion pits.

Although the most severe cavities originated at the sites of residual polishing digs, nearly all cavities had lateral dimensions less than 100 μ m. Incipient cavities which apparently initiated at sites free of surface preparation damage are shown in Figures 38 and 39.



Figure 38. Scanning electron micrograph of (001) Si exposed to rainfield of 1.3 mm water drops for 1000 impacts/cm² at 257 m/s showing incipient cleavage formation.



Figure 39. Scanning electron micrograph of (001) Si exposed to rainfield of 1.8 mm water drops for 1000 impacts/cm² at 257 m/s showing initial erosion pit.

The larger cavities tended to grow through the formation of cleavage fracture in the central cavities and by formation of shallow lateral spall cavities and radial fractures. At this stage, localized enlargement of incipient damage was more important than development of a fracture network extending across the surface. Consistent with this, macroscopic views suggested degradation of optical transmittance and mass loss to be minimal. The mechanisms postulated for damage nucleation in oxide-based glasses with sparsely distributed residual polishing digs can account for all the observed cavities.⁽¹⁹⁾

Several large arrays of circular damage were observed and the best defined is shown in Figure 40. These arrays resemble those observed for single drop impact damage on arsenic trisulfide and borosilicate glasses with dimensions comparable with single impact damage observed during rain exposure of lower strength materials.⁽¹⁹⁾ Previous observations on borosilicate glass and zinc sulfide (Irtran-2) strongly suggested that there is an impact regime in which the initial impact fractures can structure subsequent impact damage to produce a disjoint but consistent ring fracture.^(19,28) The fracture arrays on silicon resulted from impact by anomalously large drops because of their low areal density in comparison with the impact density and the absence of extraneous fracture anticipated for a field of grinding damage.

Further suggestion of one higher intensity impact is provided by the surrounding cleavage which forms well-defined, inward oriented ledges as shown in Figure 40. The smaller cracks in the interior have the opposite ledge orientation suggesting they were formed by different drop impacts. The possibility that random larger drop diameters than the stated average diameter can be far more damaging suggests that rotating arm tests may overestimate realistic lifetimes based on a uniform field of drop sizes. A quantitative estimate of the manner in which the drop diameter can influence the response of the target material



Figure 40. (001) Si exposed to rainfield of 1.8mm water drops for 1000 impacts/cm² at 257 m/s using Nomarski interference illumination.

has been described.⁽²⁾ The strong dependence of erosive damage on drop diameter suggests that standard rotating arm tests with well-defined drop sizes should be supplemented with evaluations of the limits of drop diameter and impact velocity over which the results of these tests are meaningful for the stated conditions.

3.2.2 Nylon Bead Impacts

Impacts by 1 mm nylon beads on (001) oriented Si at 915 and 975 ms^{-1} did not yield well-defined fracture structures. The lower velocity impact produced a loose circular array of short, wavy cleavage fractures. Extension of the short circumferential fractures occurred along a tangential rather than a radial orientation into the surrounding material. The overall fracture structure and the tendency for tangential propagation from the perimeter resembled the more coherent structures produced by indentation with 1 mm diameter tungsten carbide spheres. The ring diameter for the nylon bead impact is .25 mm whereas those produced by a tungsten carbide indenter ranged from .2 mm to .3 mm.

In contrast, the higher velocity nylon bead impact was far more destructive than lower velocity water drop impacts. In addition to forming a similar small ring, larger nonconcentric square arrays are also formed as shown in Figure 41. Some evidence of cavity formation by lateral outflow can be found in the outer fracture pattern. It is interesting to contrast this impact with the 885 ms^{-1} impact on a (001) CaF_2 surface which produced a long radial fracture and associated large penny-shaped crack. The transient stress distribution appears to be highly dependent upon the degree of microplasticity within the crystal under dynamic loading conditions.

Nylon bead impacts on (111) Ge at 730 ms^{-1} produced a large set of concentric ring fractures. The central diameter of .25 mm agreed



a. Nylon distribution
around impact site



b. Fracture produced
by nylon bead im-
pact

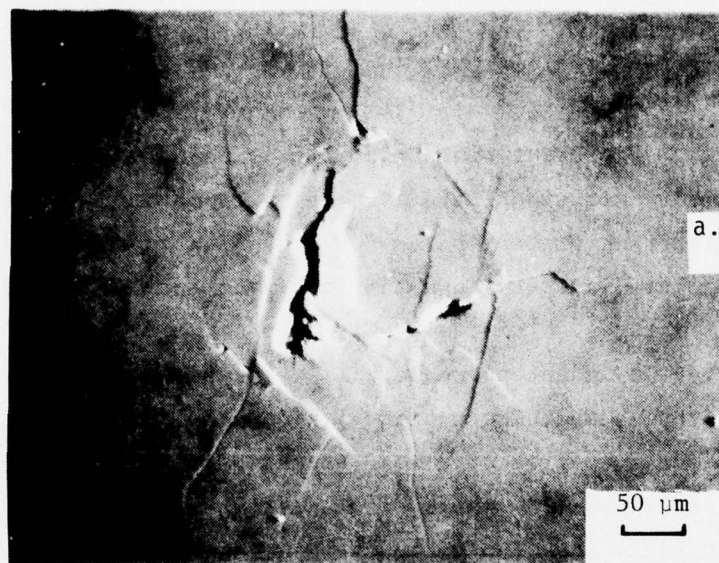
1 mm

Figure 41. 1 mm nylon bead impact on (001) Si at 975 m/s.

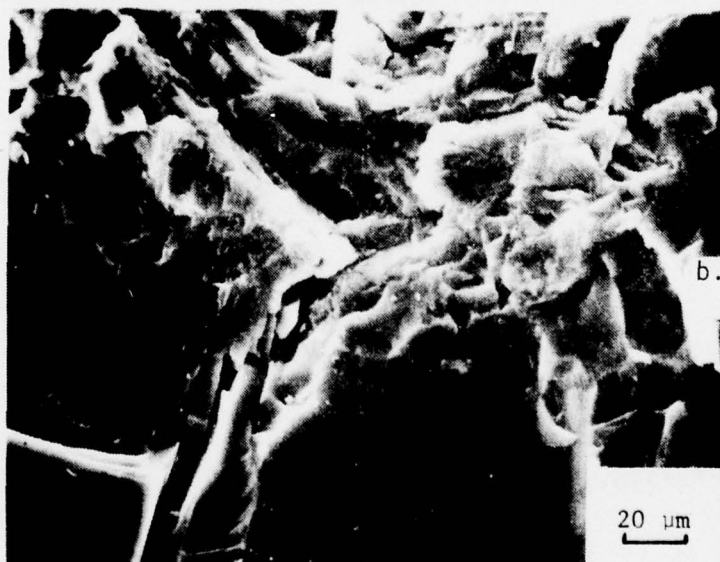
closely with that observed on silicon. However, the germanium fractures extended beyond a diameter of 3 mm with the fracture lengths increasing with increasing radial distance.

3.2.3 Sapphire Bead Impacts

A somewhat different ring fracture was observed on (111) oriented Si specimens for collisions with 1 mm sapphire beads. At low velocities loose irregular ring fractures formed which span approximately .12 to .18 mm: a smaller diameter range than observed for quasistatic indentation ring fractures. This damage is also far more complex as shown in Figure 42. The indentations initially formed a coherent ring of cleavage fractures enclosing a central zone free from damage. The central zone remained free of damage as larger loads produced nearly coherent multiple rings from which cleavage fractures extended predominantly tangentially into the surrounding material. Spalling occurred primarily at the larger exterior lateral fracture bounded by these tangential and smaller radial fractures. In contrast, the impact produced a central depression and fracture .06 to .08 mm in diameter, noncoherent rings of damage and irregular fractures, frequent spalling along the ring perimeter, and numerous irregular radial fractures which propagated into the surrounding material. The larger central spalls reveal a broken, fragmented subsurface suggesting complex crushing in the central region. Increasing the impact velocity of the sapphire beads produced structures containing a large jagged central crater, crystallographic and irregular radial fractures, and lateral vent cavities. The central interior of the craters frequently contained trigonal and hexagonal shapes suggesting crystallographic median vents had formed.



a. Overview of damage site



b. Detail of large crack

Figure 42. Scanning electron micrographs of (111) Si impacted with a 1mm sapphire bead.

3.3 MAGNESIUM OXIDE

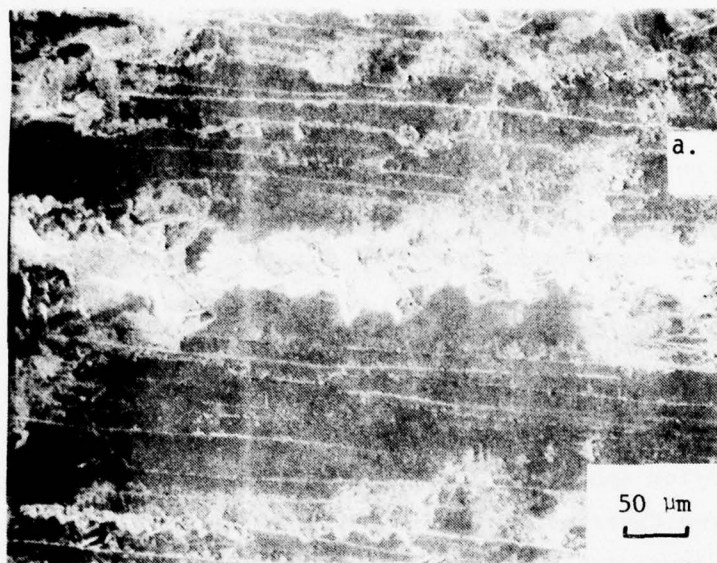
Single crystal specimens of MgO in the (001) orientation have been subjected to the following impact loadings: multiple water drop impacts on the rotating arm, higher velocity nylon bead impacts, lower velocity sapphire bead impacts, and quasistatic indentations. The impact conditions employed in the multiple water drop impact tests were well below the threshold for single impact fracture. Exposure of as-cleaved surfaces resulted in gradual propagation of residual cleavage damage and the introduction of networks of dislocation loops within the surface layer. Similar dislocation networks have been reported for exposure of lithium fluoride to methanol drop impacts⁽²⁹⁾. Exposure of the MgO to nylon bead impacts at supersonic velocities yielded extensive slip band formation within the underlying surface layer and a subsurface radial fracture system. The sapphire bead impact velocities spanned a range from the introduction of slip band rosettes without associated fracture to the development of bulk cleavage. A series of quasistatic sapphire bead indents were also carried out for comparison with the dynamic loading conditions.

3.3.1 Multiple Water Drop Impacts

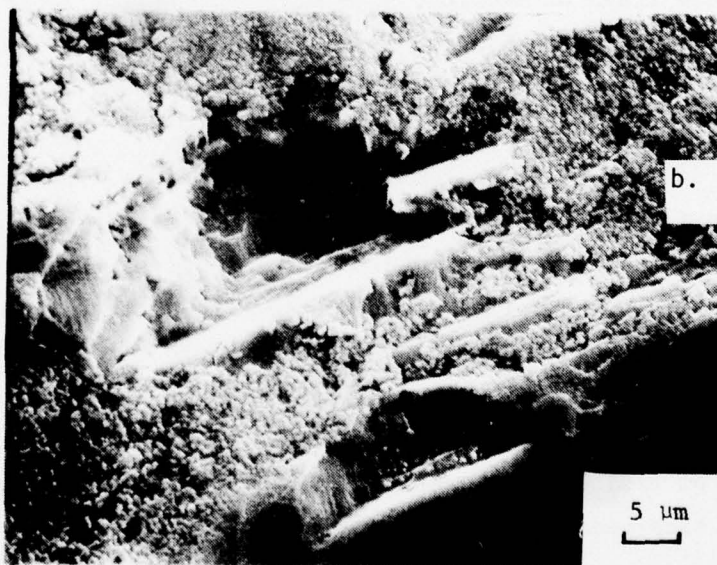
As-cleaved MgO specimens were exposed to the standard rainfield in the AFML rotating arm erosion facility at 258 ms^{-1} for 6 sec (15 impacts/cm²) and for 10 minutes (1000 impacts/cm²). The as-cleaved surfaces were relatively free of large ledges and other forms of gross damage due to cleaving. The principal observation from the 6 sec exposure was the ejection of minute flakes of undercut surface. Application of a dislocation etch to this surface revealed a shallow pattern of microfissures and residual cleavage damage.

Continued exposure of the sample to the rainfield produced gradual erosion as shown in Figure 43 for a 10 minute exposure at 257 ms^{-1} . Damage primarily consisted of cavity growth (particularly along cleavage ledges) and fracture extension. The relatively short $4 \mu\text{m}$ extension contained in Figure 43b is typical. A granular deposit which covered a large portion of the sample appears to be a reaction product such as a carbonate or a hydrated oxide formed during the rainfield exposure. Such formation is probably assisted by the removal of a surface film since it did not form on the unexposed sides of the specimen or on the 6 sec exposure surface. Although Figure 43b was chosen to show both the granular deposit and the crater growth, the granular patches were randomly distributed rather than selectively connected with the cleavage craters and ledges. Examination under optical microscopy did not reveal any underlying networks of fractures or slip bands associated with the granular deposit. Although a small decrease in optical transmittance was observed for the layer formation, the erosion rate was too slow to detect an anticipated acceleration of erosion. It is doubtful that the layer could afford a protective quality, since adhesion of the micron sized modules would be less than the cohesion of the substrate and their projection would expose them to additional stresses, particularly during lateral outflow.

Exposure of the chemically polished specimen to the standard rainfield for 6 sec at 257 ms^{-1} revealed no evidence of erosion damage. Even after etching damage due to a single impact could not be located due in part to dislocations introduced during testing, particularly in turning the specimen over to expose the opposite face. After the 10 minute exposure the chemically polished surface was free of mechanical damage, although a similar granular deposit as described above covered part of the surface. The granular deposit tended to run in the thin strips along the sample which were not influenced by topological features such as polishing pits, polishing hillocks, and polished contours of cleavage ledges. These



a. Overview of eroded surface



b. Detail of cleavage ledges

Figure 43. (001) MgO (as cleaved) exposed to rainfield of 1.8 mm water drops for 1000 impacts/cm² at 257 m/s.

latter features also resisted selective attack during the rainfield exposure.

Application of a dislocation etchant removed the granular deposit without evidence of substrate damage, topographic displacement, or straining as could be detected with optical microscopy: fracture extension was minimal with the exception of large crystallographic craters associated with incompletely polished damage. Instead, mechanical damage was limited to the extension of $\{110\}_{45}$ slip bands to form overlapping networks and the formation of minute $\{110\}_{90}$ rosettes. A similar predominance of $\{110\}_{45}$ slip band formation over $\{110\}_{90}$ slip band formation has been observed for low load indentations on LiF crystals by nylon spheres⁽²⁴⁾. This observation was attributed to the Hertzian stress distribution which predicts that the subsurface shear stresses are appreciably greater in the $\{110\}_{45}$ plane than the $\{110\}_{90}$ plane. At this stage of erosion, some minute rosettes containing $\{110\}_{90}$ slip planes were observed as shown in Figure 44. These rosettes are similar to those observed by Narayan who impacted a magnesium oxide surface with glass beads ranging from .3 to .27 μm ⁽³⁰⁾. One can speculate that the low density of these rosettes resulted from minute particulate contamination in the rotating arm facility. The minute pits associated with these rosettes may contribute nucleation sites for subsequent cavity growth. However, it is doubtful these rosettes significantly influenced the overall erosion rate since much greater embrittlement would be associated with the large $\{110\}_{45}$ slip bands. Examination of the dislocation profile by etching cleaved cross sections indicated that a dense band of dislocations was present 5-10 μm beneath the surface and that few slip bands penetrated deeper than 50 μm .

To elucidate the depth profile, 26 μm was removed by a chemical polishing cycle. This cycle removed many of the small rosettes and a large fraction of etch pits. Most of the remaining pits were associ-

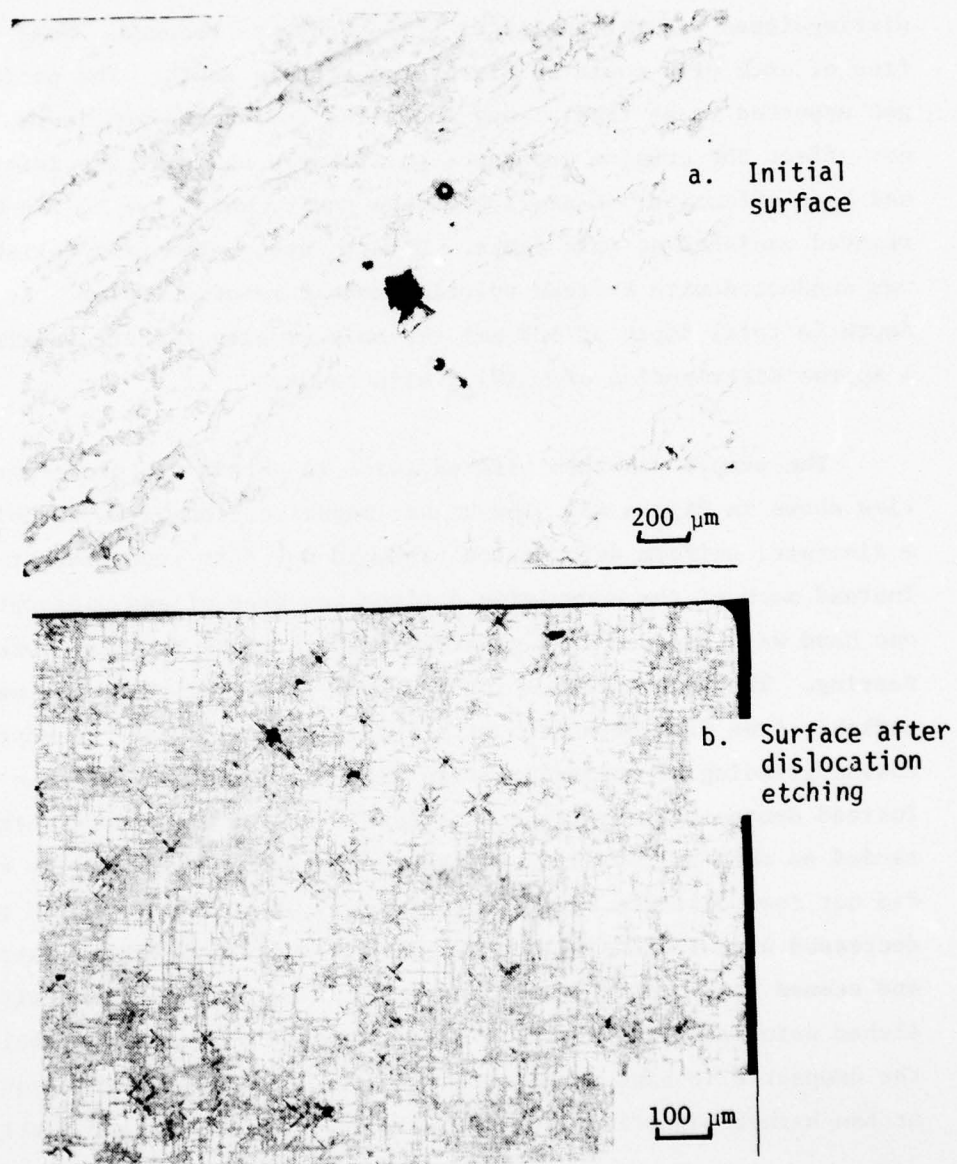


Figure 44. (001) MgO (chempolished) exposed to 1.8 mm water drops for 1000 impacts/cm² at 257 m/s.

ated with the $\{110\}_{45}$ slip bands. The next polishing cycle removed an additional 12 μm . At this depth very few minute rosettes could be distinguished and the number of slip bands was reduced. Some regions free of etch pits could be discovered at this depth. The polished ledges appeared to be free of any anomalies indicating gentle contours did not affect the erosion process significantly and that the initial polish had been effective. A small cleavage cavity which the polish had not removed vanished at this depth. Unfortunately, the next polish cycle was conducted with a fresh solution and it removed 100 μm . At this depth (a total depth of 138 μm) the only erosion feature remaining was a sparse distribution of $\{110\}_{45}$ slip bands.

The sample was then cleaved twice to obtain the cross-sectional view shown in Figure 45. The higher magnification views revealed that a discrete, uniform deformation band did not form underneath the surface. Instead much of the underlying surface was free of any dislocation bands; one band was observed on a cleavage surface which was attributed to tearing. The back surfaces for the two successful cleavages were remarkably free from both etch pits and cleavage ledges. In contrast, coarse grinding of magnesium oxide does produce dense layers of damage⁽³¹⁾. Instead damage principally consisted of $\{110\}_{45}$ slip bands which extended as deep as 300 μm in these two cleavage sections. The slip bands did not form discrete layers but instead a distribution which rapidly decreased with increasing depth. Damage was nonuniformly distributed and seemed to be concentrated in certain regions consistent with densely etched patches in Figure 45. These areas are apparently associated with the deepest slip band penetration. $\{110\}_{90}$ slip bands were not detected at the higher magnifications probably due to their sparse distribution.

The etched surface resembles somewhat the lithium fluoride surface exposed to 100,000 methanol drop impacts⁽²⁹⁾. Comparison of the

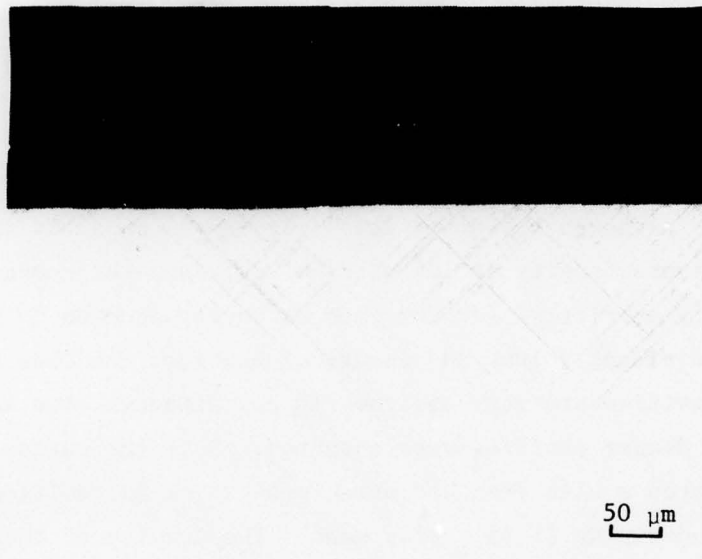


Figure 45. Dislocation etched cross section of (001) MgO (chempolished) exposed to rainfield of 1.8 mm water drops for 1000 impacts/cm² at 257 m/s.

AD-A045 220

EFFECTS TECHNOLOGY INC SANTA BARBARA CALIF
IMPACT DAMAGE IN SINGLE CRYSTALS.(U)
JUL 77 W F ADLER, S V HOOKER
ETI-TR77-49

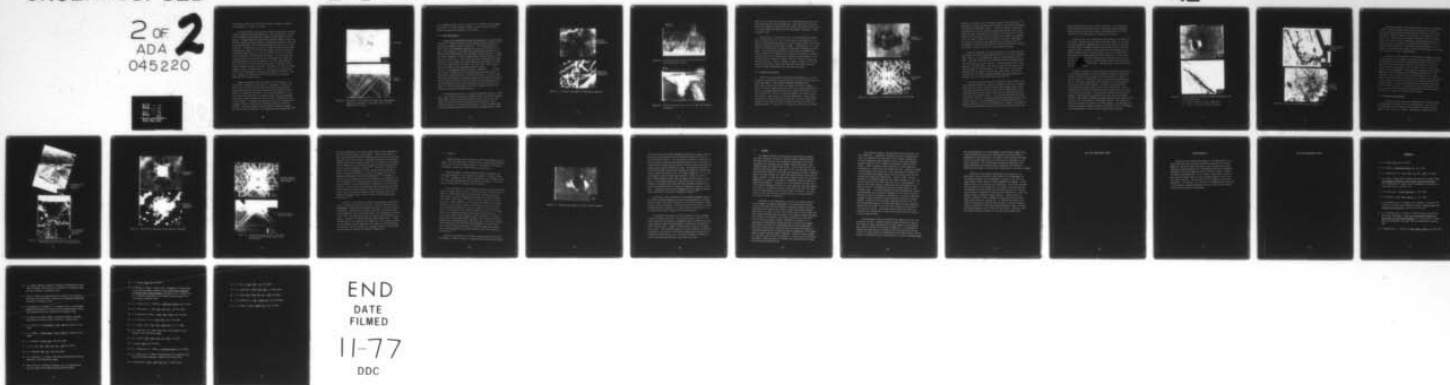
F/G 20/2

UNCLASSIFIED

N00014-76-C-0744
NL

2 OF
ADA
045220

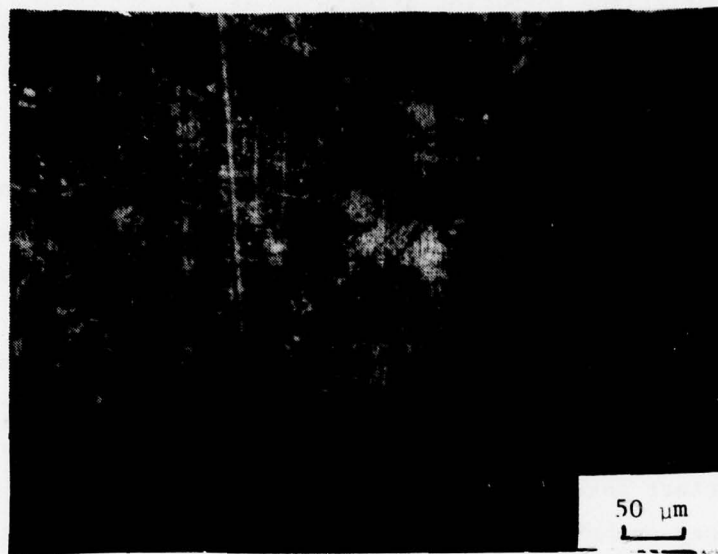
11-77



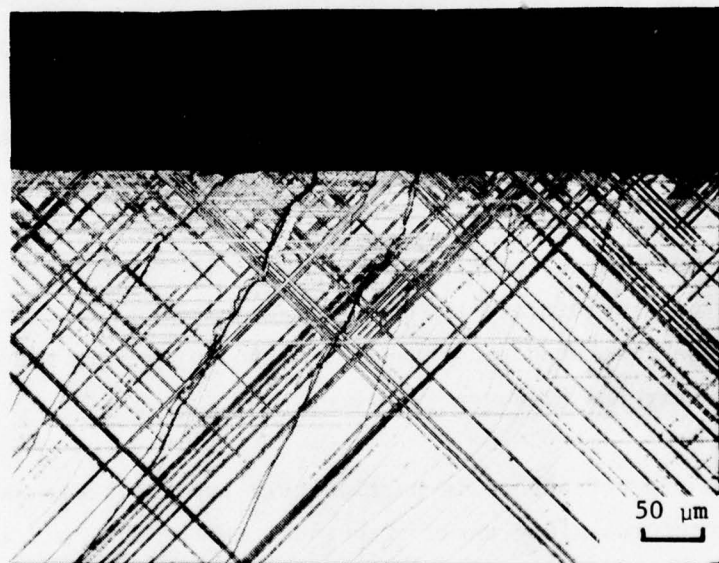
two surfaces reveals that both systems primarily underwent formation and propagation of $\{110\}_{45}$ slip bands.

A second specimen was chemically polished and exposed to the same rainfield conditions for 2500 impacts/cm. This specimen also retained good transmission characteristics although it also formed a granular deposit. Etched surface and cross-section views are shown in Figure 46. Although a greater etch pit density is apparent in the surface view, the most important effect of the increased exposure is the onset of cavity formation. Although these are still very small as shown in Figure 46b the approximate density of 10^3 pits/cm² suggests the surface has been sufficiently embrittled for the rate of cavity erosion to accelerate, both in individual volume and numerical density. At this stage, most of these cavities are very shallow (10 μ m) although some larger and presumably deeper cavities were observed. Note the cavity appears to have initiated a slit fracture which penetrated an additional 10 μ m along an underlying $\{110\}_{45}$ slip band. The density of these slip bands appears to block cleavage fracture. A continuous dislocation layer still has not formed despite the high impact density (2,500/cm²). However, $\{110\}_{90}$ slip bands were not detected despite their apparent appearance on the etched surface.

Damage consequently resulted primarily from increases in slip band density and dimension (extending to 1 mm depths). However, the onset of pit formation indicates that this mechanism would become increasingly important and that measurable optical degradation would result as a significant fraction of the surface was removed. It is clear that the introduction of a worked structure into the magnesium oxide surface impairs rather than aids the erosion resistance in this velocity regime. Although the structure may resist the introduction of cleavage fracture, it assists the formation and growth of shallow cavities. The cavity formation may not impair the window strength; previous work has established it will degrade optical transmittance. (32)



a. Top View



b. Cross Section

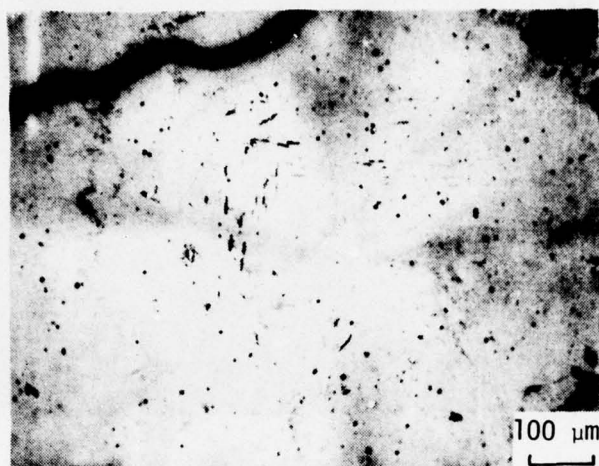
Figure 46. Dislocation etched specimen of (001) MgO (chempolished) exposed to rainfield of 1.8 mm water drops for 2500 impacts/cm² at 257 m/s

It is suggested similar tests be conducted on irradiated or doped magnesium oxide to determine whether a higher yield stress material would resist the embrittling formation of slip bands.

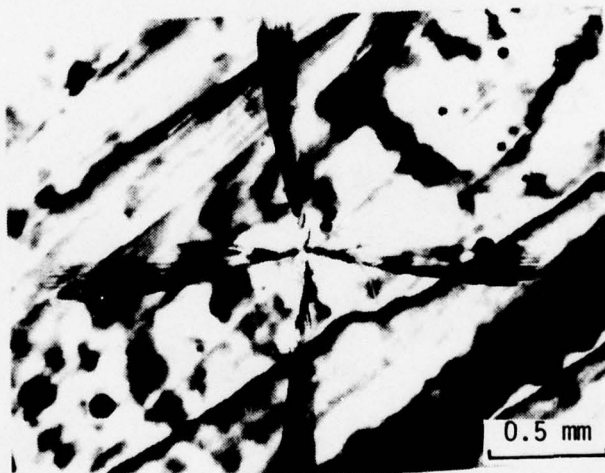
3.3.2 Nylon Bead Impacts

A chemically polished MgO surface was impacted by a 1 mm nylon bead at 1000 ms^{-1} . Optical microscopy of the impacted surface revealed relatively little damage as shown in Figure 47. The surface beneath the nylon contact zone underwent extensive slip along the $\{110\}_{45}$ planes to form a dense network of slip bands which penetrated $130 \mu\text{m}$ beneath the surface before interruption by the subsurface cleavage fracture. (Figure 48) Minute fractures $< 20 \mu\text{m}$ in length formed along one side and corner within the contact zone. Since these fractures occurred near the deposited nylon, they probably were formed along the slip bands by the shear forces associated with the collapse of the nylon bead. Beyond the contact axis, intense slip bands formed along the $\{110\}_{90}$ planes in the vicinity of the subsurface radial fractures. These features are shown more clearly in Figure 49 after cleaving through the impact center and exposing the cleaved surface to a dislocation etchant. It may be speculated that the sequence of responses began with the extensive formation of slip bands beneath the contact zone, that this deformation generated sufficient stress to initiate the sub-surface cleavage, and that propagation of these fractures generated the surrounding slip bands which occurred only near the cleavage fractures.

The subsurface fracture is particularly important because it introduces large fractures along three orthogonal axes. The central cleavage plane shown in Figure 49 passes through the central axis of the subsurface fracture but does not include the entire fracture. The subsurface fracture is inclined approximately 4° to the sectioning face and the remainder extends beneath the matching cleavage surface. Mark-



REFLECTED
ILLUMINATION



TRANSMITTED
ILLUMINATION

Figure 47. 1 mm nylon bead impact on (001) MgO at 1000 m/s.

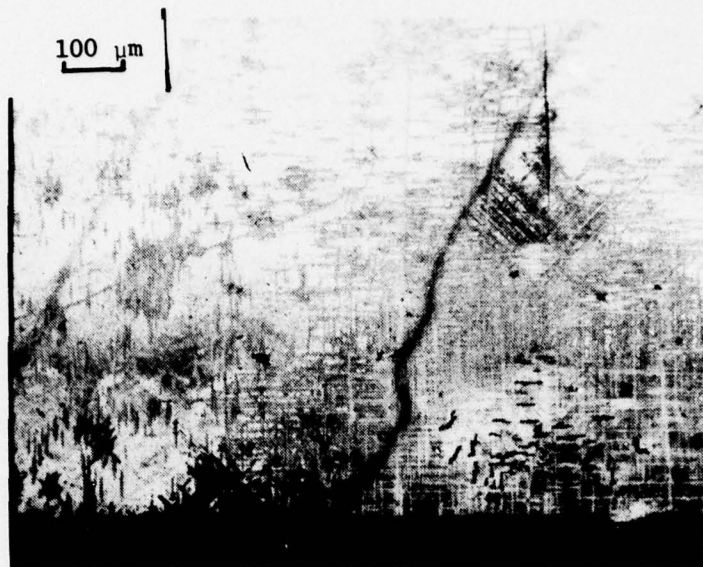


Figure 48. Dislocation etched surface of (001) MgO impacted with a 1mm bead at 1000 m/s.

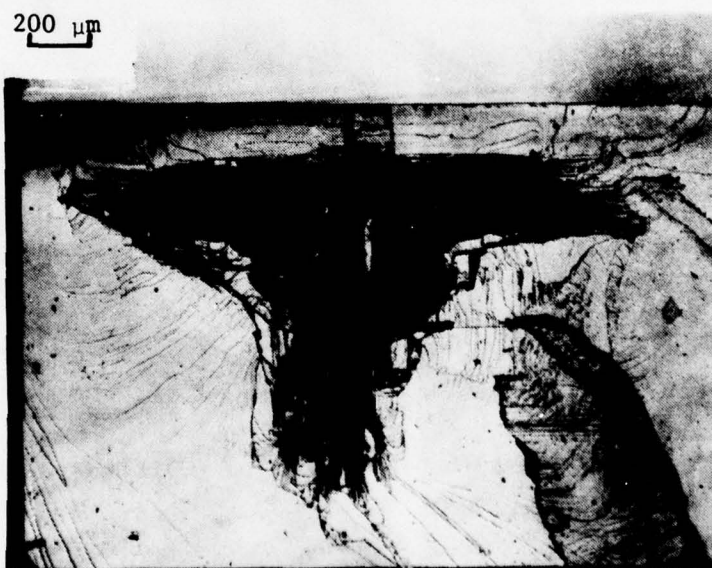


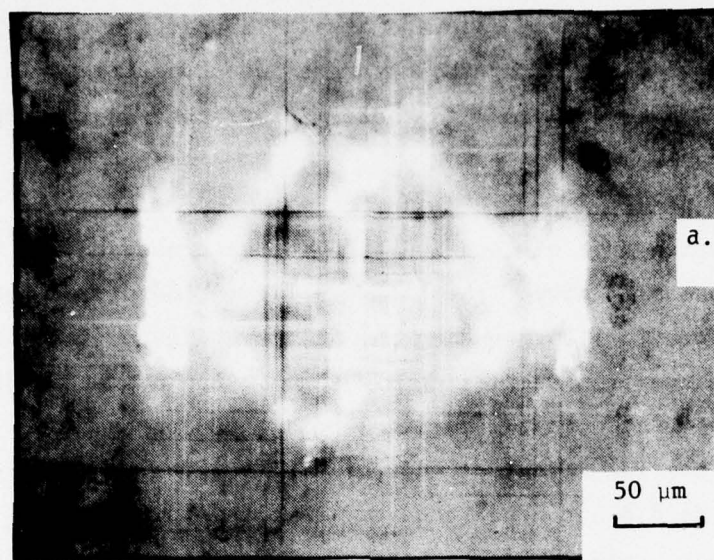
Figure 49. Dislocation etched cross section of (001) MgO specimen in Figure 47.

ings on the fracture system indicate very rapid propagation from a common origin along the three cleavage axes. The portion of the fracture front which formed the penny-shaped arc between these axes is much closer to a plane surface (not shown in these micrographs) indicating a slower propagation rate.

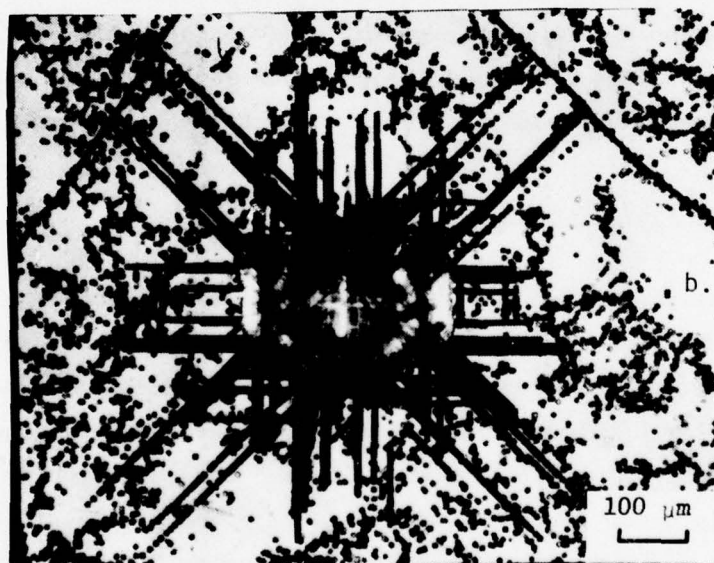
Application of a dislocation etch to the cross-section revealed a zone of intense slip above the cleavage figure, described above, and bands of dislocations surrounding the fracture figure (some of the latter may have resulted from sectioning cleavage). Approximately 25 μm of the surface was removed with the chemical polish and the specimen was etched again. This section revealed bands of dislocations surrounding the fracture figure did not penetrate very deeply into the bulk. Sequential polish and etch cycles indicated the subsurface volume adjacent to the cleavage fracture underwent extensive slip both along the $\{110\}_{90}$ and $\{110\}_{45}$ directions. The etch exposed a number of small slit fractures which initiated along $\{110\}_{45}$ slip bands and several small satellite fractures formed independently near the fracture origin.

3.3.3 Sapphire Bead Impacts

Chemically polished MgO surfaces were also subjected to a series of sapphire bead impacts to provide reference data for the water drop and nylon bead impacts. 1mm diameter beads were propelled over a sufficiently large velocity range to explore the fracture sequence. Below a fracture threshold less than 15 ms^{-1} the collision produced rosettes of slip bands without fracture as reported previously for rock-salt crystals.⁽³³⁾ As for the nylon bead impacts, the contact area is covered with a dense array of slip bands (Figure 50). Larger $\{110\}_{45}$ slip bands are located adjacent to the impact site whose surface components extend along the $\langle 100 \rangle$ directions and outward into the surrounding material. Another set of $\{110\}_{90}$ slip bands also are located



a. Nomarski
Illumination



b. Dislocation
Etched

Figure 50. Low velocity 1mm sapphire bead impact on (001) MgO

adjacent to the impact site and extend along the $\langle 110 \rangle$ directions.⁽³³⁾ Although the $\{110\}_{90}$ slip bands appear longer at the surface, these radiate outward from the impact center. Penetration studies by sequential polishing and etching on cleaved cross-sections show the $\{110\}_{45}$ slip bands are larger and penetrate more deeply at all velocities. Previous workers have also shown that the slip bands are composed of dislocation loops such that the upper surface intersects the screw components of the $\{110\}_{45}$ loops and the edge components of the $\{110\}_{90}$ loops.⁽³⁴⁾ Consequently, the former slip bands form height discontinuities whereas the latter can only be detected by their inherent stresses.

Above the threshold, the initial fracture is a lateral cleavage fracture on the (001) surface approximately 10 to 25 μm below the specimen's surface. It is assumed this fracture forms during the relief phase. At higher velocities, the subsurface fracture propagates downward along $\{110\}_{45}$ fracture surfaces. The deepest penetration occurs along the $\langle 110 \rangle$ directions. New (001) lateral fractures tend to form instead along the $\langle 100 \rangle$ directions. The formation of these initial fractures does not appear to perturb the impact event. It has been observed that the initial fracture formation does not influence the rebound velocity for rigid bead impacts on glass.⁽²⁵⁾

The impact velocities required to initiate surface fracture produce a prominent network of precursor subsurface fractures. Consistent with this, the initial surface fractures adopt several forms: radial $\langle 110 \rangle$ extension outward from the contact area, circumferential $\langle 110 \rangle$ extension adjacent to the contact area, and $\langle 100 \rangle$ extension above the outer edge of a lateral fracture. In all forms, the surface fracture is part of a $\{100\}$ or a $\{110\}_{90}$ fracture which propagated from the subsurface network. It is interesting that the stress gradient in the impact surfaces may be either circumferential or radial. Inspection of the surface with Nomarski interference contrast reveals only the slip

band discontinuities but not a central depression. The transmission view in Figure 50a shows several vertical fractures which propagated toward but did not reach the surface. The well-defined central lateral fracture is characteristic of sapphire bead impacts.

These fractures are confined within the volume of the rosette of slip bands. For the nylon bead impacts onto MgO, nearly all fractures are crystallographic aligning along the $\{110\}$ slip bands or the $\{100\}$ cleavage planes. Although fractures often initiate as slit fractures along slip bands, the large $\{110\}$ fractures tend to propagate in the spaces between prominent slip bands where there is the lowest dislocation density and correspondently the least resistance. As the impact velocity is increased, the circumferential fractures tend to form an ellipse around the impact site with prominent radial extensions along the center $\langle 110 \rangle$ rosette arms. The subsurface systems also increase in size and complexity.

Further increases in velocity beyond the threshold levels produce a well-defined hemispherical cavity underlain by extensive subsurface fracture as shown in the scanning electron micrographs in Figures 51 and 52. Material is displaced to form an upraised rim surrounding the crater. The $\{110\}_{45}$ slip bands which contribute to this displacement are clearly shown in these figures. The widest surface fractures extend radially along the center of the $\langle 110 \rangle$ rosette arms. These fractures result from the displacement stresses and extend to the limit of the $\{110\}_{45}$ slip arrays. Less favorably oriented fractures tend to propagate erratically over much shorter patterns than the principal fracture. The contrast produced by these secondary radial fractures suggests the $\langle 110 \rangle$ rim sides are raised higher than the $\langle 110 \rangle$ corners so that discrete steps are formed at fracture openings. The difficulty for fracture propagation through prominent slip bands is clearly illustrated by the displacement of some of the principal radial fractures.

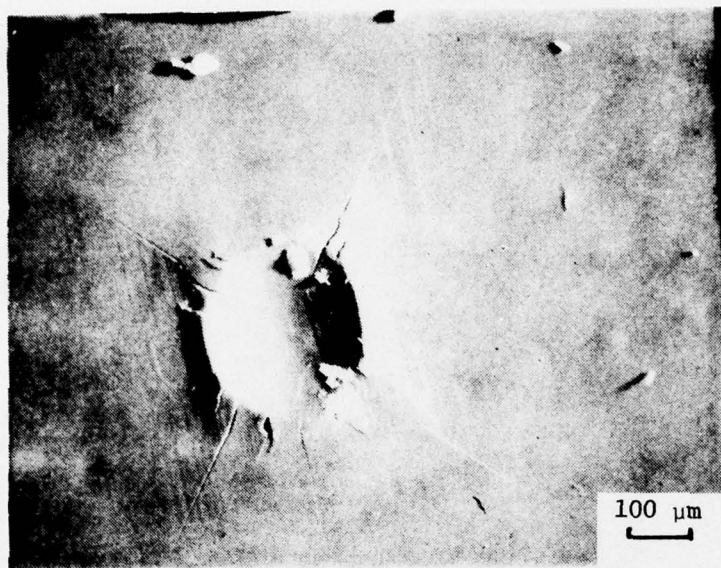
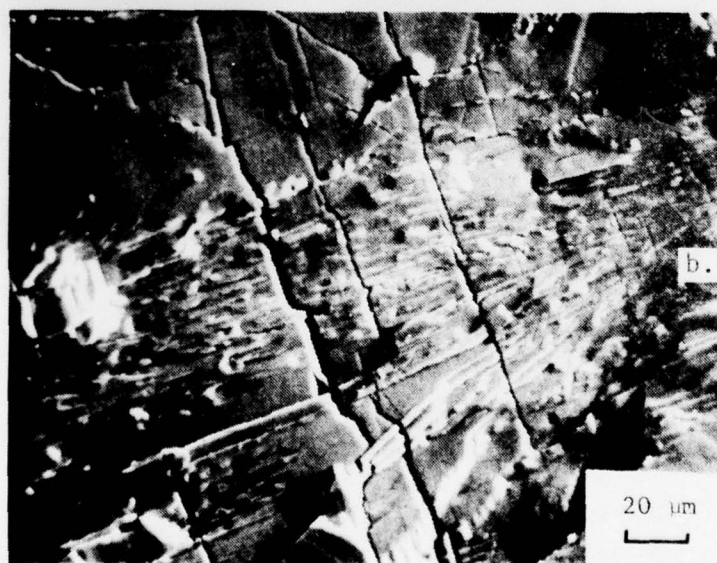


Figure 51. Scanning electron micrographs of (001) MgO impacted with a 1mm sapphire bead.

- (a) General overview of impact impression
- (b) Detail of fracture arresting slip bands



a. General overview
of impact im-
pression



b. Detail of
fracture
arresting
slip bands

Figure 52. Cross section of MgO specimen in Figure 51.

Additional increases in the impact velocity produce bulk cleavage in which cleavage fractures initiate from a point below the contact area and propagate radially outward along the $\{100\}$ axes and down into the sample. Figure 53 shows the cross section of an impact near the contact zone illustrating the extensive formation of lateral fracture and also the source of the catastrophic cleavages approximately $100\text{ }\mu\text{m}$ below the surface. No defects are visible (or anticipated) so it is assumed failure initiated by a plasticity assisted mechanism. Slit fractures aligned along the $\{110\}$ ₄₅ traces are readily apparent in Figure 53b located lower on the cleavage surface.

A fracture and slip structure is illustrated in Figures 54 and 55 for the higher velocity impacts. The plasticity zone clearly surrounds the fracture system. Microscopy views into the interior from both the top and cross-sectional planes indicate that the greatest strain is associated with the prominent $\{110\}$ slip bands and that these bands arrest fracture propagation. Fractures tend to initiate along crystallographic planes, particularly slit fractures associated with $\{110\}$ slip bands, and to a lesser extent at discontinuities such as hackle ledges. Since the fracture geometries are controlled by the slip bands, it is assumed that slip occurred during the compression phase and preceded fracture. The fracture structure does not establish when most of the fracture occurred. The fracture structure does indicate, however, that the large lateral (001) fractures which radiate outward are the last to form and occur during the relief phase.

3.3.4 Quasistatic Indentations

A limited series of quasistatic indentations with sapphire beads was undertaken for comparison with the bead impacts. Below the fracture threshold similar rosettes of slip bands were formed although contact areas were better defined. Again glide extended further for

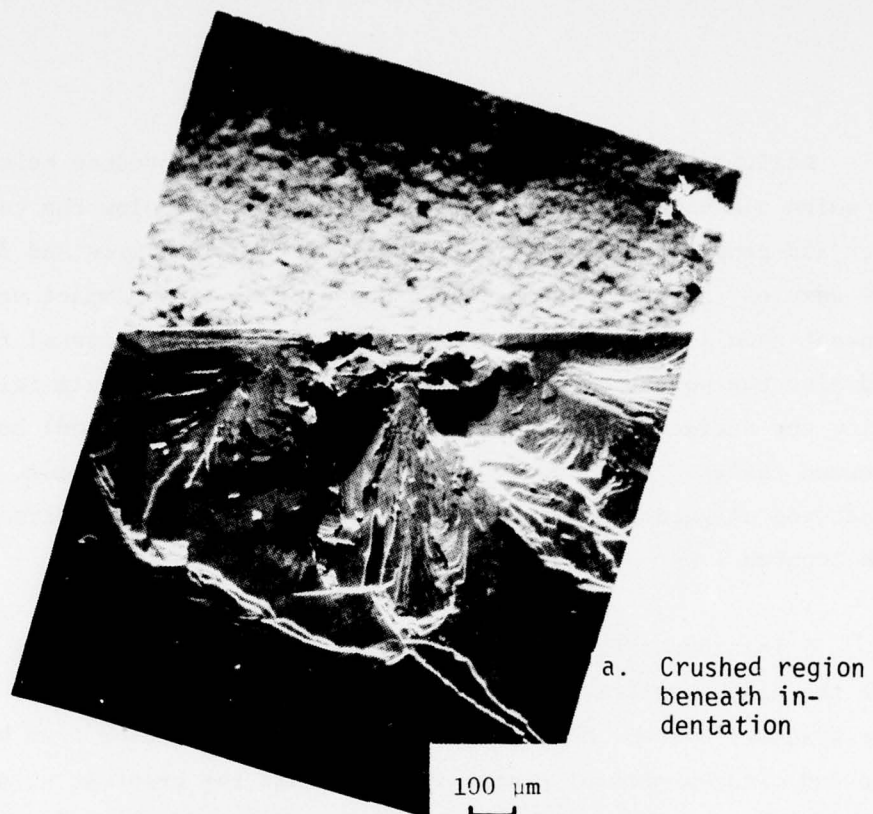
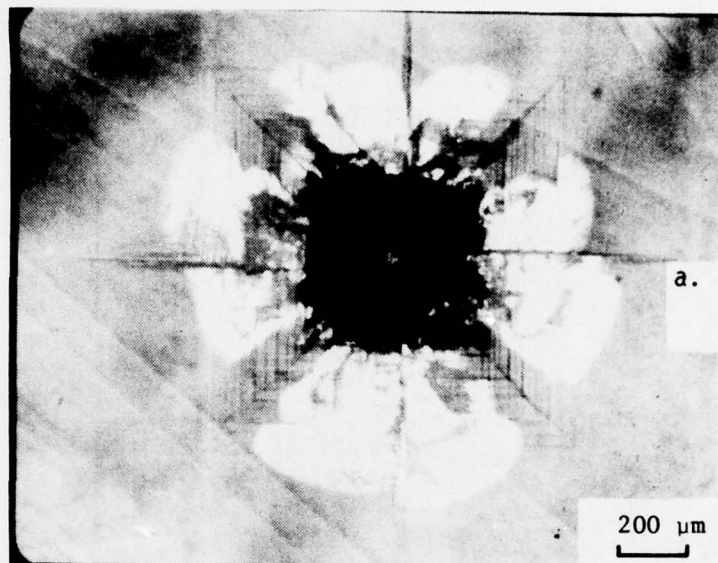
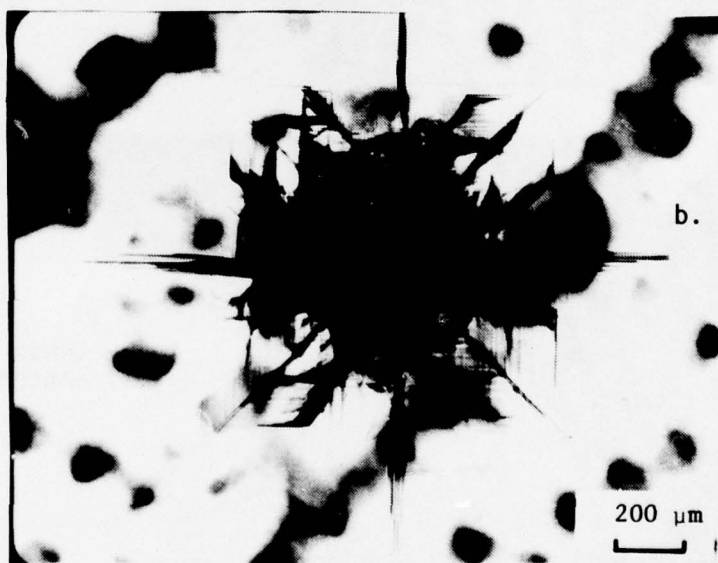


Figure 53. Scanning Electron Micrographs Cross Section of MgO Specimen Impacted with a 1 mm Sapphire Bead.

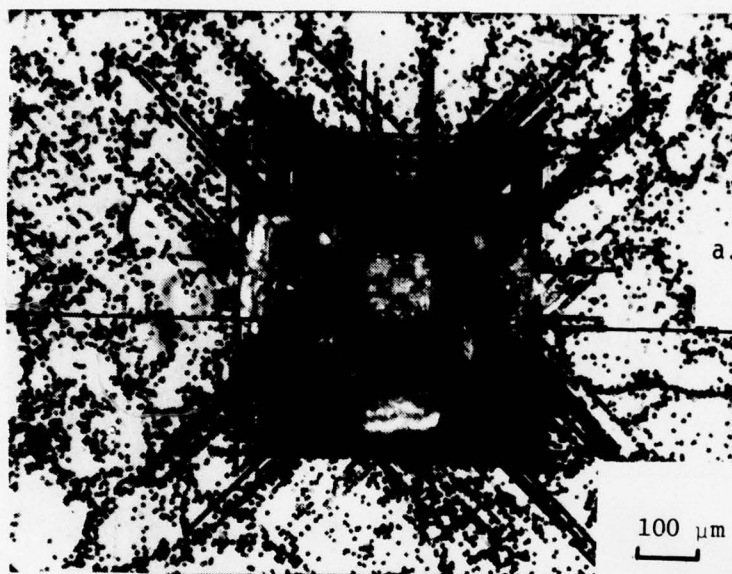


a. Catastrophic cleavage

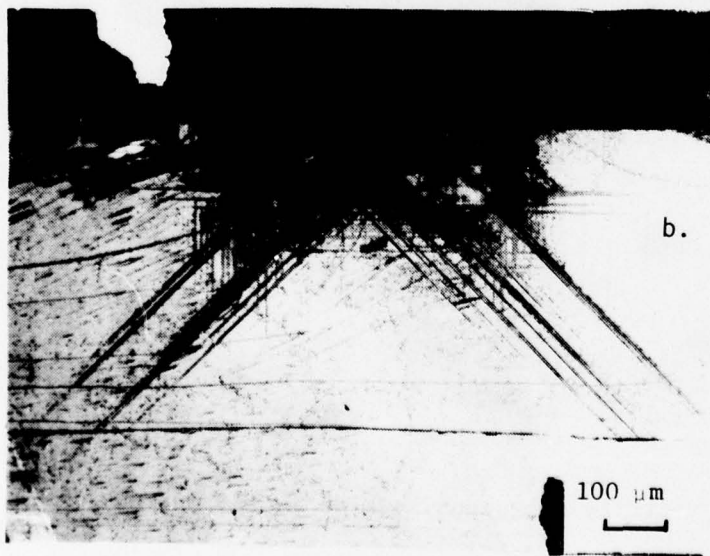


b. Origin of catastrophic cleavage

Figure 54. High velocity 1mm sapphire bead impact on (001) MgO



a. Top view showing cleavage plane for cross section



b. Cross section off center of impact

Figure 55. Dislocation etched specimen of (001) MgO After High Velocity Impact with a 1 mm Sapphire Bead.

the screw components on the $\{110\}_{45}$ planes than the edge components of the dislocations along the $\{110\}_{90}$ planes. Fracture initiation for this case was entirely different, beginning at the surface with circumferential $\langle 110 \rangle$ slit fractures. Sequential polish and etch procedures revealed these fractures were shallow, $<15 \mu\text{m}$ in depth, and originated at the intersection of prominent slip planes as shown by Argon and Orowan for uniform compressive loading.⁽³⁵⁾ Initiation of fracture as radial $\langle 110 \rangle$ crack propagation in the rosette arms was observed for Vicker's indentation geometry as previously reported but is not the initiation mechanism for spherical indentation.⁽³⁴⁾ Although the initial fracture geometry for spherical indentation is consistent with that anticipated for a Hertzian stress distribution, this distribution may not provide a valid approximation to indentation in the rock salt structure. Previous work has established that the dislocation configuration displaces material radially outward within the $\langle 110 \rangle$ rosette arms so that the plasticity response during compression would also establish the radial stress field to initiate fractures during the relief phase.⁽³⁴⁾

Increases in the indentation pressure produced more complicated surface and subsurface fracture patterns. Fracture conformed to crystallographic orientations and remained confined to the zone of plastic deformation. Comparing the quasistatic and impact fracture patterns, the encompassment by the slip band rosette, the confinement of fracture to the $\{110\}$ and $\{100\}$ planes, and the fracture pattern symmetry were similar. However, the fracture systems differ significantly. A well-defined crater is not formed by the indentation. The lateral fractures are much smaller and less important, the volume of fractured material also appears to be much smaller, and cleavage fractures into the bulk material were not observed for spherical indentations.

3.4 SAPPHIRE

Sapphire specimens were subjected to nylon and sapphire bead impacts. The nylon bead impacts produced rings of discontinuous fractures on both the 0° and 90° oriented surfaces. In contrast, the sapphire bead impacts yielded star-shaped fractures and cavities.

Nylon bead impact on (0001) sapphire yielded a hexagonal ring structures analogous to that reported for impact by cylindrical water jets.⁽³⁶⁾ Assignment of the fracture orientations as the $(10\bar{1}0)$ planes was confirmed by comparison with Laue diffraction images. The central zone enclosed within the ring was free of fracture.

Nylon bead impacts on $(12\bar{1}0)$ sapphire generally yielded elliptical rings of discontinuous fractures. This result was not anticipated since impact on $(10\bar{1}0)$ sapphire by cylindrical water jet had yielded two large parallel fractures which were attributed to fracture along the two internal $\{10\bar{1}0\}$ planes.⁽³⁶⁾ The long axes of the fracture structures were aligned parallel to the traces of the $\{10\bar{1}0\}$ planes perpendicular to the specimen's surface. Well-defined fractures were also observed nearly perpendicular to this axis which are not well-understood. There appears to be a small inclination to the traces of these fractures, forming approximately an 80° angle to the major axis. It is not clear whether they propagated along a path just off the basal plane (which resists preferential cleavage in the cantilever beam configuration) or propagated along a high index plane. Two other fracture trace orientations were observed at approximately 30° and 65° which can be reconciled with activation of the $\{10\bar{1}2\}$ rhombohedral planes. This orientation has been previously identified for a bent beam test configuration.⁽³⁷⁾

Figure 56 illustrates an elliptical fracture pattern and the crystallographic fracture structure. Although surface polarization effects

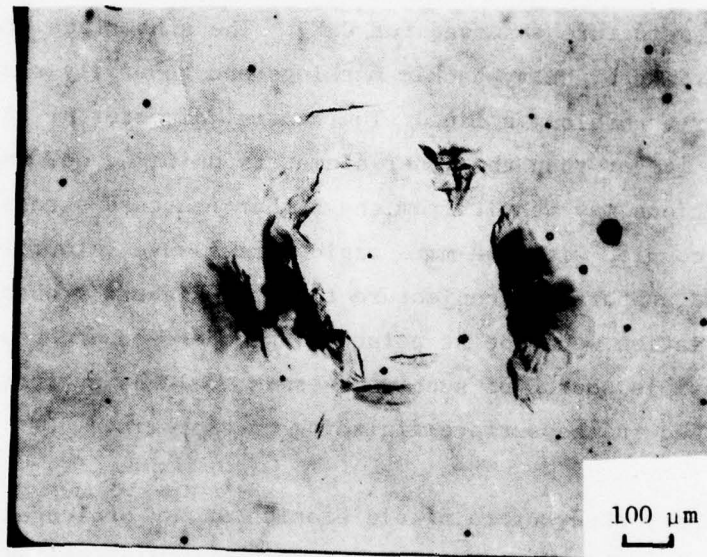


Figure 56. 1 mm nylon bead impacts on $(1\bar{2}10)$ oriented sapphire.

restricted the effectiveness of Nomarski interference contrast, none of the optical and electron microscopy techniques revealed evidence of scratch-assisted fracture. The ring fractures tended to be discrete so that the conical fractures penetrating the interior were created by the overlap pattern of many discrete planar fractures rather than having the coherent cone structure observed for CaF_2 . The subsurface fractures were characterized by heavy hackle markings and generally radiated from a point rather than along a line. The central diameter of .4 to .6 mm were somewhat larger than the inner diameters on CaF_2 , Ge, and Si. These observations may result from the higher fracture stress for sapphire. This coupled with the more rapid stress wave velocities for sapphire would support the conjecture that the highest probability for fracture initiation would be at points of weakness on and near the surface. A plausible source of such weaknesses would be surface grinding flaws identified in the surface finishing of sapphire. ⁽³⁸⁾

Preliminary study of rainfield erosion showed prolonged exposure at subsonic velocities produced a field of isolated minute pits rather than the surface fractures and lateral relief cavities observed on most brittle crystals and glasses. Water drop or nylon bead impacts on flame polished specimens (courtesy of P. Becher, NRL) are scheduled in order to explore the potential degree of fracture suppression.

1 mm sapphire bead impacts on (0001) sapphire surfaces produced complex star-shaped fractures. At the lower velocity, 165 ms^{-1} , the radial fractures preferentially propagated along the $\{10\bar{1}0\}$ orientations and secondarily along noncrystallographic orientations (and possibly $\{12\bar{1}0\}$ orientations). A higher velocity impact at 260 ms^{-1} produced a large crater. This process was similar to crater formation in CaF_2 but was unlike Si for which the craters were produced by the ejection of a crushed and broken central core. The cavity in sapphire formed by a lateral spall mechanism bounded by the radial fractures.

The general features of water drop and solid particle impacts have been considered in terms of relatively simple analytical models. The least restrictive but still meaningful equivalence criteria were established for comparing the two impact loading conditions: equal average pressures and equal contact radii. It was found that very low velocity solid bead impacts, less than 20 ms^{-1} , are equivalent (in the non-restrictive sense) to 1.8 mm water drop impacts in excess of 1000 ms^{-1} . However the time required for a water drop and equivalent solid particle impact condition to reach the same contact radius is more than an order of magnitude to in excess of two orders of magnitude larger for glass and sapphire bead impacts. In general it is not possible to satisfy all of the necessary equivalence criteria for solid bead and water drop impacts. The analytical idealizations used for water drops and hard solid beads should be representative of the physical impact conditions. The application of these idealizations to nylon beads is not straight-forward and requires further consideration.

In addition to the differences in the rate of loading reflected in the temporal and spatial development of the interfacial pressures for water drop and solid bead impacts on deformable targets, the water drop also has the capacity for lateral outflow jetting and hydraulic penetration into minute surface cracks (as described in the Introduction) which further differentiates the nature of the modes of damage associated with liquid drop impingement from rounded solid particle collisions. The ETI liquid drop impact facility (described in Section 2.1) is being used to understand the damage modes due to liquid drop impingement, while an air gun and an exploding wire particle accelerating facility are being used to obtain hard and soft solid bead impacts on crystalline materials for detailed microscopic examination of the damage modes for these localized impact conditions. Water drop impact damage on crystalline materials will be analyzed in a future report; only water drop impact conditions below the threshold for coherent fracture formations have been considered here.

Solid particle damage on CaF_2 depended on the loading rate and bead composition. Quasistatic indentation produced a hemispherical cavity surrounded by slip bands and a zone of plastic deformation. Fracture originated at the periphery of this cavity and propagated primarily along the $\{111\}$ planes and secondarily along the $\{100\}$ planes. Impact by sapphire beads resulted in a slight depression surrounded by a ring fracture and radial fractures. Extensive crushing occurred beneath the contact zone. Slip bands were not observed and the surrounding birefringence pattern was more diffuse than that surrounding the quasistatic indentations. Lateral, radial, and vent fractures all propagated along the $\{111\}$ plane for impact on the $\{111\}$ surface; fracture on the $\{001\}$ plane was not as crystallographic. Impact by nylon beads produced a damage free zone surrounded by a geometrical array of circumferential fractures aligned along the $\{111\}$ cleavage planes. A coherent pyramidal fracture surrounding the contact zone penetrated into the interior analogous to the conical fractures observed in glass for quasistatic indentations. An array of shallower cleavage fractures extended to radial distances beyond the dominant pyramid. Ultimately all the loading conditions for (001) CaF_2 produced predominant single or multiple penny-shaped fractures radiating outward from the contact zone in the $\langle 110 \rangle$ directions and tending to lie along $\{111\}$ planes. As described above however the events preceding the full development of this fracture system are quite distinct for each loading system.

Crystallographic fracture initiation was common to all test conditions for silicon. Isolated coherent fracture clusters are seen on the surface of (001) oriented Si in a multiple water drop environment. These fracture arrays are attributed to impact by a limited number of anomalously large drops in the general drop size distribution because of their low areal density in comparison with the impact density and the absence of extraneous fracture anticipated for a field of grinding damage.

The strong dependence of erosive damage on drop diameter suggests that standard rotating arm tests with well-defined drop sizes should be supplemented with evaluations of the limits of drop diameter and impact velocity over which the results of these tests are meaningful for the stated conditions. Well controlled and monitored single water drop impact experiments can certainly make a significant contribution to identifying the range of critical impact conditions for the onset of damage.

Comparison of the sapphire quasistatic bead indentation and bead impact fracture patterns in MgO indicates the encompassment by the slip band rosette, the confinement of fracture to the {110} and {100} planes, and the fracture pattern symmetry were similar. A well-defined crater is not formed by the indentation. The lateral fractures are much smaller and less important, the volume of fractured material also appears to be much smaller, and cleavage fractures into the bulk material were not observed for spherical bead indentations. Nylon bead impacts produce a different damage structure. Surface fracture is minimal, confined to minute cleavage fractures resulting from interfacial shear within the contact zone. At 1000 ms^{-1} the impact stress level was sufficient to initiate two orthogonal subsurface cleavage figures containing the [001] axis passing through the center of impact and lying essentially in the (100) and (010) planes. Additional slip was evident along the periphery of these half penny-shaped arcs.

THIS PAGE INTENTIONALLY BLANK

Acknowledgements

Several ETI staff members contributed to the development of the liquid drop impact facility which presented a challenge of unforeseen magnitude; the authors appreciate their various contributions in providing the present capability for investigating water drop impingement: especially the helpful suggestions of Mr. Robert E. Wengler. However the ingenuity and perseverance of Mr. Thomas L. Menna and Mr. Vernon F. Hall were the primary factors in the successful operation of the water drop impact facility. Their diligence in this regard is particularly appreciated. The efforts of Ms. Joy Burt in coordinating the preparation of the figures, typing and printing this report under somewhat trying conditions are gratefully acknowledged.

THIS PAGE INTENTIONALLY BLANK

REFERENCES

1. W. F. Adler, Wear, 37, 345 (1976)
2. W. F. Adler, J. Materials Science, 12, 1253 (1977)
3. F. P. Bowden and J. E. Field, Proc. Roy. Soc., A282, 331 (1964)
4. A. A. Fyall, "Single Impact Studies with Liquids and Solids", Proc. 2nd Meersburg Conference on Rain Erosion and Allied Phenomena, (A. A. Fyall and R. B. King, editors), published by the Royal Aircraft Establishment, England, 1967.
5. Y. M. Tsai, Int. J. Solids Structures, 7, 543 (1971)
6. R. M. Blowers, J. Int. Math. Applics., 5, 167 (1969)
7. M. C. Rochester and J. H. Brunton, "The Influence of Physical Properties of the Liquid on the Erosion of Solids", Erosion, Wear, and Interfaces with Corrosion, ASTM STP 567 (1974) 128
8. M. C. Rochester and J. H. Brunton, "Surface Pressure Distribution During Drop Impingement", Proc. 4th International Conference on Rain Erosion and Associated Phenomena, (A. A. Fyall and R. B. King, editors), published by the Royal Aircraft Establishment, England, 1974
9. W. Johnson and G. W. Vickers, J. Mech. Engrg. Science, 15, 302 (1973)

10. Y. C. Huang, Numerical Studies of Unsteady, Two-Dimensional Liquid Impact Phenomena, PhD Dissertation, Department of Mechanical Engineering, University of Michigan, (1971)
11. Jia-Bo G. Hwang, The Impact Between a Liquid Drop and an Elastic Half-Space, PhD Dissertation, Department of Mechanical Engineering, University of Michigan, (1975)
12. M. Rosenblatt, G. E. Eggum, L. A. DeAngelo, and K. N. Kreyenhagen, Numerical Investigation of Water Drop Erosion Mechanisms in Infra-red-Transparent Materials, AFML-TR-76-193 (December 1976)
13. R. Kinslow, Rain Impact Damage to Supersonic Radomes, Tennessee Technological University Report TTU-ES-74-3, (October 1974)
14. F. B. Peterson, J. Fluid Engng., Trans. ASME, 95 (Series A), 263 (1973)
15. F. J. Heymann, J. Basic Engng., Trans. ASME, 90, (Series B), 400 (1968)
16. F. J. Heymann, J. Appl. Phys., 40, 5113 (1969)
17. A. E. H. Love, Phil. Trans. Roy. Soc., A288, 377 (1929)
18. P. C. Waterman, Phys. Rev., 113, 1240 (1959)
19. W. F. Adler and S. V. Hooker, "Rain Erosion Mechanisms in Brittle Materials," to be published in Wear.
20. Work carried out at Effects Technology, Inc., for hypervelocity particle impacts under SAMSO Contract F04701-76-C-0069.

21. S. V. Hooker, Wear, 38, 253 (1977)
22. S. Freiman, P. Becker, R. Rice, and K. Subramanian, "Fracture Behavior in Alkaline Earth Fluorides," Proc. Fifth Annual Conference on Infrared Laser Window Materials, (Compiled by C. R. Andrews and C. L. Strecker), published by the Defense Advanced Research Projects Agency, (February 1976)
23. A. G. Evans, and T. R. Wilshaw, J. Materials Science, 12, 97 (1977)
24. M. V. Swain and B. R. Lawn, Phys. Stat. Sol., 35, 909 (1969)
25. Y. M. Tsai and H. Kolsky, J. Mech. Phys. Solids, 15, 263 (1967)
26. T. S. Liu and C. H. Li, J. Appl. Phys., 35, 3325 (1964)
27. A. G. Evans, et.al., Proc. Brit. Ceramic Soc., 6, 173 (1966)
28. W. F. Adler and S. V. Hooker, "Water Drop Impact Damage in Zinc Sulfide", to be published in Wear.
29. K. H. Jolliffe, Phil. Trans. Roy. Soc., A260, 101 (1966)
30. J. Narayan, Wear, 25, 99 (1973)
31. B. G. Koepke and R. J. Stokes, J. Materials Science, 5, 240 (1970)
32. W. F. Adler and S. V. Hooker, Characterization of Transparent Materials for Erosion Resistance, AFML-TR-76-16 (March 1976)
33. K. Meyer and E. Gregert, Phys. Stat. Sol., 3, 2005 (1963)

34. A. S. Keh, J. Appl. Phys., 31, 1538 (1960)
35. A. S. Argon and E. Orowan, Phil. Mag., 9, 1003 (1964)
36. J. E. Field, Phil. Trans. Roy. Soc., A260, 86 (1966)
37. S. M. Wiederhorn, J. Amer. Ceramic Soc., 52, 485 (1969)
38. P. F. Becher, J. Amer. Ceramic Soc., 59, 143 (1976)